A Chromatin-Sensing Pathway Regulates Cytokinesis

Daniel Beaudet

A Thesis

In the Department

of

Biology

Presented in Partial Fulfillment of the Requirements

For the Degree of

Doctor of Philosophy (Biology) at Concordia University

Montreal, Quebec, Canada

July 2019

CONCORDIA UNIVERSITY

School of Graduate Studies

This is to certify that the thesis prepared

By: Daniel Beaudet
Entitled: A Chromatin-Sensing Pathway Regulates Cytokinesis

and submitted in partial fulfillment of the requirements for the degree of

Doctor of Philosophy (Biology)

Complies with the regulations of the University and meets the accepted standards with respect to originality and quality.

Signed by the final Examining Committee:

_____Chair
Dr. Cameron Skinner

_____External Examiner
Dr. Gilles Hickson

_____External Examiner
Dr. Peter Darlington

_____Examiner
Dr. William Zerges

_____Examiner
Dr. Michael Sacher

_____Supervisor
Dr. Alisa Piekny

Approved by

_____
Dr. Robert Weladji, Graduate Program Director

Tuesday, August 20th, 2019

_____
Dr. André Roy, Dean Faculty of Arts and Science

Abstract

A Chromatin-Sensing Pathway Regulates Cytokinesis

Daniel Beaudet, Ph.D.

Concordia University, 2019

Cytokinesis is the physical separation of a cell into two daughter cells. The core machinery is well-conserved across metazoans, yet the mechanisms that regulate cytokinesis can vary depending on the organism and cell type. Elucidating these mechanisms is important, because cytokinesis failure could lead to cell fate changes and aneuploidy, which are hallmarks of cancer. Cytokinesis occurs by the ingression of an actomyosin contractile ring that assembles between the segregating chromatids, and pinches in the plasma membrane. The mitotic spindle provides spatiotemporal signals that regulate the cytokinetic machinery. However, a number of studies have shown that spindle-independent pathways also regulate cytokinesis. The focus of my thesis is on the characterization of a Ran-GTP pathway that spatially regulates the contractile ring in response to chromatin position. During mitosis, there is a gradient of Ran-GTP with high levels around chromatin and lower levels toward the cortex. Ran-GTP competes importin(s) from the nuclear localization signal (NLS) of proteins, and we hypothesize that importin-binding to cortical proteins could regulate their function. In support of this hypothesis, we found that anillin, a key component of the contractile ring, contains an NLS within its C-terminus that is required for importin-binding and for its function during cytokinesis. Importin-binding facilitates anillin's cortical recruitment, possibly by stabilizing an open conformation. Interestingly, the NLS is autoinhibited by the adjacent RhoA binding domain (RBD), and binding to active RhoA relieves this inhibition. I also found that feedback between the RBD and C2 domain, which contains the NLS, is required for

optimal RhoA-binding and cortical recruitment. Thus, integrating a signal from chromatin could ensure that the contractile ring remains positioned between segregating chromatids. This mechanism could be crucial for the asymmetric division of polarized cells, or cells with aneuploidy.

Acknowledgements

I would like to first and foremost thank my supervisor, Dr. Alisa Piekny, for giving me the opportunity to conduct research and complete my PhD, and for being an amazing mentor throughout the process. I would also like to thank my committee members, Dr. Michael Sacher and Dr. William Zerges for their guidance and invaluable feedback.

In addition, I would like to thank the Centre for Microscopy and Cellular Imaging at Concordia University. In particular, Dr. Chris Law and Dr. Chloë van Oostende for all their help and training. Thank you for your patience and the countless times that I have needed your troubleshooting guidance.

Of course, I would like to thank my fellow lab mates, who have made the lab an extremely productive, yet entertaining environment. Karina and Dilan, a special thanks goes to you guys for the moral support, pep talks, and guidance throughout our years together in grad school. Melina, Tara, and Madhav, I am very fortunate to have started in the lab with you guys and I am thankful for everything that you have taught me in the time that we worked together. I would also like to acknowledge the many remaining members of the Piekny lab who have advised, listened, helped, and provided critical feedback, in which I am extremely thankful for.

Lastly, I would like to thank my wife Sarah and sister Stephanie for their support and guidance, and my Dad who has always encouraged me to -stay in sciences, as it will keep all of my doors open.

Dedications

I decided to dedicate this thesis to my wife Sarah and to my daughter Hannah. Their continuous motivation and support helped me tremendously throughout my research and I am extremely grateful for the many sacrifices they have made for me to fulfil these achievements. Sarah, you encouraged me to go back to school and you stood by my side during every challenging moment of grad school and of life. Hannah, you have made me stronger, more patient and more fulfilled than I could ever have imagined. I love you both.

Contribution of Authors

Figure 3: Tara Akhshi performed fixed cell imaging and cortical measurements as shown in B.

Figure 4: Tara Akhshi and I both contributed to live cell imaging and cortical accumulation measurements as shown in A and B.

Figure 6: Julia Phillipp quantified percentages of binucleate cells as shown in the bar graph in B.

Figure 7: Dr. Chris Law designed and wrote an ImageJ macro to measure the average anillin intensity at the cortex and its distance to chromatin for timelapse images.

Figure 10: Nhat Pham performed the pull-down assay as shown in A.

Figure 11: Nhat Pham performed the pull-down assay as shown in A.

Figure 12: Noha Skaik and I both made mutant anillin C-terminus constructs by PCR-based site directed mutagenesis used throughout the figure.

Figure 13: Noha Skaik and I both made mutant anillin full-length constructs by PCR-based site directed mutagenesis used throughout the figure.

Figure 14: Noha Skaik made the mutant constructs by PCR-based site directed mutagenesis (B-D), performed fixed cell imaging, and quantified nuclear localized of anillin as shown in B.

Figure S1. Tara Akhshi performed live cell imaging, cortical accumulation measurements, and colocalization measurements as shown in A and D.

Figure S2. Tara Akhshi performed fixed and live cell imaging as shown in A and C.

Figure S6. Nhat Pham and I both contributed to co-sedimentation assays and quantification as shown in A and B. Noha Skaik performed lipid overlay assays as shown in C.

Figure S7. Nhat Pham and I both had equal contribution to the pull-down experiment.

Table of Contents

List of Figures

List of Supplemental Figures

List of Abbreviations

14-3-3	14-3-3 protein named after elution fraction and migration position following chromatography
a.a.	Amino acid
a.u.	Arbitrary units
ADA	ADA complex – Transcriptional adaptor histone acetylation complex
AHD	Anillin Homology domain
BHK	Baby hamster kidney cells
BKGD	Background
Boi1/2	Bem1 (Bud-emergence 1) interacting protein 1/2
BSA	Bovine serum albumin
C-term	C-terminus or carboxyl-terminus
C1	Protein kinase C conserved lipid binding region 1
C2	Protein kinase C conserved lipid binding region 2
Cdc42	Cell division control protein 42
Cdk1	Cyclin-dependent kinase 1
cDNA	Complementary DNA
CIN	Chromosomal instability
CPC	Chromosomal passenger complex
Cyk4	Cytokinesis defect 4 [or MgcRacGAP [Male germ cell RacGAP (Rac GTPase activating protein) Rho-family GAP in humans]
DAPI	4',6-diamidino-2'-phenylindole dihydrochloride

DH	Dbl (diffuse B-cell lymphoma) Homology domain
DMEM	Dulbecco's Modified Eagle Medium
DMSO	Dimethyl sulfoxide
DNA	Deoxyribonucleic acids
DSHB	Developmental Studies Hybridoma Bank
DTT	Dithiothreitol
Ect2	Epithelial cell transforming 2
EGTA	Ethyleneglycol- bis(β-aminoethyl)-N,N,N′,N′-tetraacetic Acid
ERM	Ezrin/Radixin/Moesin
F-actin	Filamentous-actin
FBS	Fetal bovine serum
FL	Full-length
FRAP	Fluorescence recovery after photobleaching
GAP	GTPase activating protein
GDP	Guanosine diphosphate
GEF	Guanosine nucleotide exchange factor
GFP	Green fluorescent protein
GST	Glutathione S-transferase
GTP	Guanosine triphosphate
GTPase	Guanosine triphosphatase
H2B	Histone H2B
I/F	Interface

Imp- α/β	Importin-α/β- nuclear transport receptors
Inh	Inhibition
Ipl1	Increase in ploidy protein 1- Spindle assembly checkpoint kinase
KIF2C	Kinesin family member 2C (or MCAK)
LGN	Mammalian homolog of Pins
LUTs	Look up tables
M.W.	Molecular weight
MBP	Maltose binding protein
MCAK	Mitotic centromere-associated kinesin (or KIF2C)
mCherry	Monomeric cherry fluorescent protein
MDCK	Madin-Darby Canine Kidney epithelial cells
mDia	Mammalian diaphanous
Mem-Ran	mCherry:neuromodulin(1-60) Ran
Mid1	or dmf1(division mal foutue 1) protein
MKLP1	Mitotic kinesin like protein 1
MLC	Myosin light chain
MP-GAP	M phase GTPase activating protein
mRuby	Monomeric red fluorescent protein
MT	Microtubules
Myc	Polypeptide affinity protein tag derived from cMyc
N-term	N-terminus or NH_2-terminus
n.s.	Not significant

NIH	National Institute of Health
O/E	Overexpression
P	Pellet
PAR	Partitioning protein
PCR	Polymerase chain reaction
Pebble	*Drosophila* homolog of Ect2
PH	Pleckstrin Homology
PI3P	Phosphatidylinositol 3-phosphate
$PI4,5P_2$	Phosphatidylinositol 4,5-bisphosphate
Pins	Partner of Inscuteable
PIPES	1,4-Piperazinediethanesulfonic acid
Plk1	Polo-like kinase 1
PMSF	phenylmethanesulfonyl fluoride
PP1-Sds22	Protein phosphatase 1 and its regulatory subunit Sds22
PS	Penicillin and streptomycin
Rac	Ras-related C3 botulinum toxin substrate protein
Ran	Ras-related nuclear protein GTPase
RanGAP	Ran GTPase activating protein
RanQ69L	Constitutively active Ran
RBD	Rho-binding domain
RCC1	Regulator of chromosome condensation 1
RhoA	Ras homolog family member A

RNAi	Ribonucleic Acid interference
ROCK	Rho-associated protein kinase
ROI	Region of interest
S	Supernatant
S2 cells	Schneider 2 cells
SAF	Spindle assembly factor
SD	Standard deviation
SDS	Sodium dodecyl sulfate
SDS-PAGE	SDS- Polyacrylamide gel electrophoresis
SEM	Standard error of the mean
SIN kinase	Septation initiation network kinase
Sir-tubulin	Silicon rhodamine-like tubulin fluorescent probe
siRNA	Small interfering ribonucleic acid
STC	S-trityl-L-cysteine
TCA	Trichloroacetic acid
TPXL-1	Targeting protein for *xenopus* Klp2 (kinesin-like protein 2)-like protein 1
ts	Temperature sensitive
tsBN2	Baby hamster kidney cells with a ts allele in RCC1

Chapter 1: Introduction

Cytokinesis is the physical separation of a cell into two daughters and occurs at the end of mitosis. During anaphase, an actomyosin contractile ring is assembled at the midzone of the cell and pinches in the plasma membrane to divide the cytoplasm and segregated chromatids into the nascent daughters (**Figure 1**). After ingression, the contractile ring transitions to a midbody, which acts as a platform for the abscission machinery to separate the cells (**Figure 1**). Mis-regulation of cytokinesis or its failure has many pathological implications including cancer, by causing cell fate changes and aneuploidy (Lacroix and Maddox, 2012). Therefore, it is crucial to improve our knowledge of how cytokinesis is regulated to elucidate the diseases that are associated with its aberrant effects. The mitotic spindle provides cues that regulate the cortex and is thought to be the prevailing mechanism that assembles and ingresses the contractile ring (Green et al., 2012). However, a number of studies showed that microtubule-independent mechanisms also influence the division plane (Deng et al., 2007; von Dassow et al., 2009; Cabernard et al., 2010; Sedzinski et al., 2011; Kiyomitsu and Cheeseman, 2013; Zanin et al., 2013; Rodrigues et al., 2015). Many of the microtubule-dependent and -independent mechanisms regulating cytokinesis are conserved among metazoans, however their importance or role may vary depending on the cell type and organism. This thesis describes a novel chromatin-based mechanism that positions the contractile ring and works together with mitotic spindle pathways to ensure robust cytokinesis.

1.1 The Contractile Ring

Assembly and ingression of the actomyosin ring is controlled by RhoA GTPase. RhoA is bound to GTP in its active form, causing a switch in its conformation that favors binding to effectors that regulate F-actin and myosin. For example, RhoA-GTP binds to and activates formins

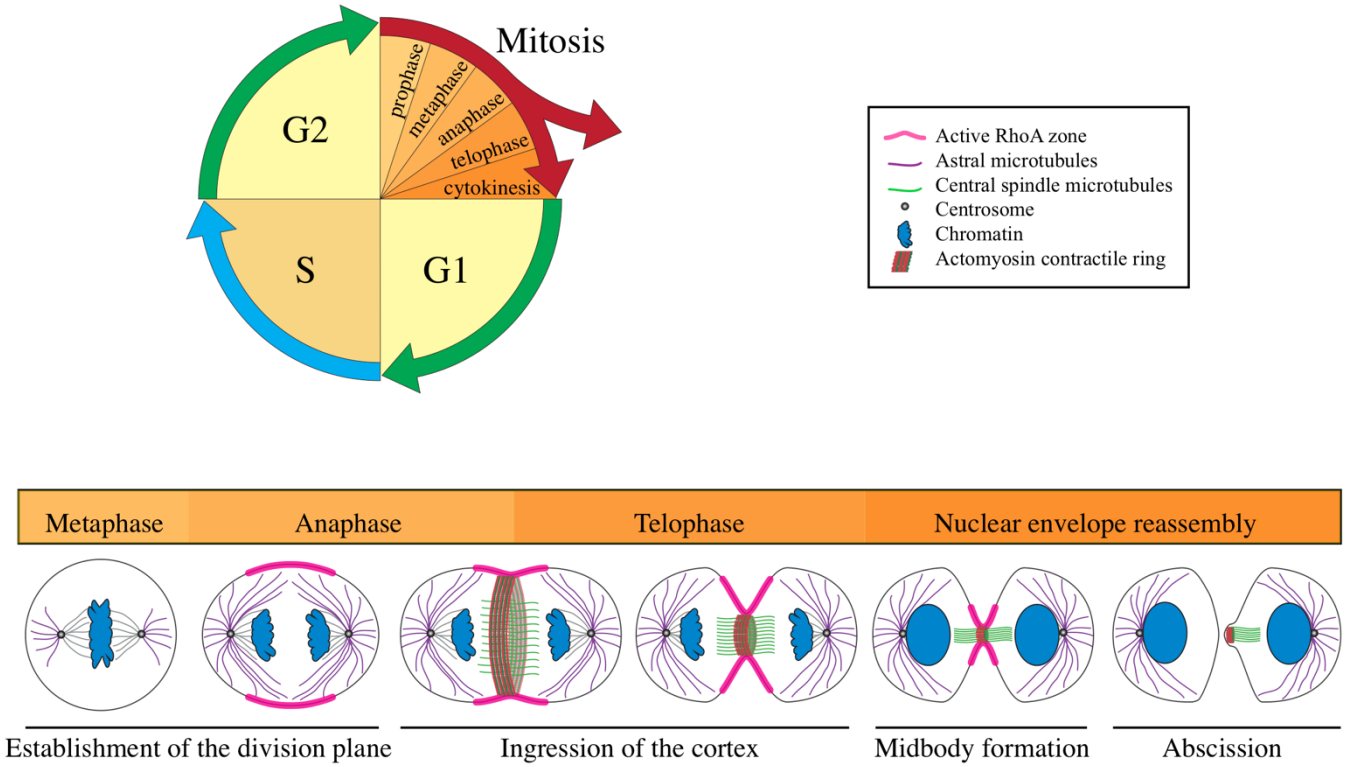

Figure 1. Cytokinesis

The schematic shows that cytokinesis occurs at the end of mitosis to complete the cell cycle. Below, are cartoons of cells depicting the major events at different stages of cell division. During the metaphase to anaphase transition, sister chromatids begin to segregate to their respective poles and the division plane is established. During anaphase and telophase, the contractile ring forms in the division plane and ingresses the cortex. The nuclear envelope is reassembled during telophase and after ingression, the contractile ring transitions to form the midbody, the site at which the abscission machinery will be recruited to resolve the nascent daughter cells.

to generate actin filaments, and Rho-dependent kinase (ROCK) to activate non-muscle myosin II (**Figure 2**; Piekny et al., 2005). Active RhoA also directly binds to and recruits anillin, a highly conserved scaffold protein that localizes to the equatorial cortex and binds to F-actin and myosin (**Figure 2**; Field and Alberts, 1995; Oegema et al., 2000; Straight et al., 2005; Piekny and Glotzer, 2008; Piekny and Maddox, 2010).

In many cell types, anillin is required for cytokinesis. For example, in anillin-depleted HeLa cells, contractile proteins oscillate around the cortex and cytokinesis eventually fails (Piekny and Glotzer, 2008; Piekny and Maddox, 2010). Similar phenotypes have been observed in S2 cells and *Xenopus* cells (Straight et al., 2005; Hickson and O'Farrell, 2008, Reyes et al., 2014). Anillin is a large protein with many binding domains that are important for its function. Through its many interactions anillin helps to stabilize the division plane by crosslinking the contractile ring and its regulators to the spindle and plasma membrane (**Figure 2**). The N-terminus of anillin organizes cortical contractility as it contains domains that bind and bundle F-actin (Field and Alberts, 1995; Oegema et al., 2000; Jananji et al., 2017), as well as bind active non-muscle myosin II (Straight et al., 2005). Anillin also indirectly binds to actin through an interaction with the Diaphanous-related formin (mDia), suggesting that anillin also influences actin nucleation or polymerization (Watanabe et al., 2008; Watanabe et al., 2010). Anillin also binds to citron kinase through a domain in the N-terminus, which is required for the ring-midbody transition during the later stages of cytokinesis (Echard et al., 2004; Gai et al., 2011; Bassi et al., 2013; El-Amine et al., 2013; Watanabe et al., 2013; McKenzie et al., 2016; El-Amine et al., 2019). The C-terminus of anillin contains a RhoA-GTP binding domain (RBD), a neighboring C2 domain, and a Pleckstrin Homology (PH) domain (**Figure 2**). Together, the C-terminal domains coordinate anillin's equatorial recruitment through the binding of active RhoA to the RBD, as well as binding to

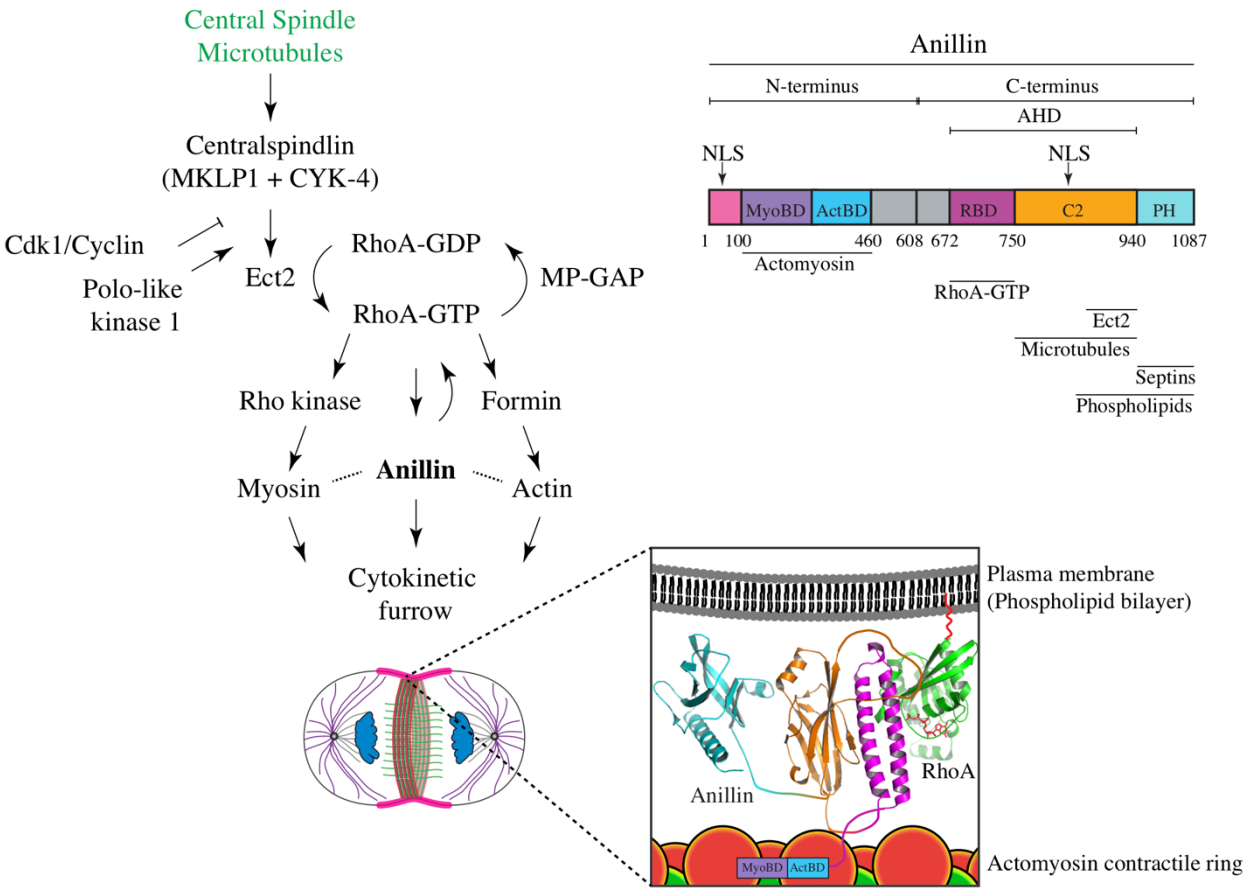

Figure 2. Active RhoA regulates contractile ring assembly

The pathway shows how the central spindle signals to the overlaying cortex to activate RhoA-GTP, which subsequently leads to the assembly of contractile proteins to form the cytokinetic furrow. The inset shows a zoomed-in region of the plasma membrane (grey) and actomyosin (red and green circles) with anillin and RhoA-GTP (green) between them. The ribbon structure of the C-terminus of anillin shows the RhoA-GTP binding domain (RBD; pink), a C2 domain (orange) and Pleckstrin Homology domain (PH; blue). The N-terminus of anillin binds to myosin and actin (purple and blue, respectively). A linear structure of anillin indicating its various domains in different colors [myosin binding domain (MyoBD; purple), actin binding domain (ActBD; blue), RhoA-binding domain (RBD; pink), C2 domain (orange), which binds to Ect2, microtubules, and phospholipids, and the Pleckstrin Homology domain (PH; cyan), which binds to septins and phospholipids), as well as the locations of nuclear localization signals (NLS).

phospholipids, such as phosphoinositol-4, 5-bisphosphate ($PI4,5P_2$), which is enriched within the equatorial cortex, and to septins through the C2 and PH domains (**Figure 2**; Oegema et al., 2000; Field et al., 2005; Liu et al., 2012; Sun et al., 2015; Budnar et al., 2019). Septins are a family of conserved GTPases that oligomerize to form filaments and higher ordered structures that associate with the plasma membrane (Piekny and Maddox, 2010). Septins may be important for the removal of anillin to mediate the contractile ring to midbody transition, which requires the coordinated shedding of the membrane, and opposes the action of citron kinase to stabilize anillin at the midbody (Kechad et al., 2012; El-Amine et al., 2013). Other studies have shown that anillin's equatorial recruitment is also affected by microtubule-binding through the C2 domain (van Oostende Triplet et al., 2014), as well as importin-binding through a site within a disordered loop emanating from the C2 domain (*discussed below*; Beaudet et al., 2017). Based on its interaction with the core regulators of cytokinesis, studying anillin's function can provide a better understanding of the mechanisms that regulate cytokinesis.

1.2 Microtubule-Dependent Mechanisms

The mitotic spindle spatially controls the division plane. Signals associated with the spindle help form a zone of active RhoA GTPase at the equatorial cortex. RhoA is a key regulator for cytokinesis that promotes assembly and contraction of the actomyosin ring. Early experiments performed by Rappaport (1996), and subsequently by Bement et al., (2005), demonstrated that after shifting the mitotic spindle to a new position in anaphase, active RhoA and the cytokinesis furrow will re-locate over the mid-plane of the newly positioned spindle.

The central spindle, which arises between sister chromatids during anaphase and is composed of antiparallel bundled microtubules, relays positional cues to the overlying cortex to

control the zone of RhoA activation for contractile ring assembly and ingression. Centrally-located signals are not explicitly derived from antiparallel bundled microtubules, but could also come from centrally positioned astral microtubules whose plus-ends point towards the equatorial cortex and have central spindle-like complexes bound to them (*i.e.* centralspindlin and CPC; as *discussed below*) (Canman et al., 2003; Inoue et al., 2004; Nishimura and Yonemura, 2006; Foe and von Dassow, 2008; Vale et al., 2009). Centralspindlin, a heterotetramer complex composed of MKLP1 (Kinesin-6 microtubule motor protein) and Cyk4 (MgcRacGAP, Rho-family GAP) dimers, is essential for the organization of the spindle midzone (Mishima et al., 2002; Mishima et al., 2004; Glotzer, 2009). This complex is also required for the activation of Ect2, a RhoA guanine nucleotide exchange factor (GEF) (**Figure 2**; Tatsumoto et al., 1999; Kimura et al., 2000; Yüce et al., 2005; Basant and Glotzer., 2018). Cyk4 is phosphorylated by Polo-like kinase 1 (Plk1), which then permits a direct interaction between the C-terminus of Cyk4 and the N-terminus of Ect2 (Yüce et al., 2005; Petronczki et al., 2007; Burkard et al., 2009; Wolfe et al., 2009). In addition, the GEF activity and membrane localization of Ect2 are autoinhibited by cell cycle-dependent regulation. The N-terminus of Ect2 inhibits the DH PH domains in the C-terminus, which are relieved when Cdk1 levels drop at the onset of anaphase (Kim et al., 2005; Yüce et al., 2005; Niiya et al., 2006). However, it remains unclear as to how centralspindlin regulates Ect2 at the equatorial cortex, especially in cells that have a significantly large distance between the central spindle and equatorial cortex. In particular, in *C. elegans*, ECT-2 localizes to the cortex, while centralspindlin localizes to the central spindle. However, recent studies found a small, but detectable pool of centralspindlin at the cortex, where it could regulate Ect2 (Lakomtsev et al., 2012; Basant et al., 2015). In human cells, Ect2 localizes to the central spindle, which is Cyk4-dependent, and to the equatorial cortex, which is dependent on phospholipid binding through the PH and polybasic tail domains (Su et al.,

2011). Several studies showed that Ect2 does not need to be recruited to the spindle midzone for its activity, but does require lipid binding (Frenette et al., 2012; Lakomtsev et al., 2012; Kotýnková et al., 2016). Centralspindlin oligomers have also been shown to accumulate weakly at the cortex (Lakomtsev et al., 2012; Basant et al., 2015). The association of centralspindlin with the cortex occurs via the C1 domain of Cyk4, which binds to phospholipids. This domain is essential for RhoA activation in *C. elegans* (Basant et al., 2015), although in human cells it is not required for activation of RhoA, but plays a critical role during late cytokinesis by linking the plasma membrane to the dense microtubules at the midbody (Lakomtsev et al., 2012). Aurora B kinase, which is a part of the chromosomal passenger complex (CPC), relocates from chromosomes to the spindle midzone and the equatorial cortex upon anaphase onset and has been shown to regulate centralspindlin. Membrane-localized centralspindlin is inhibited by PAR-5/14-3-3 in the polar regions of the cell, while at the midzone Aurora B kinase activity via the CPC overrides this inhibition by phosphorylation of MKLP1, which drives oligomerization of centralspindlin (Guse et al., 2005; Douglas et al., 2010; Basant et al., 2015). A more recent study proposed that Plk1 phosphorylation may release centralspindlin complexes from the central spindle, where they can be recruited to the equatorial cortex via their lipid-binding domain(s) (Adriaans et al., 2019). Phosphorylation of MKLP1 by Aurora B kinase could prevent sequestration by 14-3-3, so that the centralspindlin complexes can form oligomers and activate Ect2 in the equatorial cortex. However, it is still not clear if Cyk4-binding is required for Ect2 activity, and if so, how this binding regulates Ect2 function.

Astral microtubules also regulate the zone of active RhoA for contractile ring positioning during cytokinesis. Unlike the central spindle, astral microtubules that emanate toward the polar regions of the cell inhibit the localization of contractile proteins at the cell poles (Tse et al., 2011;

van Oostende Triplet et al., 2014). However, the mechanism by which they do this is not well understood. Cells treated with nocodazole to depolymerize microtubules caused a global increase in active RhoA (Chang et al., 2008). Treating cells with nocodazole during cytokinesis similarly caused the zone of accumulated contractile proteins to spread along the cortex (Murthy and Wadsworth, 2008; Zanin et al., 2013; van Oostende Triplet et al., 2014). Further, increasing the length of astral microtubules through the depletion of MCAK/kinesin-13 (mitotic centromere-associated kinesin), which is a microtubule depolymerase that regulates microtubule length and tracks to the plus-end of growing microtubules, decreased the zone of accumulated contractile proteins (Rankin and Wordeman, 2010; Zanin et al., 2013; van Oostende Triplet et al., 2014). The astral pathway may function through anillin, since contractile proteins no longer respond to lengthened astral microtubules when cells are co-depleted of anillin (van Oostende Triplet et al., 2014). Anillin contains a microtubule-binding domain in its C-terminus, and its localization to microtubules negatively correlates with its localization to the equatorial cortex (Tse et al., 2011; van Oostende Triplet et al., 2014). For example, decreasing the levels of active RhoA by Ect2 depletion caused an increase in the localization of endogenous anillin to microtubules (van Oostende Triplet et al., 2014). In addition, stabilizing spindle microtubules via Taxol-treatment caused an enrichment of anillin localization to microtubules at the expense of its localization to the cortex (Tse et al., 2011; van Oostende Triplet et al., 2014). Thus, microtubules could function as a sink for anillin to control cortical levels, and to prevent ectopic cortical contractility. Another study showed that in the early *C. elegans* embryo, the clearing of F-actin and anillin at the polar cortex is dependent on the astral microtubule-based TPXL-1 mediated activation of Aurora A kinase (Mangal et al., 2018). Their model is that a phosphorylation gradient of Aurora A kinase causes the clearing of RhoA activity and contractile proteins from the polar cortex. However, it is

unclear if Aurora A activity directly impacts RhoA and/or anillin localization or if there are other proteins involved since few other molecular regulators of the astral pathway are known (Bringmann et al., 2007; Basant and Glotzer, 2018).

1.3 Microtubule-Independent Mechanisms

A number of microtubule-independent pathways have also been shown to spatially control cytokinesis in different model systems. In *Drosophila* neuroblasts, a cortical pathway that regulates apicobasal polarity acts together with the spindle to asymmetrically position the cleavage furrow (Cabernard et al., 2010). Cells lacking polymerized microtubules or with mispositioned spindles showed that microtubules are dispensable for the asymmetric accumulation of anillin and myosin (Cabernard et al., 2010). Pins (*Drosophila* homolog of LGN) is a cortical protein that typically helps to position the mitotic spindle in asymmetrically dividing cells, but in neuroblasts is also required for the asymmetric accumulation of anillin and myosin in the absence of an intact spindle (Cabernard et al., 2010). A similar pathway may function in the early *C. elegans* embryo to ensure that the furrow is tightly aligned with cortical polarity (Schenk et al., 2010). In the early *C. elegans* embryo, cortical PAR proteins establish polarity and position the cleavage furrow. Different PAR proteins accumulate either in the posterior or anterior cortex of the one-cell embryo and this accumulation is mutually exclusive (Cowan and Hyman, 2007). This ensures the segregation of the appropriate PAR protein complexes for the cortical and cytosolic polarization of the embryo to ensure that each daughter adopts the correct fate. Gα-complexes, which are conserved with the subunits of the LGN and Pins complexes, generate pulling forces on the spindle to shift it towards the posterior cortex (Schenk et al., 2010). In return, the spindle aligns the cleavage furrow with the boundary between the anterior and posterior PAR complexes. The forces

create cortical flows that also re-position the PAR complexes and myosin to further align the spindle with the cleavage furrow (Schenk et al., 2010). Interestingly, in human cells, LGN localization is dependent on anillin, suggesting a role-reversal in their requirements for cortical polarization (van Oostende et al., 2014).

Another cortical mechanism works through MP-GAP, a GTPase activating protein that inactivates RhoA and restricts the equatorial zone of active RhoA for cytokinesis (Zanin et al., 2013). Depletion of MP-GAP caused cells to have ectopic cortical activity, although cells often still successfully complete cytokinesis. Co-disruption of astral microtubules with MP-GAP enhanced cytokinesis phenotypes, while their stabilization through MCAK depletion suppressed cortical activity, suggesting that MP-GAP functions in a microtubule-independent manner. MP-GAP is localized globally around the cortex, and the model is that it keeps RhoA inactive, but Ect2 (GEF) activation at the equatorial cortex overrides MP-GAP to specifically generate active RhoA in the equatorial plane.

Another microtubule-independent pathway that coordinates cytokinesis in *Drosophila* and human cells stems from the kinetochores (Rodrigues et al., 2015). This pathway triggers the relaxation of the polar cortex in anaphase cells and depends on PP1 phosphatase and its regulatory subunit Sds22 (Rodrigues et al., 2015). As chromosomes move toward the polar cortices in mid-anaphase, kinetochore-localized PP1-Sds22 dephosphorylates moesin, an ERM (Ezrin/Radixin/Moesin) protein, causing dissociation of F-actin at the cell poles (Carreno et al., 2008; Roubinet et al., 2011; Rodrigues et al., 2015). This promotes the local softening of the polar cortex to allow for elongation of the anaphase cell to prepare for cytokinesis. However, it is not clear how kinetochore signaling is coordinated with other pathways that regulate the localization of contractile proteins during cytokinesis.

In yeast, a NoCut pathway acts as a surveillance mechanism to ensure that chromatin is cleared from the midzone prior to abscission to prevent any DNA damage and ensure the viability of the cell. The NoCut pathway is triggered by central spindle defects, as well as lagging and/or unsegregated chromatids (Norden et al., 2006; Mendoza et al., 2009). This pathway relies on the activity of Ipl1 (Aurora B kinase) and the anillin-related proteins Boi1 and Boi2, which localize to the cleavage furrow (Norden et al., 2006). The presence of chromatin in the spindle midzone triggers the NoCut signal, where the histone acetylation complex ADA regulates Aurora B activity to delay abscission (Mendoza et al., 2009). In human cells, Aurora B is a key regulator of abscission timing and its inactivation is required for the completion of cytokinesis (Eggert et al., 2006; Ruchaud et al., 2007). An Aurora B-mediated abscission checkpoint prevents the furrow from regressing prior to abscission in cells with perturbed chromosome segregation. If chromosomes fail to segregate, Aurora B activity is sustained at the intercellular bridge between nascent daughters (Steigemann et al., 2009). MKLP1, which is required for stabilizing the midbody and anchoring the ingressed furrow, is a likely target of this checkpoint (Guse et al., 2005; Neef et al., 2006). Prolonged Aurora B activity sustains MKLP1 at the midbody, delaying abscission to give the cell adequate time to resolve the chromosome bridge, which would otherwise result in tetraploidization (Steigemann et al., 2009). Similarly, in *Drosophila* neuroblasts, trailing chromatid arms correlate with elongation of the cell and prolonged cytokinesis (Kotadia et al., 2012). Elongated cells have increased spindle length and myosin efflux, which flows outwards from the contractile ring in response to sustained *Pebble* (Ect2) activity (Montembault et al., 2017). *Pebble* localizes to the nucleus after ingression, and their model is that the trailing chromatid arms delay nuclear envelope assembly, keeping *Pebble* in the cytosol. Excess RhoA activation would

cause prolonged cortical myosin activity, which would spread away from the equator resulting in the elongation of the cell.

Active Ran associated with chromatin also has been shown to influence the localization of contractile proteins. Active Ran (Ran-GTP) is essential for many cellular functions including nucleocytoplasmic transport, spindle assembly and nuclear envelope formation. Ran is best known for its role in interphase cells where it regulates the nuclear import of proteins that contain nuclear localization signals (NLS) (Cavazza and Vernos, 2015). Importins, which are nuclear transport receptors, bind to NLS-containing proteins in the cytosol and shuttle them across the nuclear envelope. Inside the nucleus, Ran-GTP binds to importins to release the cargo protein (Cavazza and Vernos, 2015; Soniat and Chook, 2015). RanGAP stimulates GTP hydrolysis to generate inactive Ran and is high in the cytosol, while RCC1 (RanGEF) stimulates the exchange of GDP for GTP to activate Ran and is tethered to histones on chromatin. This compartmentalization of Ran regulators generates a steep chemical gradient across the nuclear envelope, where high levels of Ran-GTP are sequestered to the nucleus and inactive Ran (Ran-GDP) is in the cytosol (Kaláb et al., 2006). After nuclear envelope breakdown during mitosis, high levels of Ran-GTP are maintained around chromatin forming a gradient where the concentration of Ran-GTP decreases toward the cortex (Kaláb et al., 2006). The mitotic Ran gradient is also well known for its role in the regulation of proteins required for bipolar spindle assembly. Ran-GTP induces the release of NLS-containing spindle assembly factors (SAFs) from importins close to chromatin, which permits them to become active to regulate spindle assembly, for example by binding to partners or altering their conformation (Kaláb and Heald, 2008).

The Ran pathway also functions to regulate the cortex during meiosis. In mouse oocytes with highly asymmetrically positioned meiotic spindles, chromosome-derived Ran-GTP regulates

cortical polarity (Deng et al., 2007). Chromatin positioned at a precise distance from the cortex induces the formation of an actin cap, which is a zone of enriched actin organized along the cortex (Deng et al., 2007). The authors suggested that the Ran-GTP signal from chromatin is consistent with the range of the gradient in mitotic somatic cells, and functions as a molecular ruler to spatially position the actin cap. They proposed that rather than being strictly stimulatory or inhibitory, the effects of the gradient on cortical proteins or their regulators are sensed in a distance-dependent manner. Thus, at a precise distance from the cortex, Ran-GTP is at a threshold concentration to mediate the enrichment of cortical proteins. A more recent study showed that the formation of the actin cap is dependent on Cdc42, and its activation correlates with the position of meiotic chromosomes (Dehapiot et al., 2013). However, it is not clear how the Ran-GTP gradient regulates Cdc42 activity. In a follow-up study they also found that ERM proteins were inactive at the cortex furthest away from the meiotic spindle leading to the collapse of microvilli, which is an essential part of oocyte division (Dehapiot and Halet, 2013). However, it is not clear whether this mechanism applies to cytokinesis, where Cdc42 and Rac regulation of actin are not essential.

Ran-GTP also influences the cortex during cytokinesis. The Ran-GTP gradient persists until late anaphase/early telophase, when RCC1 is sequestered by the reforming nuclear envelope (Li and Zheng, 2004; Clarke and Zhang, 2008). In cells lacking polymerized microtubules and stimulated to exit mitosis, anillin is cleared from the region of the cortex near chromatin (Kiyomitsu and Cheeseman, 2013). However, reducing Ran-GTP in these cells, which express a temperature-sensitive RCC1 allele, anillin no longer responds to chromatin position (Kiyomitsu and Cheeseman, 2013). This data suggests that Ran-GTP may inhibit the accumulation of anillin, and/or other cortical components. The authors proposed a model where Ran-GTP regulates the cortex in response to chromatin to recover the division plane when the spindle shifts too close to

one pole (Kiyomitsu and Cheeseman, 2013). However, the data in this study was correlative, and they did not investigate the molecular mechanism by which Ran-GTP regulates the cortex, or the function of Ran-GTP during cytokinesis. Another study showed that Ran-GTP influences the localization of anillin during pseudocleavage in *Drosophila* syncytial embryos (Silverman-Gavrila et al., 2008). Pseudocleavage describes the process where membrane invaginates between nuclei, which is largely driven by the trafficking of lipids to the growing membrane (Finger and White, 2002). Some of the proteins that regulate cytokinesis also localize to the pseudocleavage membranes, which may have a role in this process (Miller and Kiehart, 1995). This study showed that anillin's interaction with another contractile ring component, septin, is competed by the overexpression of importin-α *in vitro* and in embryos (Silverman-Gavrila et al., 2008). They proposed a model where anillin is released from importins to permit septin-binding in the presence of high Ran-GTP (Silverman-Gavrila et al., 2008). However, anillin and septin colocalize to membranes between nuclei, not over them, and the levels of Ran-GTP would be predicted to be lower not higher in these locations. Further, it is not clear how such a model would apply to cytokinesis, since chromosomes are positioned near the poles, while septins are in the equatorial plane. A more likely model is that Ran-GTP functions as a molecular ruler vs. being strictly stimulatory or inhibitory. Different proteins could be differently regulated by Ran-GTP, and at unique distances based on their binding affinities with importins and/or other partners.

1.4 Summary

Both microtubule-dependent and -independent mechanisms spatially control the localization of contractile proteins to couple cytokinesis with the segregation of chromosomes and fate determinants. Different cell types may more strongly rely on one pathway vs. another. For

example, cells with large astral microtubules may rely more heavily on them vs. cells with large central spindles (Glotzer, 2009). Microtubule-independent mechanisms such as the Pins-LGN pathway or MP-GAP regulation may be more essential in polarized cells during development, where it is crucial to maintain different cortical domains (Cabernard et al., 2010). Other microtubule-independent pathways such as the NoCut pathway or myosin efflux may function as safety mechanisms to prevent premature cleavage in cells that have errors in chromatin segregation or to adjust the division plane to ensure that trailing chromosomes have time to segregate correctly (Norden et al., 2006; Mendoza et al., 2009; Steigemann et al., 2009; Kotadia et al., 2012; Montembault et al., 2017). In addition, signals from chromatin have been shown to position the division plane in a number of model systems and is thought to act as a molecular ruler to ensure that cell division occurs at a precise position from chromatin (Deng et al., 2007; Dehapiot et al., 2013; Dehapiot and Halet, 2013) or to correct for spindle position when the mitotic spindle shifts too close to the cortex (Kiyomitsu and Cheeseman, 2013).

This thesis sheds light on the molecular pathway by which chromatin spatially regulates the contractile ring during cytokinesis. Our hypothesis is that the Ran pathway acts as a global mechanism to regulate cortical proteins during cytokinesis and we propose that anillin is a target of this pathway. Specifically, importins bind to a C-terminal NLS to potentiate anillin's recruitment to the equatorial cortex by stabilizing a conformation that favors its cortical interactions (*e.g.* by enhancing RhoA-binding or phospholipid binding).

The first part of this thesis (*Chapter 2*), demonstrates that a chromatin-based Ran-GTP pathway regulates the division plane during cytokinesis. We show that active Ran is essential for the localization of contractile proteins and for cytokinesis. Our data suggests that this pathway regulates the function of anillin, a key cytokinesis regulator, for contractile ring positioning. Ran-

GTP competes importin complexes from the nuclear localization signal (NLS) of cargo proteins and we show that anillin contains an NLS within the C-terminus and that importin binds to this site. Further, we show that importin-binding potentiates anillin's cortical recruitment to the cortex and that mutating the NLS perturbs anillin localization and function. This data supports a model where importins form an inverse gradient to Ran-GTP and act as a ruler to properly position anillin at the equatorial cortex for its function during cytokinesis.

The second part of this thesis (*Chapter 3*) provides evidence that importin binding enhances anillin's cortical affinity and promotes its association with RhoA-GTP. We show that anillin is autoregulated and that binding to RhoA induces conformational changes within its C-terminal domains that enable its interaction with importins, which further stabilize its interaction with active RhoA at the cortex. Our evidence suggests that importin enhances RhoA binding and that this feedback is coordinated through a C-terminal intramolecular interface between the RhoA binding domain and the C2 domain. We propose that importins and RhoA work together to mediate anillin's cortical recruitment and function for cytokinesis. In summary, the work shown in this thesis uncovers the molecular underpinnings of the Ran pathway and shows that it is a novel mechanism that regulates anillin's cortical function during cytokinesis.

Chapter 2: Active Ran regulates anillin function during cytokinesis

Adapted from: Beaudet D., Akhshi T.K., Phillipp J., Law C., and Piekny A. (2017). Active Ran regulates anillin function during cytokinesis. *Molecular Biology of the Cell,* 28, 3517-531.

2.1 Abstract

Cytokinesis cleaves a cell into two daughters at the end of mitosis and must be spatially coordinated with chromosome segregation to prevent aneuploidy. The dogma is that the mitotic spindle governs the assembly and constriction of an actomyosin ring. Here, we reveal a function for active Ran in spatially restricting the ring. Our model is that during anaphase, 'free' importins, whose gradient inversely correlates with active Ran and chromatin position, function as a molecular ruler for the recruitment and localization of anillin, a contractile protein and a crucial regulator of cytokinesis. We found that decreasing Ran-GTP levels or tethering active Ran to the equatorial membrane affects anillin's localization and causes cytokinesis phenotypes. Anillin contains a conserved nuclear localization signal (NLS) at its C-terminus that binds to importin-β and is required for cortical polarity and cytokinesis. Mutating the NLS decreases anillin's cortical affinity, causing it to be more dominantly regulated by microtubules. Anillin contains a RhoA-GTP binding domain, which autoinhibits the NLS and neighbouring microtubule-binding domain, and RhoA-GTP binding may relieve this inhibition during mitosis. Retention of the C-terminal NLS in anillin homologues suggests that this is a conserved mechanism to control anillin function.

2.2 Introduction

Cytokinesis is driven by the ingression of an actomyosin ring, which cleaves a cell into two daughters. The contractile ring is spatially controlled by the mitotic spindle to coordinate with the

segregation of chromosomes and cell fate determinants (Green et al., 2012; Akhshi et al., 2014; D'Avino et al., 2015; Cheffings et al., 2016). Failed or dysfunctional cytokinesis causes changes in cell fate and ploidy, which can be detrimental and/or cause cancer (Lacroix and Maddox, 2012; D'Avino et al., 2015). During early anaphase, actomyosin filaments accumulate at a broad region of the cortex which transitions into a tight ring-like organization as the cell progresses through mitosis (Green et al., 2012; Akhshi et al., 2014; D'Avino et al., 2015; Cheffings et al., 2016). The highly conserved protein anillin is a crucial regulator of cytokinesis in metazoans and has binding sites for key regulators and core effectors of cytokinesis, including F-actin, myosin, RhoA, septins, phospholipids, and microtubules (Piekny and Maddox, 2010; Tse et al., 2011; van Oostende Triplet et al., 2014). Owing to its ability to bind to these components, previous studies have focused on how inputs from different pathways are integrated by anillin to spatially control the contractile ring (*e.g.* Zanin et al., 2013; van Oostende Triplet et al., 2014).

Multiple pathways regulate cytokinesis, yet the requirement for them varies between organisms and cell types. The majority of studies have focused on microtubule-dependent mechanisms, for which the prevailing dogma in the field is that the anaphase spindle determines the division plane for cytokinesis. The central spindle stimulates contractile ring assembly around the equatorial cortex (Somers and Saint, 2003; Bement et al., 2005; Yüce et al., 2005; Zhao and Fang, 2005), while astral microtubules exclude contractile proteins from the poles (Dechant and Glotzer, 2003; Bringmann and Hyman, 2005; Werner et al., 2007; Lewellyn et al., 2010; van Oostende Triplet et al., 2014). However, signals from other cellular locations, such as kinetochores, chromatin or centrosomes, also influence the localization of contractile proteins (*e.g.* Canman et al., 2000; Canman et al., 2003; Potapova et al., 2006; Deng et al., 2007; Petronczki et al., 2007; Silverman-Gavrila et al., 2008; Cabernard et al., 2010; Kotadia et al., 2012; Dehapiot et

al., 2013; Kiyomitsu and Cheeseman, 2013; Zanin et al., 2013; Rodrigues et al., 2015). A kinetochore pathway functions in *Drosophila* and human cells to mediate relaxation of the polar cortex during anaphase, independent of microtubules and centrosomes (Rodrigues et al., 2015). A kinetochore-tethered complex containing PP1 phosphatase and its regulatory subunit Sds22 dephosphorylates the actin regulator moesin at the cell poles to promote cortical relaxation (Carreno et al., 2008; Roubinet et al., 2011; Rodrigues et al., 2015). Although the balance of active moesin is important, it is not essential for cytokinesis *per se*, and this pathway functions for just a short time during early anaphase. Microtubule-independent pathways may be crucial for cytokinesis in cells where the spindle is positioned far from parts of the cortex, such as in highly polarized cells. In support of this, the cortex still polarizes and ingresses in the absence of polymerized microtubules or an intact mitotic spindle in dividing *Drosophila* neuroblasts with apical/basal polarity (*e.g.* Cabernard et al., 2010).

Chromatin-associated signals also regulate the cortex during cytokinesis. In yeast and metazoans, a NoCut pathway regulates the abscission machinery to prevent the cortex from cutting through unsegregated chromosomes (Norden et al., 2006; Mendoza et al., 2009; Steigemann et al., 2009). Acetyltransferase is associated with chromatin and regulates the activity of Ipl1/Aurora B kinase to modulate proteins that control abscission, such as Boi1 and Boi2 (anillin-like proteins) and septins in yeast, or MKLP1 in human cells (Norden et al., 2006; Potapova et al., 2006; Mendoza et al., 2009; Steigemann et al., 2009). However, the mechanisms by which chromatin-associated signals regulate the cortex during earlier stages of mitotic exit are not well-understood. In *Drosophila* neuroblasts, increasing the length of chromatid arms causes an increase in the breadth of active myosin localization during late anaphase and early telophase, leading to dramatic changes in cell shape (Kotadia et al., 2012). During meiosis of mouse oocytes, chromatin

positioned near the cortex induces the formation of an actin cap via Ran-GTP, and the placement of DNA-coated beads near the cortex induces cortical polarity independent of microtubules (Deng et al., 2007). These studies suggest that a chromatin-associated Ran-GTP gradient functions as a molecular ruler to organize the cortex. Furthermore, this gradient may regulate active Cdc42 and Rac for actin cap formation, while excluding ERM (Ezrin/Radixin/Moesin; Dehapiot et al., 2013; Dehapiot and Halet, 2013). However, it is not clear whether this mechanism applies to cytokinesis, where Cdc42 and Rac are not essential. In another study, Ran-GTP was shown to positively regulate the actomyosin cortex for pseudocleavage furrowing in the early *Drosophila* embryo (Silverman-Gavrila et al., 2008). Ran-GTP releases importin(s) from a nuclear localization signal (NLS) that overlaps with the septin-binding site in the C-terminus of anillin to permit septin binding (Silverman-Gavrila et al., 2008). It is not clear how this model applies to cytokinesis, because the contractile ring assembles and ingresses away from chromosomes. Another study showed that Ran-GTP inhibits rather than promotes anillin's cortical localization in mitotic mammalian cells (Kiyomitsu and Cheeseman, 2013). While anillin clears from the cortex near chromatin in cells with depolymerized microtubules and induced to exit mitosis, it fails to clear in cells with decreased active Ran (Kiyomitsu and Cheeseman, 2013). The authors suggest a model where Ran-GTP regulates cell elongation in response to chromatin in order to maintain the division plane during cytokinesis (Kiyomitsu and Cheeseman, 2013). However, they did not study the function of Ran-GTP during cytokinesis or the molecular mechanism by which Ran-GTP regulates the cortex.

Here, we show that human anillin is regulated by active Ran during anaphase. We found that decreasing Ran-GTP leads to the ectopic localization of anillin and myosin to the cell poles and blocks furrowing in BHK (Baby Hamster Kidney) epithelial cells. In HeLa cells, targeting

active Ran to the furrow membrane causes a reduction in anillin localization and oscillation phenotypes similar to those observed after anillin depletion. Anillin contains a highly conserved NLS at its C-terminus that binds to importin-β, and is needed to mediate cortical polarization and cytokinesis. Furthermore, mutating the NLS reduces anillin's affinity for the equatorial cortex, causing it to be more dominantly regulated by astral microtubules during cytokinesis. However, high overexpression of importin-β negatively regulates anillin's cortical localization. Thus, 'free' importins may function as a molecular ruler, for which optimal levels mediate the cortical recruitment of anillin by stabilizing a conformation that improves accessibility to cortical proteins and lipids. However, high levels of importins could reduce off-rates and sterically hinder binding to other sites at the C-terminus. Interestingly, anillin's RhoA-GTP binding domain blocks accessibility to the NLS and neighbouring microtubule-binding domain, and we propose that RhoA-GTP binding during early mitotic exit relieves this autoinhibition. Thus, our model is that RhoA-GTP binding to anillin opens the conformation of the C-terminus to make it more accessible for binding to importin and microtubules. A gradient of free importins forms in response to chromatin, where Ran-GTP levels are high. Optimal levels of importins likely form near the equatorial plane and facilitate anillin's cortical recruitment during anaphase. These results shed light on a novel mechanism through which Ran-GTP polarizes the cortex during cytokinesis.

2.3 Materials and Methods

2.3.1 Cell culture, transfection and drug treatments

HeLa, BHK (Baby Hamster Kidney), and tsBN2 (with a ts mutation in RCC1 in BHK) cells were plated and grown in Dulbecco's Modified Eagle Medium (DMEM; Wisent), supplemented with 10% fetal bovine serum (FBS; Thermo Scientific), 2 mM L-glutamine

(Wisent), 100 U penicillin and 0.1 mg/mL streptomycin (Wisent) with 5% CO_2. HeLa cells were maintained at 37°C, and BHK and tsBN2 cells were maintained at 33°C. For transfection, cells were plated in DMEM media without antibiotics (PS), and transfected using Lipofectamine 2000 (DNA or DNA and siRNA co-transfection in HeLa, BHK or tsBN2 cells; Invitrogen) or Oligofectamine (siRNA transfection in HeLa cells; Invitrogen) according to manufacturer's protocol, except that 4 μL of Lipofectamine was used per 2 mL of media with 0.5–1.5 μg DNA and 3 μL of 2 nM siRNAs, as described previously (Yüce et al., 2005; Piekny and Glotzer, 2008). Cells were imaged 24–26 hours after DNA transfection, and 27–30 hours after co-transfection of DNA and siRNAs.

Anillin and Ect2 siRNAs were used as described previously (Yüce et al., 2005; Piekny and Glotzer, 2008). The following drugs were used and dissolved in DMSO as 1000X stocks: Importazole (Sigma-Aldrich), S-trityl-L-cysteine (STC; Sigma-Aldrich), Blebbistatin (Sigma-Aldrich) and Purvalanol A (Sigma-Aldrich). To make cells monopolar, 2 μM of STC was used to arrest cells in prometaphase, followed by the addition of 22.5 μM Purvalanol A to promote mitotic exit (Hu et al., 2008). For Nocodazole (Sigma-Aldrich) treatments, 33 nM was added to cells 3 minutes after anaphase onset to selectively disrupt astral microtubules, while 100 nM was added to cells for 3–4 hours to depolymerize the majority of microtubules and cause mitotic arrest. 22.5 μM Purvalanol A was then added to promote mitotic exit during imaging. 100 μM Blebbistatin was added to cells to inhibit myosin II activity during imaging. 100 nM Importazole was added to HeLa cells for either 4 hours in combination with Nocodazole to test for changes in polarization, or for 8 hours to test for changes in the nuclear localization of anillin. Control cells were treated with DMSO for all of the experiments involving drug treatments.

tsBN2 cells with a ts mutation in RCC1 was generously provided by I. Cheeseman

(Whitehead MIT; Nishimoto et al., 1978; Kiyomitsu and Cheeseman, 2013). HeLa cells stably expressing GFP:non-muscle regulatory myosin light chain (T18E S19E) and anillin:GFP were previously described (Zanin et al., 2013; van Oostende Triplet et al., 2014). Myc-tagged human karyopherin (importin-β1; KPNB1; accession number NM_002265) cDNA was obtained from Origene.

H2B:mRuby was generated from H2B:GFP, generously provided by G. Hickson (University of Montreal). GFP was replaced with mRuby using *BamHI* (New England Biolabs) and *XbaI* restriction enzymes (New England Biolabs) and the pcDNA3-mRuby2 plasmid kindly provided by C. Brett (Concordia University). mCherry:Neuromodulin (1-60) Ran (WT) was generated via PCR using Ran cDNA (True Clone), and the pTK24 plasmid (Addgene), using *XhoI* and *EcoRI* restriction enzymes (New England Biolabs). Ran Q69L was generated in the same vector by quickchange PCR. GFP:Ran and GFP:Ran (Q69L) was cloned into pEGFP-C1 (Life Technologies) using *XhoI* and *EcoRI* restriction enzymes. The anillin constructs were previously described (Piekny and Glotzer, 2008), except for GFP:anillin (748-1087), which was cloned into pEGFP-C1 (Life Technologies) using *HindIII* and *SacII* restriction enzymes. mRuby:anillin was generated from GFP:anillin by replacing GFP with mRuby using *AgeI* and *SacI* restriction enzymes. The 850 KK 851-DE mutations were generated in the anillin constructs by quickchange PCR. All constructs were verified by sequencing.

2.3.2 Fixation, immunofluorescence and live imaging

Cells were fixed for immunofluorescence using 10% trichloroacetic acid (TCA) or 100% cold methanol as previously described (Yüce et al., 2005). Fixed cells were immunostained for microtubules using 1:200 mouse anti-tubulin antibodies (DM1A, Sigma-Aldrich), anillin using

1:200 rabbit polyclonal anti-anillin antibodies (Piekny and Glotzer, 2008), GFP using 1:100 mouse Clones 7.1 and 13.1 (Roche) or 1:200 rabbit anti-GFP polyclonal antibodies generously provided by M. Glotzer (University of Chicago). Anti-rabbit or mouse Alexa 488 and anti-mouse or rabbit Alexa 568 (Invitrogen) secondary antibodies were used at a 1:250 dilution. DAPI (Sigma-Aldrich) was added at a 1:1000 dilution (1 mg/mL stock) for 5 minutes before mounting the coverslips onto slides. Fixed cells were imaged using a Fluoview FV10i confocal laser scanning microscope (Olympus), with the 60x/1.35 oil immersion objective, and 3x magnification (total magnification of 180x). Images were acquired as 0.5 μm Z-stacks with the pinhole set at 1 airy unit. Fixed cells also were imaged using a Leica DMI6000B wide-field microscope with the 63x/1.4 PL APO oil immersion objective (pixel size 0.102 μm), and Z-stacks of 0.5 μm were acquired with a Hamamatsu OrcaR2 camera and Volocity software (PerkinElmer) using a piezo Z stage (MadCityLabs). Fixed cells also were imaged with high resolution using the Zeiss LSM800 airyscan mode with the C-APO 63x/1.2 oil immersion objective, and Z-stacks of 0.17 μm, using a 32 channel GaAsP Airyscan spatial detector that provides spatial resolution 1.7x typically achieved via confocal imaging at 1 airy unit. Image files were exported as TIFFs, which were opened with ImageJ (NIH) and converted into maximum intensity Z-stack projections. Projections and merged colour images were then converted into 8-bit images and imported into Illustrator (Adobe) to make figures.

To perform live imaging, media was replaced with phenol red-free DMEM media. Cells were plated and transfected on 25 mm round coverslips (No. 1.5) placed in a 35 mm Chamlide magnetic chamber (Quorum), or on a 35 mm μ-Dish with 2 mL volume (ibidi), or on μ-Slide Angiogenesis tissue culture-treated 15-well dishes (ibidi). Cells were kept at 37˚C (except for BHK and tsBN2 cells, which were kept at either 33˚C or 39.7˚C) with 5% CO_2 using the INU-TiZ-F1

chamber (MadCityLabs). For BHK and tsBN2 cells, Sir-tubulin (Cytoskeleton) was added to a final concentration of 200 nM 3–4 hours before filming, and Hoechst 33342 (Invitrogen) was added to a final concentration of 160 nM 30–40 minutes before filming. tsBN2 cells were upshifted for 30–40 minutes before imaging. Live imaging was performed on an inverted Nikon Eclipse Ti microscope with a Livescan Swept Field confocal unit (Nikon), using the 60x/1.4 CFI PLAN APO VC oil immersion objective (pixel size 0.27 μm), a piezo Z stage (MadCityLabs), and with the iXON897 EMCCD camera (Andor). Images were acquired with 200 ms exposures using the 488 and 561 nm lasers (100 mW, Agilent) set between 20–40% power, depending on the intensity of fluorescent signals (settings were kept constant for related experiments), and multiple Z-stacks of 0.5 μm were taken every 40–60 seconds per cell using NIS-Elements acquisition software (Nikon), and a narrow GFP or dual filter (500-544 and 600-665 nm; Chroma). The tsBN2 cells were kept at 33˚C (permissive temperature), and were upshifted to the restrictive temperature (39.7˚C) to inactivate RCC1 in late metaphase or immediately following anaphase onset. All of the images co-expressing GFP and mRuby or mCherry probes were spectrally unmixed using the NIS-Elements acquisition software (Nikon), and deconvolved using Autoquant X software (Media Cybernetics). Image files were exported as TIFFs, which were opened with ImageJ (NIH) and converted into maximum intensity Z-stack projections. Projections and merged colour images were then converted into 8-bit images and imported into Illustrator (Adobe) to make figures, or saved as AVI movie files.

2.3.3 Pull-downs, immunoblots and co-sedimentation assays

Purified protein was made from *E. coli* BL21 cells transformed with the following constructs: MBP:anillin (C2; 750-872), MBP:anillin (RBD + C2; 672-940), and MBP:anillin (C-

term; 608-1087) as described previously (Piekny and Glotzer, 2008). NLS mutant MBP-anillin (850 KK 851-DE) was generated in the anillin constructs by quickchange PCR. Bacteria were resuspended in lysis buffer [2.5 mM $MgCl_2$, 50 mM Tris, 150 mM NaCl pH 7.5, 0.5% Triton X-100, 1 mM dithiothreitol (DTT), 1 mM phenylmethanesulfonyl fluoride (PMSF) and 1 X protease inhibitors; Roche], incubated with 1 mg/ml lysozyme on ice for 30 minutes, then sonicated three times. Extracts were incubated with amylose resin (New England Biolabs) for 5 hours at 4˚C with rotation. After washing, protein loaded beads were stored as a 50% slurry at 4˚C or eluted in equivalent volumes of 100 mM maltose on ice for 2 hours. Protein concentration was determined before use.

Microtubules were prepared from lyophilized microtubules (Cytoskeleton) as per the manufacturer's instructions in resuspension buffer (15 mM PIPES, 1 mM $MgCl_2$, 20μM Taxol; Bioshop) at room temperature for 10–15 minutes with gentle mixing. Aliquots of 45.5 μM were flash frozen and stored at -80˚C, then thawed in a circulating water bath and diluted with resuspension buffer to 9.1 μM. Purified anillin proteins were pre-spun by centrifugation at 279,000 g for 25 minutes at room temperature. Co-sedimentation reactions were prepared as described previously (van Oostende Triplet et al., 2014).

Transfected Hela cells were lysed in 50 mM Tris pH7.6, 150 mM NaCl, 5 mM $MgCl_2$, 0.5% Triton X-100, 1 mM DTT, 1mM PMSF with protease inhibitors (Roche) and incubated with 5-10 μg of purified MBP-tagged anillin protein on amylose resin beads at 4°C to pull down Myc:importin-β, Myc:Ect2 C-terminus (422-881) and GFP:RhoA (Q63L). Beads were washed 3–4 X with 50 mM Tris pH7.6, 150 mM NaCl, 5 mM $MgCl_2$ before adding SDS sample buffer to denature the proteins for SDS-PAGE. All pull-downs were run by SDS-PAGE and wet-transferred to nitrocellulose membrane for western blotting. All blots were reversibly stained with Ponceau S

to show total protein. Western blots were treated with either mouse anti-Myc antibodies (clone 9E10; DSHB) used directly or 1:2000 mouse anti-GFP antibodies (Roche). The secondary antibody used for all blots was anti-mouse Alexa 488 (Invitrogen). Blots were scanned at 488 nm using the Typhoon Trio phosphoimager (GE). Images were converted to 8-bit by ImageJ, and made into figures using Adobe Photoshop and Illustrator (Adobe).

2.3.4 Quantification

The breadth and ratios of cortical accumulation for anillin and myosin were performed using ImageJ. Maximum intensity Z-projections were generated for each cell, and the breadth was determined using a line scan drawn along the cell cortex. The breadth was determined as the number of pixels above 50% of the maximum intensity (width of the peak) after subtracting cytosol levels, which was divided by the total number of pixels to give a ratio of breadth to length of cell perimeter. To measure the ratio of cortical accumulation vs. cytosol, the average intensity was determined in an area drawn around the cortex from one pole to the other. This value was then divided by the average fluorescence intensity from a ROI from the cytosol. To measure the asymmetric distribution of GFP-tagged anillin, RhoA and myosin, a line was drawn through chromatin perpendicular to the axis of polarization to bisect the cell. The breadth of accumulation was measured for each half of the cell and a ratio (R) was determined (schematic in **Figure 5A**). Cells with R = [0.7–1.2] were scored as symmetric, while cells with $R > 1.2$ were scored as asymmetric. In cells where there was no visible cortical protrusion, a line was drawn arbitrarily through chromatin. To measure the cortical recruitment of anillin in polarized cells, a line scan was drawn through the central plane of the cell. The ratio (R) of maximum cortical vs. maximum cytosolic levels was determined, and anillin was scored as cortical in cells with $R > 1.1$ (schematic

in **Figure S4A**). To compare the localization of Myc:importin-β and anillin at the equatorial cortex, a line scan was drawn through the cell at the equatorial axis, and their fluorescence levels were compared in a line graph. To measure the nuclear localization of GFP-tagged anillin, the average fluorescence intensity from ROI's in the nucleus and cytosol were measured and a ratio of nuclear vs. cytosolic levels (R) was determined. Cells with $R > 1.3$ were scored as nuclear, while cells with $R < 1.3$ were scored as cytosolic. All data was imported into Excel (Microsoft), where calculations were performed including standard deviations and to generate graphs. All experiments with fixed cells were replicated at least three times and analyzed using the Student's t test, or one-way Anova. Live imaging experiments were replicated a minimum of five times to obtain sufficient n's, which were pooled and statistically analyzed via the Fisher's exact test.

To choose cells with Ran overexpression for analysis in **Figure 4**, the levels of mCherry-tagged Ran were measured in cells co-expressing GFP-tagged anillin. The exposure time and gain were kept constant for Ran vs. Ran Q69L. Cells were determined to have high overexpressed Ran if the levels were above 1,500 and below 3,000, and to have low expression of Ran if the levels were above 460 and below 1,500.

Colocalization measurements between mCherry-tagged Ran and GFP-tagged anillin were performed using the Colocalization Analysis plugin in ImageJ (NIH). The ROI was determined for each region of the cell cortex (as indicated in **Figure S1B**) after background subtraction, and a scatter plot was generated to show the colocalized pixels for varying intensities for each channel. The percentage of colocalized pixels was determined based on the Pearson's coefficient for each cell, and the average for the population was determined. The mean of the averages for multiple cells, and standard deviations were calculated and graphed in Excel (Microsoft).

The expression levels of the constructs used in **Figures 5-8** were determined based on

controls where anillin RNAi cells co-expressing either full-length or C-terminus of anillin were tested for their ability to polarize or rescue cytokinesis, respectively. The imaging parameters used for the rescued cells were optimized to fluorescence intensities between 1,200–3,500 for the GFP channel, and were kept constant for the other constructs to ensure that only cells with sufficient levels of expression were considered.

To assay changes in the localization of GFP-tagged anillin along the cortex during anaphase in relation to chromatin distance, an ImageJ (NIH) macro was written. Briefly, the cortex of a cell was traced at each time point (anaphase onset; 0, 2, 4 and 6 minutes), and a series of 43 points (in total) were drawn around each half of the cell, encompassing 220º. At each point, the shortest distance to a binary mask that described the chromatin was measured, and a circular sampling window of 640 nm diameter was used to measure mean anillin intensity.

All of the images and graphs were transferred to Illustrator (Adobe) to make figures.

2.4 Results

2.4.1 Active Ran spatially regulates cytokinesis

Recent studies have shown that there is a correlation between chromatin position and the localization of cytokinesis proteins (Rodrigues et al., 2015). During mitosis, Ran-GTP forms a gradient around chromatin that regulates proteins required for bipolar spindle assembly (Kaláb et al., 2002; Kaláb et al., 2006; Clarke and Zhang, 2008). This gradient persists into anaphase and we propose that it influences the cortex (Li and Zheng, 2004; Lee et al., 2012). To test the role of Ran in cytokinesis, we determined how decreasing the levels of endogenous active Ran affects the localization of contractile proteins in tsBN2 cells, which contain a ts mutant of RCC1 (Ran GEF) in BHK epithelial cells (Nishimoto et al., 1978). A reduction in Ran-GTP occurs within minutes

of upshift to a restrictive temperature (39.7˚C), and all of our analyses were done after cells were upshifted for 30–40 minutes (Lee et al., 2012). Longer upshifts were detrimental and prevented cells from exiting mitosis, likely due to spindle defects (Kaláb et al., 2002; Kaláb et al., 2006). A significant proportion of tsBN2 cells, 59% for GFP:anillin and 35% for GFP:myosin (MLC; myosin light chain; active), failed to ingress when upshifted to restrictive temperature in comparison with tsBN2 cells at a permissive temperature (33˚C; 0% for GFP:anillin or GFP:myosin), or BHK cells at either temperature (0%, at 39.7 or 33˚C for anillin:GFP; **Figures 3A** and **S1A**). To ensure that the mitotic spindle formed properly in the upshifted cells, we labeled microtubules with Sir-tubulin (in red; **Figure 3A**). Anillin and myosin appeared to be ectopically recruited to regions outside the equatorial plane, so we measured their cortical accumulation. To do this, a line scan was drawn around the perimeter of the cell and the pixels above 50% maximum levels were summed and calculated as a ratio vs. the total perimeter (**Figures 3B** and **S1A**). In tsBN2 cells at restrictive temperature, the ratio of cortical endogenous anillin and GFP:myosin was greater in comparison to cells at permissive temperature (**Figures 3B** and **S1A**). Therefore, decreasing Ran-GTP levels during mitosis causes contractile proteins to be ectopically recruited, likely blocking furrow ingression due to altered cortical properties at the cell poles. However, there is always the caveat that these phenotypes are caused indirectly by spindle perturbations, which can occur when Ran-GTP levels are insufficient. In addition, these phenotypes could be caused by the presence of cortical regulators that should be sequestered to the nucleus, since a reduction in Ran-GTP prevents nuclear envelope reformation (Clarke and Zhang, 2008).

To test whether there is a more direct role for Ran-GTP in regulating cytokinesis, we targeted active Ran to the cleavage furrow membrane. Ran or constitutively active Ran (Q69L) tagged with mCherry were targeted to the equatorial membrane in cells stably expressing

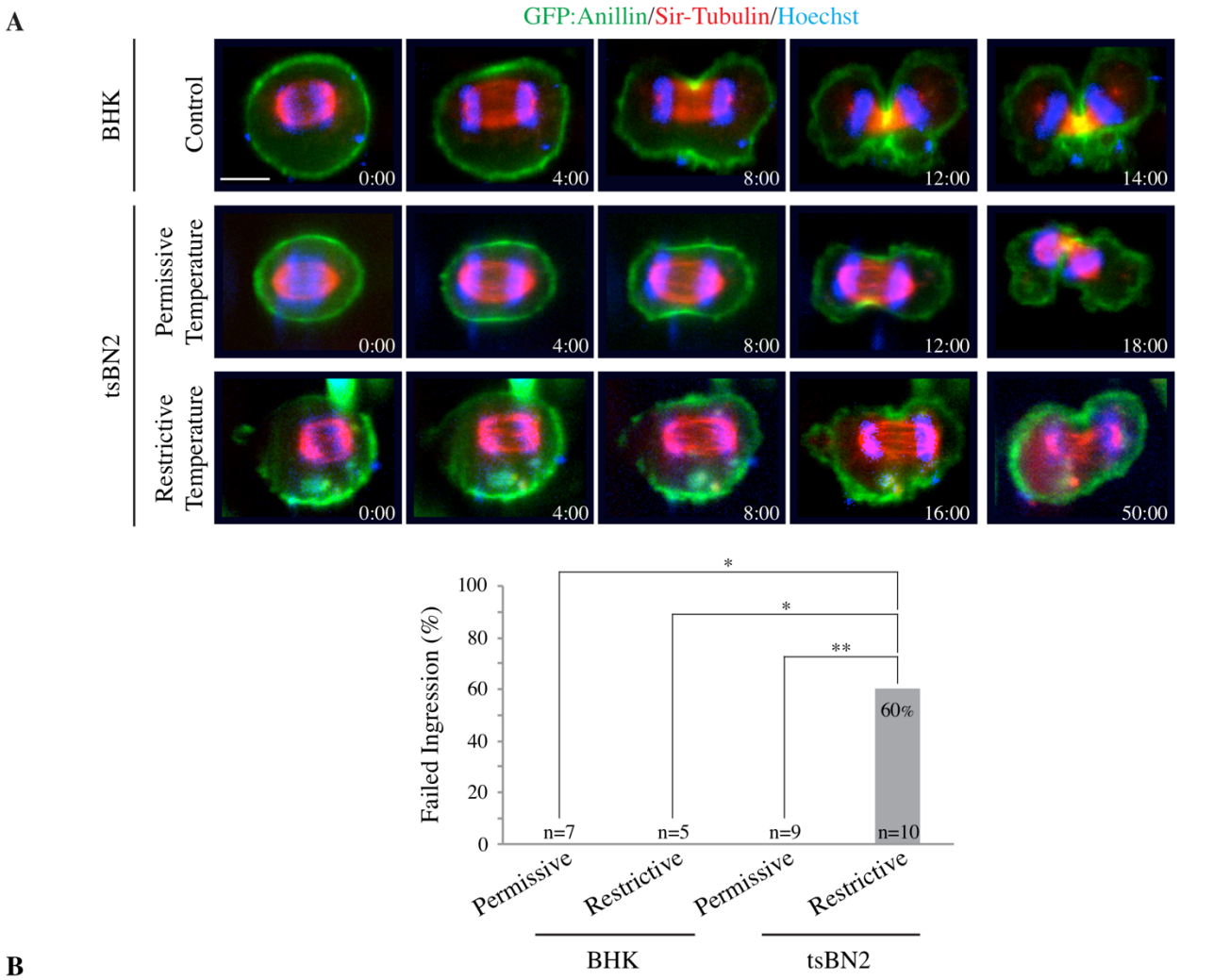
A
GFP:Anillin/Sir-Tubulin/Hoechst
BHK
Control
tsBN2
Permissive Temperature
Restrictive Temperature
0:00
4:00
8:00
12:00
14:00
18:00
16:00
50:00
Failed Ingression (%)
100
80
60
40
20
0
*
*
**
60%
n=7
n=5
n=9
n=10
Permissive
Restrictive
Permissive
Restrictive
BHK
tsBN2
B
Ratio of Total Cortical Anillin vs. Perimeter = A +B+C+D / Linescan
D
C
B
A
Linescan
Width at 1/2 Max
Anillin Fluorescence Intensity (a.u.)
5000
4000
3000
2000
1000
A
B
C
D
Cytosol
0
20
40
60
80
100
120
140
160
Length (pixels)
Ratio of Cortical Anillin vs. Perimeter
0.90
0.70
0.50
0.30
0.10
**
0.14
0.39
Permissive Temperature
Restrictive Temperature
tsBN2

Figure 3. Reducing active Ran affects the localization of contractile proteins during cytokinesis

A) Timelapse images show BHK and tsBN2 [BHK with a ts mutation in RCC1 (Ran GEF)] cells, expressing GFP:anillin (green), treated with Sir-tubulin (red) and Hoechst (stains DNA; blue) during cytokinesis at permissive (33°C) and restrictive temperatures (39.7°C). The scale bar is 10 μm. A bar graph shows the proportions of cytokinesis phenotypes observed for the different cell types and conditions. The data was analyzed using Fisher's exact test (* $p < 0.05$; ** $p < 0.01$) and the n's are indicated on the graph. **B**) Schematic shows how cortical anillin accumulation was measured. Line graph shows a cortical line scan of anillin:GFP around the cell perimeter, with the length (pixels) on the X axis and fluorescence intensity (a.u.) on the Y axis. Regions of the cortex with anillin above 50% maximum levels were summed together to generate the total breadth of accumulated anillin. Dot plot shows the ratio of accumulated anillin to cell perimeter for tsBN2 cells at permissive (n=9) or restrictive temperature (n=16). The means are indicated, and the data were analyzed using Student's t test (** $p < 0.01$).

anillin:GFP using the phosphatidylinositol 4,5-bisphosphate ($PI4,5P_2$)-binding domain of neuromodulin (1-60 a.a.; Liu et al., 2012). Cytokinesis phenotypes were observed in cells strongly overexpressing active Ran (fluorescence intensity 1,500–3,000 a.u.), which were separated into categories of weak cortical instability, such as blebbing or ruffling (39%), and oscillation (35%), where the furrow failed to remain stably positioned (**Figure 4A**). Cells weakly overexpressing active Ran (460–1,500 a.u.) also displayed weak cortical instability (54%), while only a small proportion of cells strongly overexpressing Ran displayed weak cortical instability (23%; **Figure 4A**). Furrow oscillation and cortical instability are reminiscent of the phenotypes reported for anillin depletion in HeLa cells (Straight et al., 2005; Piekny and Glotzer, 2008), suggesting that active Ran negatively regulates anillin function. We also determined if the overexpression of Ran or Ran (Q69L) is sufficient to cause phenotypes without being targeted to the membrane (**Figure S1B**). No cytokinesis phenotypes were observed in cells overexpressing GFP:Ran or GFP:Ran (Q69L), however, there may be a mild increase in the breadth of anillin in cells overexpressing active Ran (**Figure S1B**). To determine if membrane-targeted active Ran affects anillin localization, we measured the ratio of cortically accumulated anillin to cytosol (**Figure S1C**), and the ratio of anillin breadth to cell perimeter just prior to furrow ingression (**Figure 4B**; Zanin et al., 2013). There was no significant change in the total levels of cortical anillin in membrane-targeted active Ran versus Ran or control cells (**Figure S1C**). However, there was a significant increase in the breadth of anillin in the equatorial plane in cells where membrane-targeted active Ran was highly overexpressed (**Figure 4B**). This data suggests that there is less anillin in the equatorial plane in cells expressing membrane-targeted active Ran. Therefore, targeting active Ran to the membrane may cause insufficient levels of anillin to persist in the equatorial plane to stabilize the ring. To ensure that membrane-targeted Ran overlapped with anillin, we measured

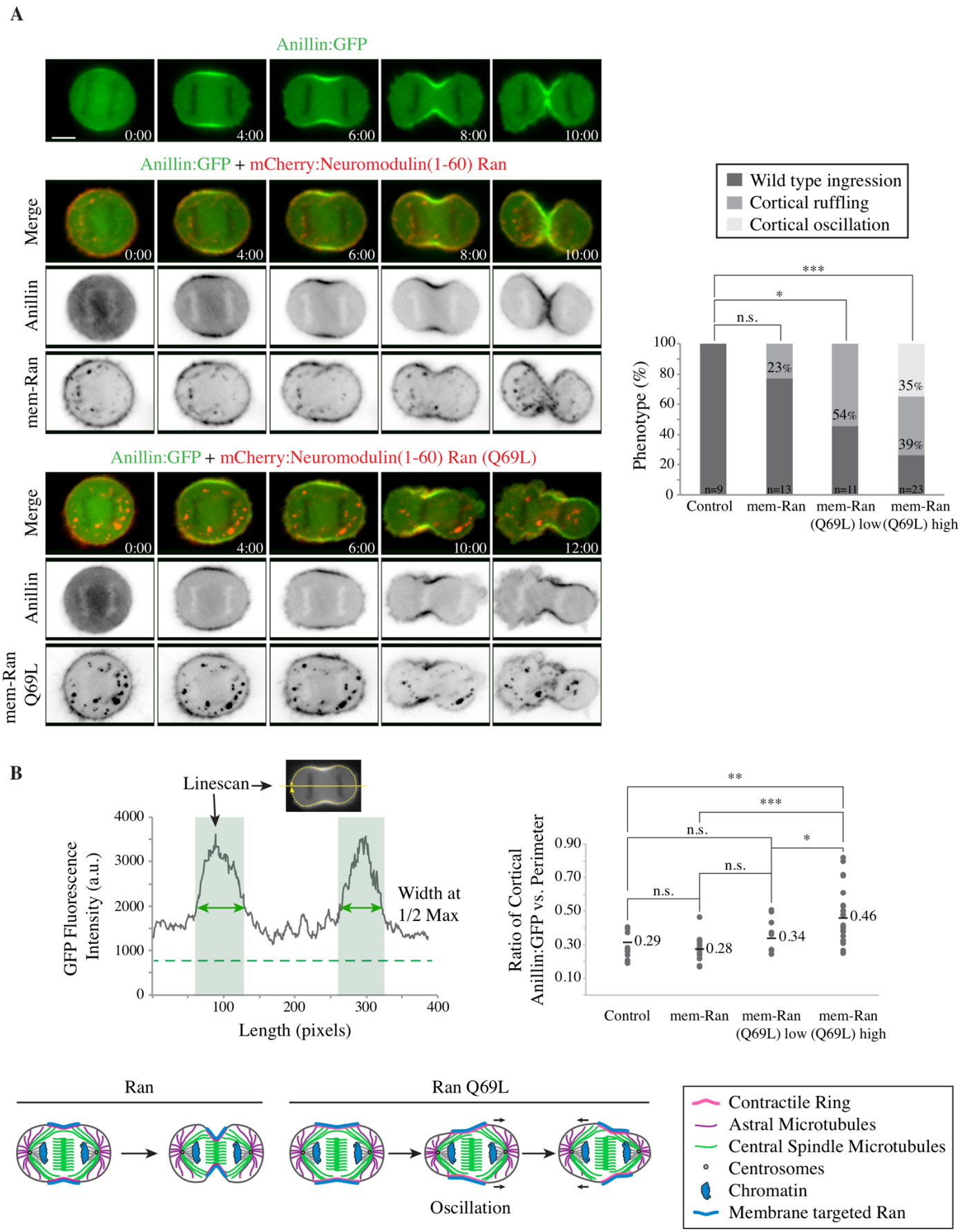
A
Anillin:GFP
0:00
4:00
6:00
8:00
10:00
Anillin:GFP + mCherry:Neuromodulin(1-60) Ran
Merge
Anillin
mem-Ran
Anillin:GFP + mCherry:Neuromodulin(1-60) Ran (Q69L)
12:00
mem-Ran Q69L
Wild type ingression
Cortical ruffling
Cortical oscillation
Phenotype (%)
n.s.
*
***
23%
54%
39%
35%
n=9
n=13
n=11
n=23
Control
mem-Ran
mem-Ran (Q69L) low
mem-Ran (Q69L) high
B
Linescan
GFP Fluorescence Intensity (a.u.)
Length (pixels)
Width at 1/2 Max
Ratio of Cortical Anillin:GFP vs. Perimeter
**
0.29
0.28
0.34
0.46
Ran
Ran Q69L
Oscillation
Contractile Ring
Astral Microtubules
Central Spindle Microtubules
Centrosomes
Chromatin
Membrane targeted Ran

Figure 4. Furrow-localized active Ran causes cytokinesis phenotypes

A) Timelapse images show HeLa cells expressing anillin:GFP (green; top panel), or co-expressing anillin:GFP and mCherry:Ran (mem-Ran; red; 1,500–3,000 a.u.; middle panels) or RanQ69L [mem-Ran(Q69L); 1,500–3,000 a.u.; bottom panels] fused to the phospholipid-binding domain of Neuromodulin (1-60) during cytokinesis. The scale bar is 10 μm. To the right, a bar graph shows the proportions of cytokinesis phenotypes observed in the different cells, as indicated. Cells co-expressing anillin:GFP and low levels of mem-RanQ69L (460–1,500 a.u.) were also included in the analysis. The data was analyzed using Fisher's exact test (n.s., not significant, * $p < 0.05$, *** $p < 0.001$) and the n's are indicated on the graph. **B**) Line graph shows a cortical line scan of anillin:GFP around the cell perimeter, with the length (pixels) on the X axis and fluorescence intensity (a.u.) on the Y axis. The width of the peak at 50% maximal levels of intensity represents breadth. Dot plot shows changes in the ratio of the breadth of anillin to cell perimeter for control (n=9), membrane-targeted Ran (n=13), low expressing membrane-targeted Ran (Q69L; n=11) and membrane-targeted Ran (Q69L; n=23). The means are indicated, and p values were determined by Student's t test (n.s., not significant, * $p < 0.05$, ** $p < 0.01$, *** $p < 0.001$). At the bottom, cartoon schematics show the oscillation phenotype observed in cells overexpressing membrane-targeted Ran (Q69L). The components of the cell are shown in the legend.

colocalization between Ran and anillin in cells at the onset of furrow ingression, which ranged from 40–98% for Ran and Ran (Q69L; **Figure S1D**).

2.4.2 Anillin is a target of the Ran pathway

To find a target of the Ran pathway, we determined which of the known regulators of cytokinesis are required to polarize the cortex in response to chromatin. First, we verified that Ran polarizes the cortex in HeLa cells lacking polymerized microtubules and induced to exit mitosis (Kiyomitsu and Cheeseman, 2013). HeLa cells display cortical contractility after treatment with 100 nM Nocodazole for 3-4 hours to depolymerize microtubules, followed by 22.5 μM Purvalanol A to inhibit Cdk1 activity and promote mitotic exit (*e.g.* **Figures S2A** and **5A**; Petronczki et al., 2007). Contractile proteins accumulate around the region of the cortex furthest from chromatin causing cells to polarize. This polarization is reminiscent of that in monopolar cells treated with S-trityl-L-cysteine (STC) to block centrosome separation and forced to exit mitosis (**Figure S2A**; Hu et al., 2008). To show that cortical polarity is influenced by Ran, HeLa cells lacking polymerized microtubules and induced to exit mitosis were treated with 100 nM Importazole, which was previously shown to disrupt Ran-GTP-importin binding (**Figure S2B**; Soderholm et al., 2011). Cells were assayed for polarization by measuring asymmetric anillin distribution. Anillin was determined to be asymmetric if the ratio (R) of accumulated anillin around part of the cortex, perpendicular to the axis of chromatin position, deviated from the other part by $R > 1.2$ (see schematic in **Figure 5A**). Indeed, while anillin was asymmetric in 53% of control cells, it was not asymmetrically distributed in the majority of Importazole-treated cells (14%; **Figure S2B**), consistent with previous studies showing that the Ran pathway influences the localization of contractile proteins during mitotic exit (Kiyomitsu and Cheeseman, 2013).

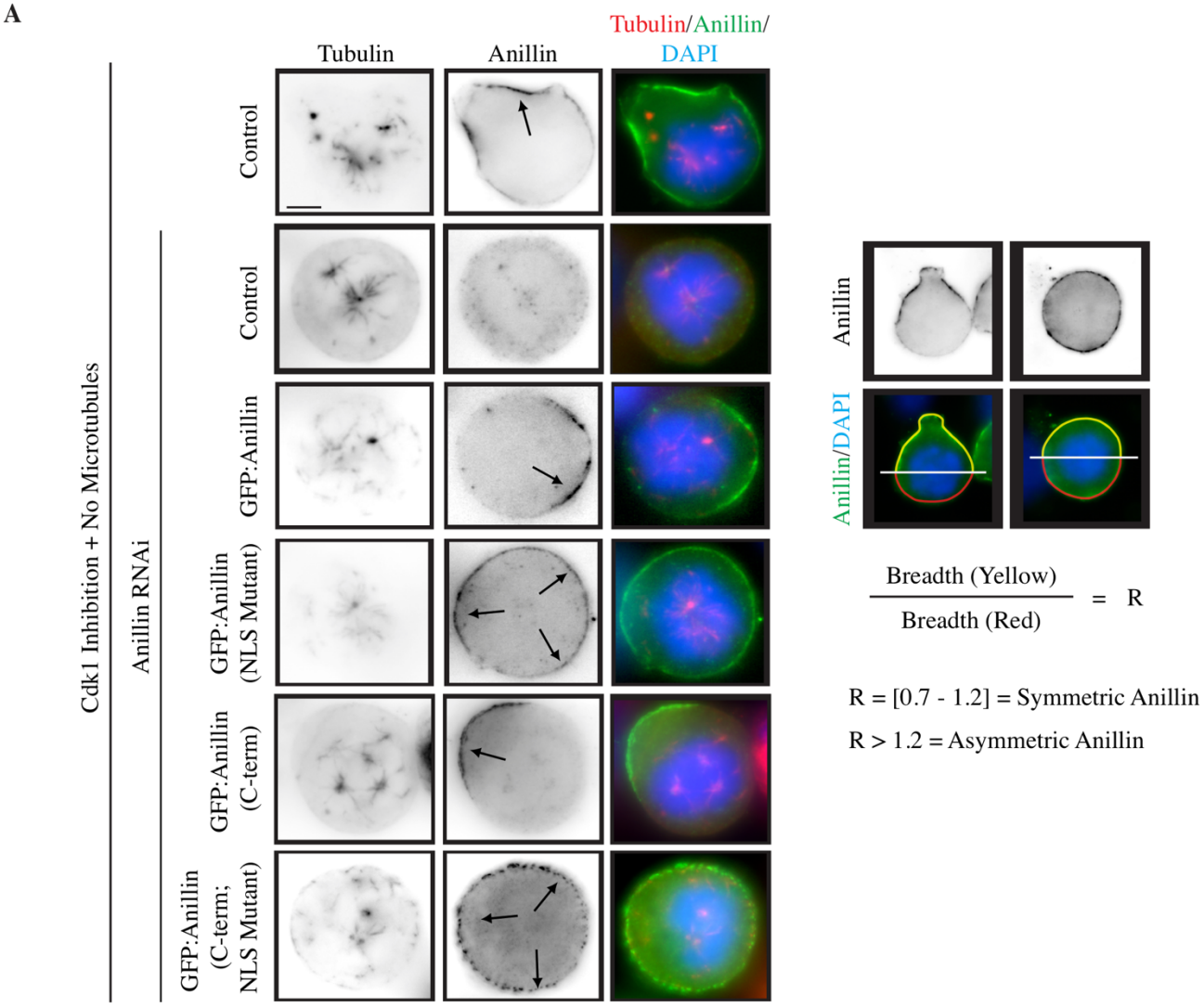
A
Tubulin/Anillin/
DAPI
Tubulin
Anillin
Cdk1 Inhibition + No Microtubules
Anillin RNAi
Control
Control
GFP:Anillin
GFP:Anillin
(NLS Mutant)
GFP:Anillin
(C-term)
GFP:Anillin
(C-term;
NLS Mutant)
Anillin
Anillin/DAPI
Breadth (Yellow)
Breadth (Red)
= R
R = [0.7 - 1.2] = Symmetric Anillin
R > 1.2 = Asymmetric Anillin

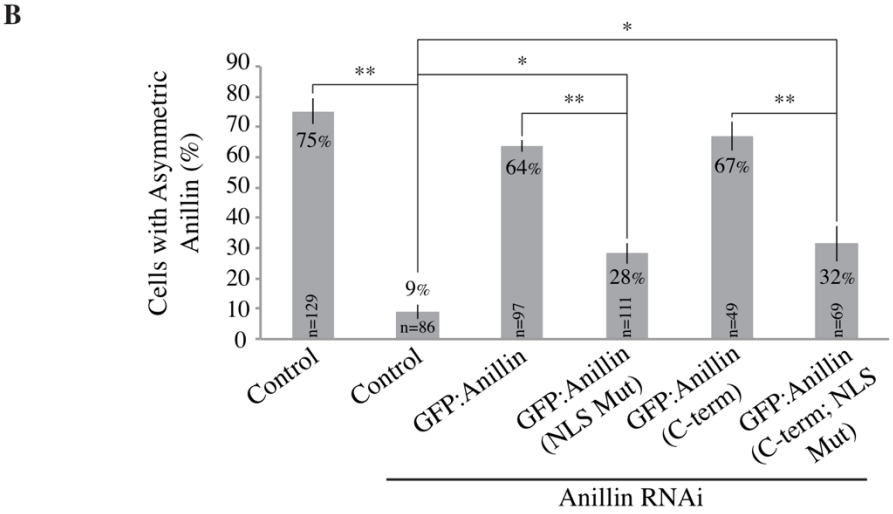
B
Cells with Asymmetric Anillin (%)
90
80
70
60
50
40
30
20
10
0
**
*
*
**
**
75%
9%
64%
28%
67%
32%
n=129
n=86
n=97
n=111
n=49
n=69
Control
Control
GFP:Anillin
GFP:Anillin
(NLS Mut)
GFP:Anillin
(C-term)
GFP:Anillin
(C-term; NLS
Mut)
Anillin RNAi

Figure 5. Anillin is required for cortical polarity in the absence of polymerized microtubules

A) Images show fixed HeLa cells treated with anillin RNAi and co-expressing RNAi-resistant full-length GFP:anillin, (1-1087) or C-terminal GFP:anillin (608-1087; C-term) with or without mutations in the C-terminal NLS (850 KK 851- DE; NLS Mutant), treated with 100 nM nocodazole and 22.5 μM Purvalanol A to depolymerize microtubules and induce mitotic exit, respectively. Cells were co-stained for endogenous anillin or GFP (green), tubulin (red) and DAPI (chromatin; blue). Black arrows indicate regions of the cortex where anillin accumulates. The scale bar is 10 μm. To the right is a schematic to show how anillin's cortical localization was determined to be asymmetric. In cells where the cortex was polarized, a line was drawn through chromatin, perpendicular to the axis of polarization. Line scans were drawn around the cortex in each region (*e.g.* red vs. yellow) to measure the accumulation of anillin. In cells where the cortex was round, a line was drawn arbitrarily through chromatin, and each side was measured. The ratio R of accumulated anillin was determined, and $R > 1.2$ was defined as asymmetric. **B**) Bar graph shows the percentage of cells with asymmetric anillin distribution after rescue with the different anillin constructs as indicated. Bars show SD, and p values were determined by Student's t test (* $p < 0.05$, ** $p < 0.01$). The n's are indicated on the graph.

Next, we monitored changes in cortical polarization after cells were treated with different small interfering RNAs (siRNAs) or drugs to deplete or inhibit known cytokinesis regulators (**Figure S2C**). Depleting Ect2 blocked the cortical recruitment of anillin:GFP, consistent with its requirement to generate active RhoA for contractile ring assembly (5% asymmetric vs. 61% control; Yüce et al., 2005). Inhibiting myosin with Blebbistatin had no effect on polarization and anillin:GFP localized asymmetrically in response to chromatin (62% when Blebbistatin was added 'early' with Purvalanol A, and 68% when Blebbistatin was added 'late' ~7 minutes after Purvalanol A; **Figure S2C**). However, in anillin-depleted cells, myosin and RhoA were globally localized regardless of chromatin position, and the majority of cells failed to polarize (10 and 3%, respectively vs. 56% GFP:myosin and 65% GFP:RhoA; **Figure S2C**). Asymmetric anillin distribution and cortical polarization was restored in anillin-depleted cells co-expressing GFP-tagged RNA interference (RNAi)-resistant full-length (FL) or C-terminus (C-term) of anillin (75% for endogenous anillin and 9% after anillin RNAi vs. 64% for anillin RNAi + FL anillin (1-1087), and 67% for anillin RNAi + C-term (608-1087; **Figures 5A**, **B**), suggesting that anillin's N-terminal actin and myosin binding sites are not needed for polarization. These data show that the cortical polarization of cells lacking polymerized microtubules is regulated by anillin or upstream regulators of anillin, as shown in the schematic in **Figure S2D**.

We determined the molecular mechanism by which anillin mediates polarization in response to Ran-GTP. Human anillin contains an NLS at its C-terminus, but this site has not been extensively studied (Oegema et al., 2000). A NLS at the C-terminus of *Drosophila* anillin overlaps with a putative septin-binding region and was shown to bind to importins *in vitro* (Silverman-Gavrila et al., 2008). It was hypothesized that importins released in the vicinity of chromatin-associated Ran-GTP during cellularization permit anillin to form a functional complex with septins

at the nearby cortex (Silverman-Gavrila et al., 2008). However, it is not clear how this model fits with other published data showing that Ran-GTP inhibits rather than promotes anillin's cortical localization during mitotic exit (Kiyomitsu and Cheeseman, 2013). Our data are consistent with the hypothesis that Ran-GTP negatively regulates anillin's cortical localization. However, in addition to using *Drosophila* rather than mammalian cells, different methods were used (gain-of-function vs. loss-of-function), and the model could be more complex than either study revealed.

The NLS in human anillin maps to a disordered loop emanating from the C2 domain at the C-terminus (Sun et al., 2015). To determine if the C-terminal NLS in human anillin is functional, we expressed different GFP-tagged anillin constructs and monitored nuclear localization in interphase HeLa cells (**Figure 6A**). Nuclear localization was determined to be positive if the ratio of GFP in the nucleus to that in the cytosol was > 1.3, and only cells with levels > 1,200 a.u. were considered (*see* **Figure S3A**). The full length and the N-terminus of anillin (1-460) were previously reported to localize to the nucleus in interphase cells (*e.g.* **Figure 6A**; Oegema et al., 2000; Chen et al., 2015). The C-terminus (608-1087; RhoA-GTP binding domain -RBD + C2 + Pleckstrin Homology domain -PH), and a fragment containing the N-terminal actin and myosin domains, and the C-terminal PH domain are nonnuclear (*e.g.* **Figure 6A**; Piekny and Glotzer, 2008; Chen et al., 2015). We found that a fragment lacking the RBD (748-1087; C2 + PH) was nuclear (**Figure 6A**). The localization of C-terminal fragments to the nucleus had been previously reported, but it was not clear why some fragments localized more strongly than others (Oegema et al., 2000). We propose that the C-terminal NLS is inhibited intramolecularly by the RBD during interphase. Treating cells with 100 nM Importazole for 8 h decreased nuclear localization of the C2 + PH fragment, while point mutations in the NLS (850 KK 851- DE) blocked nuclear localization altogether (**Figure 6A**). Higher concentrations of Importazole were not used, because it affected

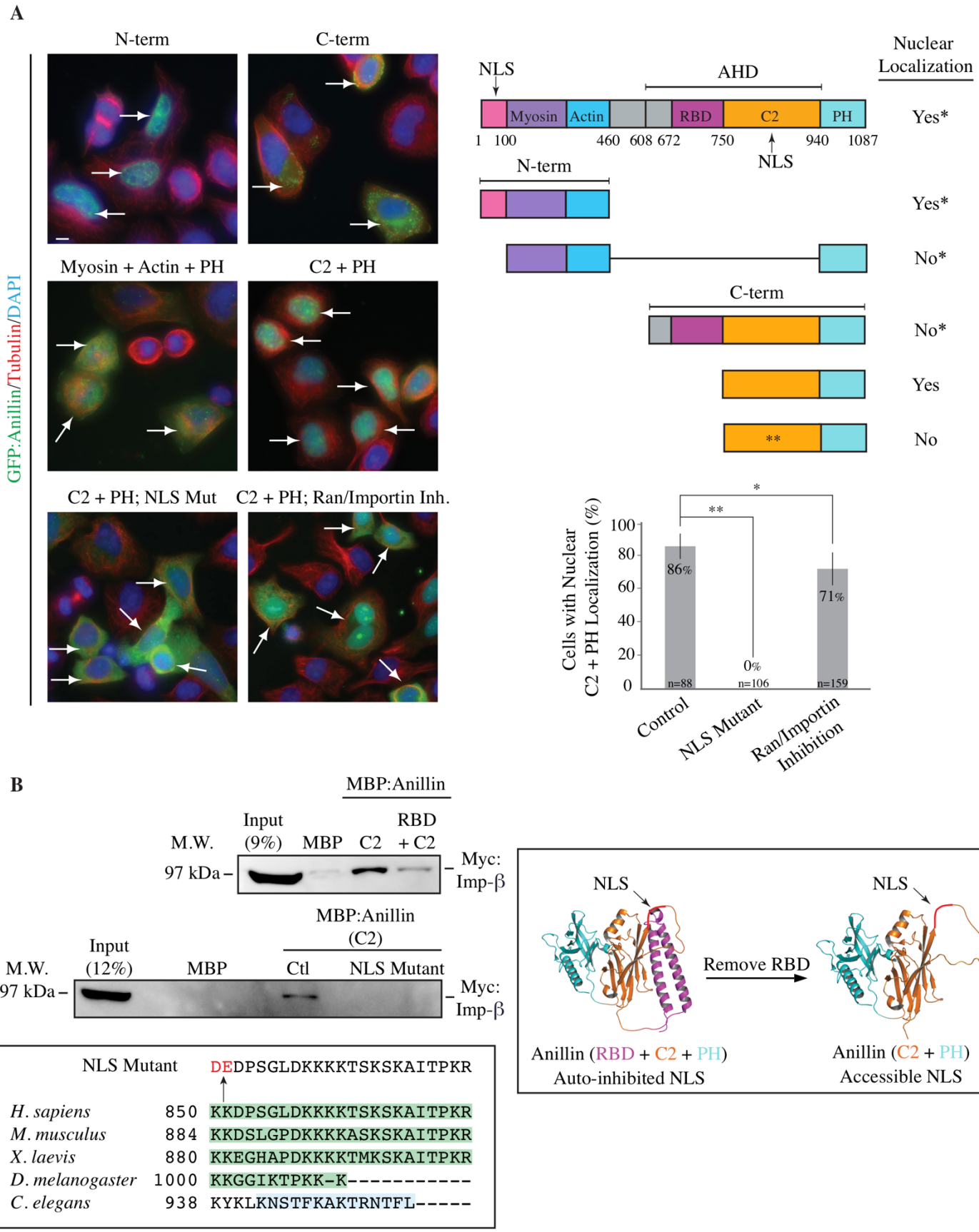
A
N-term
C-term
Myosin + Actin + PH
C2 + PH
C2 + PH; NLS Mut
C2 + PH; Ran/Importin Inh.
GFP:Anillin/Tubulin/DAPI
Nuclear Localization
NLS
AHD
Myosin
Actin
RBD
C2
PH
1 100 460 608 672 750 940 1087
NLS
N-term
Yes*
Yes*
No*
C-term
No*
Yes
No
**
Cells with Nuclear C2 + PH Localization (%)
100
80
60
40
20
0
*
**
86%
0%
71%
n=88
n=106
n=159
Control
NLS Mutant
Ran/Importin Inhibition
B
MBP:Anillin
Input (9%)
MBP
C2
RBD + C2
M.W.
97 kDa
Myc: Imp-β
MBP:Anillin (C2)
Input (12%)
MBP
Ctl
NLS Mutant
M.W.
97 kDa
Myc: Imp-β
NLS Mutant DEDPSGLDKKKKTSKSKAITPKR
H. sapiens 850 KKDPSGLDKKKKTSKSKAITPKR
M. musculus 884 KKDSLGPDKKKKASKSKAITPKR
X. laevis 880 KKEGHAPDKKKKTMKSKAITPKR
D. melanogaster 1000 KKGGIKTPKK-K----------
C. elegans 938 KYKLKNSTFKAKTRNTFL-----
NLS
NLS
Remove RBD
Anillin (RBD + C2 + PH)
Auto-inhibited NLS
Anillin (C2 + PH)
Accessible NLS

Figure 6. Anillin contains a functional NLS in its C-terminus

A) Images show fixed HeLa cells expressing GFP:anillin constructs co-stained for GFP (green), tubulin (red) and DAPI (chromatin; blue). White arrows indicate cells with expression levels above 1,200 levels. The scale bar is 10 μm. To the right, a schematic shows the structure of anillin, with its binding domains in different colors [myosin (purple); actin (blue); RBD, RhoA-GTP Binding Domain (dark pink); C2 (orange); PH, Pleckstrin Homology; cyan] and corresponding amino acid numbers, as well as the locations of the N-terminal and C-terminal NLSs, and point mutations within the C-terminal NLS as indicated (**). The AHD (Anillin Homology domain) is also shown. Constructs that localize to the nucleus are indicated as 'yes' or 'no' based on previous studies (* *e.g*. Oegema et al., 2000; Piekny et al., 2008; Chen et al., 2015), or this study. Underneath, a bar graph shows the percentage of cells with nuclear anillin (C2 + PH). Bars show SD, and *p* values were determined by Student's t test (* $p < 0.05$, ** $p < 0.01$). The n's are indicated on the graph. **B**) Immunoblots show pull-downs of Myc:importin-β from lysates with purified MBP and MBP-tagged anillin proteins as indicated (C2 vs. RBD + C2, and C2 vs. C2 NLS mutant). An alignment of the C-terminal NLS is shown for human (*Homo sapiens*) anillin with mouse (*Mus musculus*), frog (*Xenopus laevis*), *Drosophila* (*D. melanogaster*) and *C. elegans*. Sequences highlighted in green are strongly predicted to be NLSs, or have been shown to bind to importins (Silverman-Gavrila et al., 2008), while the amino acids highlighted in blue are weakly predicted to be NLSs. The box to the right shows structures for the RBD, C2 and PH (modified from Sun et al., 2015), to demonstrate how the NLS in the C2 domain of anillin may be intramolecularly inhibited by the RBD.

cell viability. These data suggest that the C-terminal NLS of anillin is responsive to the Ran pathway for nuclear import.

We further assessed if the C-terminal NLS could respond to Ran via binding to importins. This site matches the consensus sequence of a classical bi-partite NLS, which binds to importin-β to mediate nuclear entry, and is highly conserved among vertebrates (**Figure 6B**; Soniat and Chook, 2015). As mentioned above, the C-terminal NLS also appears to be conserved in *Drosophila*, where it has been shown to bind to importins. However, it is not clear if this conservation extends to *Caenorhabditis elegans*, as the sequence is more divergent. We pulled down Myc-tagged importin-β from cell lysates using recombinant MBP-tagged human anillin constructs that contained or lacked the RBD (**Figures S3B, C,** and **6B**). As expected, Myc:importin-β localized to the periphery of the nucleus and cytosol in HeLa cells (**Figure S3B**). Myc:importin-β bound weakly to an anillin fragment containing the RBD, but bound more strongly to a fragment lacking the RBD, and mutations in the C-terminal NLS (850 KK 851- DE) abolished binding altogether (**Figures S3C** and **6B**). These mutations did not impart gross structural changes in the C-terminus of anillin, because Ect2 and RhoA binding were not affected (**Figure S3D**; Piekny and Glotzer, 2008; Frenette et al., 2012).

2.4.3 The C-terminal NLS of anillin regulates polarization and cytokinesis

Next, we determined the function of anillin's C-terminal NLS in cortical polarity. To do this, rescue assays were performed expressing GFP-tagged RNAi-resistant full-length or C-terminal anillin constructs with the NLS point mutations described above (850 KK 851- DE; NLS mutant) in anillin-depleted cells lacking polymerized microtubules and forced to exit mitosis (**Figure 5A**). Cells were assessed 25 min after Cdk1 inhibition, when the majority of control cells

had sufficient time to polarize. As described earlier, while the proportion of polarized cells with asymmetric anillin was restored in cells expressing nonmutant anillin constructs (64% for FL and 67% for C-term), cells failed to polarize with NLS mutant anillin (28% for FL and 32% for C-term; **Figures 5A, B**). Because Ran-GTP may affect anillin during earlier stages of mitotic exit, we repeated this assay, but examined cells 15 min after Cdk1 inhibition. At this time, the majority of control cells were not polarized, but anillin was cortically recruited (**Figure S4A**). To measure cortical localization, line scans were drawn across the central plane of the cell and the maximum levels of cortical anillin were compared to the cytosol (**Figure S4A**). Anillin was considered to be cortical if the ratio of cortical to cytosolic anillin was > 1.1 (**Figure S4A**). Indeed, while anillin was recruited cortically in 96% of control cells and in 84% of anillin-depleted cells co-expressing RNAi-resistant GFP:anillin (FL), NLS mutant anillin was cortical in only 29% of the cells (**Figure S4A**). Together, these data suggest that the C-terminal NLS of anillin is needed for cortical recruitment during early stages of polarization, and also to polarize cells in the absence of microtubules. The ability of the mutant constructs to localize cortically during later time points suggests that other proteins and/or lipids are sufficient to recruit anillin to the cortex.

Next, we determined whether the C-terminal NLS of anillin is required for cytokinesis. GFP-tagged RNAi-resistant FL or NLS mutant anillin was expressed in anillin-depleted cells co-expressing H2B:mRuby to visualize chromatin, and cells were imaged during cytokinesis (**Figure 7A**). Anillin accumulated along the equatorial cortex ~2 min after anaphase onset, which narrowed as the contractile ring ingressed to pinch in the cell (**Figures 7A, B**). However, mutant anillin was recruited ~6 minutes after anaphase onset to a narrow region, and cytokinesis failed in a larger number of cells (33% vs. 12% for control cells; **Figures 7A, B**). Interestingly, although this delay in accumulation correlated with an overall delay in ingression, once mutant anillin was

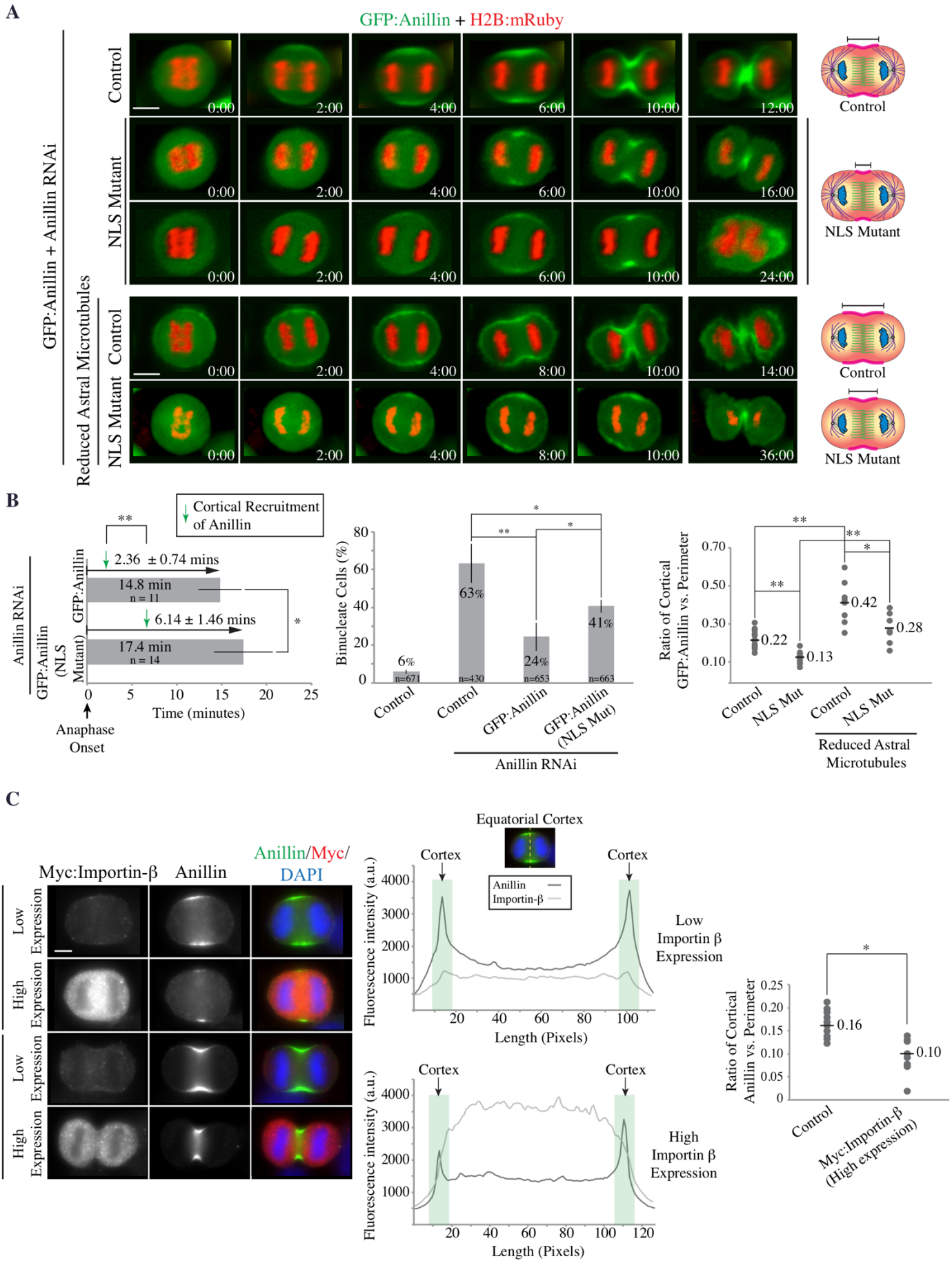
A
GFP:Anillin + H2B:mRuby
GFP:Anillin + Anillin RNAi
Reduced Astral Microtubules
Control
NLS Mutant
Control
NLS Mutant
Control
NLS Mutant
B
Cortical Recruitment of Anillin
Anillin RNAi
GFP:Anillin
GFP:Anillin (NLS Mutant)
2.36 ± 0.74 mins
14.8 min
n = 11
6.14 ± 1.46 mins
17.4 min
n = 14
Time (minutes)
Anaphase Onset
Binucleate Cells (%)
6%
63%
24%
41%
n=671
n=430
n=653
n=663
Control
Control
GFP:Anillin
GFP:Anillin (NLS Mut)
Anillin RNAi
Ratio of Cortical GFP:Anillin vs. Perimeter
0.22
0.13
0.42
0.28
Control
NLS Mut
Control
NLS Mut
Reduced Astral Microtubules
C
Myc:Importin-β
Anillin
Anillin/Myc/ DAPI
Anaphase
Telophase
Low Expression
High Expression
Low Expression
High Expression
Equatorial Cortex
Anillin
Importin-β
Cortex
Cortex
Fluorescence intensity (a.u.)
Length (Pixels)
Low Importin β Expression
High Importin β Expression
Ratio of Cortical Anillin vs. Perimeter
0.16
0.10
Control
Myc:Importin-β (High expression)

Figure 7. The C-terminal NLS regulates anillin's function during cytokinesis

A) Timelapse images show HeLa cells depleted of anillin, expressing GFP-tagged RNAi-resistant nonmutant (n=17) or NLS mutant anillin (n=21) co-expressing H2B:mRuby. Also shown are cells after treatment with 33 nM nocodazole to reduce astral microtubules (n=7 for nonmutant and n=7 for mutant anillin). Cartoon cells to the right show changes in the distribution of anillin under the different conditions. The scale bar is 10 μm. **B**) Bar graph shows a comparison of the timing of anillin recruitment (green arrow) and time from anaphase onset to complete furrow ingression for anillin-depleted cells rescued with nonmutant anillin in comparison with NLS mutant anillin from anaphase onset. SDs are shown as bars and as time for cortical recruitment, and the data was analyzed by Student's t test (* $p < 0.05$, ** $p < 0.01$). The n's are shown on the graph. A bar graph in the middle shows the percentage of binucleate cells ± anillin RNAi and after rescue with GFP-tagged RNAi-resistant nonmutant or NLS mutant anillin. The bars show SD, and p values were determined by Student's t test (* $p < 0.05$, ** $p < 0.01$). The n's are indicated on the graph. The dot plot to the right shows changes in the ratio of the breadth of anillin to cell perimeter in anillin-depleted cells rescued with nonmutant (n=15) or NLS mutant anillin (n=21), and after treatment with nocodazole to reduce astral microtubules (n=7 for wt and n=7 for NLS mutant). The means are indicated, and the data were analyzed by Student's t test (* $p < 0.05$, ** $p < 0.01$). **C**) Images show fixed cells expressing Myc:importin-β (red), co-stained for anillin (green) and DAPI (blue) in anaphase or during furrow ingression (telophase) as indicated. Line scans show the levels of anillin vs. Myc across the equatorial plane (dotted yellow line) in a cell with low levels of Myc (< 1,000 a.u.; top) or high levels of Myc (1,500–4,000 a.u.; bottom), with length (pixels) on the X axis and fluorescence intensity (a.u.; dark grey = anillin, light grey = importin-β) on the Y axis. The green rectangles highlight regions of the equatorial cortex. To the right is a dot plot of the

ratio of the breadth of anillin to the perimeter in cells with low (control, n=11) vs. high Myc (n=9). The data were analyzed by Student's t test (* $p < 0.05$).

recruited, the time from accumulation to ingression did not vary in comparison with that in nonmutant anillin (**Figure 7B**). To further test the requirement of the C-terminal NLS in cytokinesis, we also performed rescue assays in asynchronous populations of cells and calculated the proportion of cells that were binucleate and failed cytokinesis. Anillin depletion caused cytokinesis failure (63% vs. 6% untreated cells; **Figure 7B**), while expression of RNAi-resistant full-length anillin restored cytokinesis in the majority of cells, consistent with previous studies (24%; **Figure 7B**; Piekny and Glotzer, 2008). However, a higher proportion of cells expressing RNAi-resistant NLS mutant anillin failed cytokinesis (41%; **Figure 7B**), supporting the conclusion that the C-terminal NLS is at least partially required for cytokinesis.

To further characterize the effect of the NLS mutations on anillin localization, changes in the breadth of nonmutant versus mutant anillin were quantified by measuring the ratio of cortical anillin to cell perimeter. Mutant anillin was narrower than nonmutant anillin (**Figure 7B**), although the peak of intensity was comparable (unpublished data). A C-terminal anillin construct containing the NLS mutations also appeared to localize with a narrower breadth than in nonmutant anillin (unpublished data). Collectively, these data suggest that the C-terminal NLS is needed to mediate anillin's recruitment and distribution at the equatorial cortex during anaphase for optimal contractile ring ingression. To show that pools of importin-β localize to the equatorial cortex, line scans were drawn across the equatorial plane, and Myc:importin-β levels were compared with those of endogenous anillin (**Figure 7C**). Indeed, the two proteins overlapped at cortical peaks in the equatorial plane (**Figure 7C**). However, we were surprised to see that the overexpression of Myc:importin-β (levels 1,500–4,000 a.u.) decreased the breadth of endogenous anillin (**Figure 7C**). As described earlier, a previous study found that there was competition between importin-α and a putative septin binding site in the C-terminus of *Drosophila* anillin (Silverman-Gavrila et

al., 2008). Therefore, high levels of importin-β could similarly hinder the binding of proteins and/or lipids to the C-terminus of human anillin. Together, our data suggests that free importins (*e.g.* not bound to Ran-GTP) may function as a molecular ruler for anillin, where optimal levels facilitate recruitment, as opposed to when levels are too low or high.

The timing of Ran-regulation of anillin likely occurs during anaphase, prior to furrow ingression. During this time, sister chromatids move toward the poles, where Ran-GTP levels influence anillin's cortical recruitment and localization in the equatorial plane via importins. To further test this model, we compared the temporal and spatial accumulation of nonmutant and mutant anillin in relation to chromatin position. As with the experiments above, cells were depleted of endogenous anillin and rescued with GFP-tagged RNAi-resistant nonmutant vs. mutant anillin. An ImageJ (National Institute of Health) macro was written to sample the intensity of anillin (in a circular region of interest [ROI] 320 nm in radius) at 43 evenly spaced points around the cortex, as well as the distance from these points to the closest point of a mask describing chromatin (see cartoon, **Figure 8A**). Measurements were taken every 2 min from anaphase onset until 6 min after, and the data from five cells for nonmutant vs. mutant anillin was averaged and graphed (**Figure 8A**). Consistent with our model, the accumulation and clearance of cortical nonmutant anillin strongly correlated with changes in chromatin distance (**Figure 8A**). However, there was no correlation with mutant anillin until 6 min after anaphase onset, when the central spindle likely promotes the accumulation of active RhoA and anillin in the equatorial plane (van Oostende Triplet et al., 2014). These data suggest that the localization of mutant anillin likely is not influenced by chromatin or Ran-GTP.

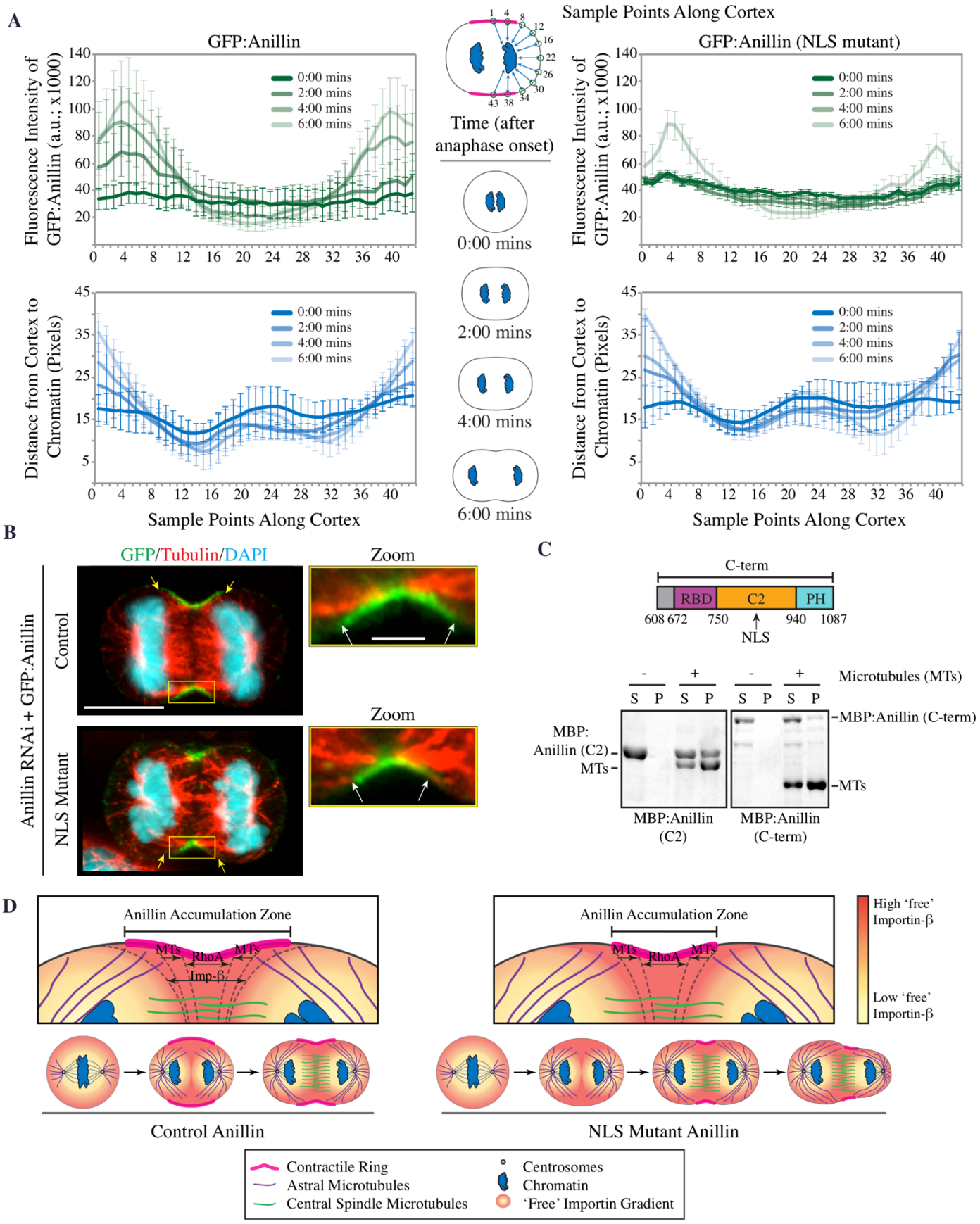
A
GFP:Anillin
GFP:Anillin (NLS mutant)
Sample Points Along Cortex
Fluorescence Intensity of GFP:Anillin (a.u.; x1000)
Distance from Cortex to Chromatin (Pixels)
0:00 mins
2:00 mins
4:00 mins
6:00 mins
Time (after anaphase onset)
Sample Points Along Cortex
B
GFP/Tubulin/DAPI
Zoom
Anillin RNAi + GFP:Anillin
Control
NLS Mutant
C
C-term
RBD
C2
PH
608 672
750
940
1087
NLS
Microtubules (MTs)
S P S P S P S P
MBP:Anillin (C-term)
MBP: Anillin (C2)
MTs
MBP:Anillin (C2)
MBP:Anillin (C-term)
D
Anillin Accumulation Zone
MTs
RhoA
Imp-β
High 'free' Importin-β
Low 'free' Importin-β
Control Anillin
NLS Mutant Anillin
Contractile Ring
Astral Microtubules
Central Spindle Microtubules
Centrosomes
Chromatin
'Free' Importin Gradient

Figure 8. The C-terminal NLS influences anillin's affinity for the equatorial cortex during cytokinesis

A) A macro written for ImageJ measured average anillin intensity at 43 points around the cortex as well as the distance from each point to chromatin. Line graphs show anillin intensity (top graphs; green), and distance to chromatin (bottom graphs; blue) as indicated in the schematic at the top, from anaphase onset to early ingression. The graphs on the left show measurements from anillin-depleted cells rescued with GFP-tagged RNAi resistant anillin (n=5 cells), and the graphs on the right show anillin-depleted cells rescued with GFP-tagged RNAi resistant NLS mutant anillin (n=5 cells). Bars show SD. **B**) Images show HeLa cells treated with anillin RNAi expressing GFP-tagged RNAi-resistant anillin or NLS mutant anillin, co-stained for GFP (green), tubulin (red) and DAPI (chromatin; cyan). Yellow arrows point to astral microtubules. The scale bar is 10 μm. Zoomed-in regions in the boxed insets show anillin and microtubules at the furrow, as indicated. White arrows point to the demarcation of anillin localization. The scale bar is 2 μm. **C**) Cartoon schematic shows binding domains in the C-terminus of anillin (RBD, C2, PH). Below are Coomassie-stained gels of co-sedimentation assays (S, supernatants; P, pellets) using 1.5 μM purified microtubules (MT) incubated with 1.5 μM purified MBP-tagged anillin proteins as indicated. A comparison between C2 and C-term is shown. **D**) Cartoon schematics show anillin vs. NLS mutant anillin (right) localization during anaphase and early telophase. Zoomed-in regions highlight how the zone of anillin is determined by RhoA-GTP and importin-β, the latter of which permits the spread of anillin beyond the boundary of astral microtubules. The levels of free importin-β are determined by the Ran-GTP gradient formed around chromatin.

2.4.4 Importin binding influences anillin's affinity for the equatorial cortex

Our analyses of NLS mutant anillin suggest that disrupting importin binding weakens anillin's affinity for the equatorial cortex. Typically, the boundary of equatorial anillin tightly matches active RhoA, and will loosely correlate with mitotic spindle position (yellow arrows; **Figure 8B**; Piekny and Glotzer, 2008; van Oostende Triplet et al., 2014). The decrease in breadth of mutant anillin's localization is similar to what we observed when the proportion of astral microtubules was increased near the equatorial plane via MCAK RNAi (Zanin et al., 2013; van Oostende Triplet et al., 2014). Indeed, the localization of NLS mutant anillin tightly matched the boundary of microtubules near the equatorial cortex (white arrows), while nonmutant anillin loosely correlated with their position as shown previously (**Figure 8B**; van Oostende Triplet et al., 2014). We previously reported that the C-terminus of anillin weakly bound to microtubules *in vitro* (Tse et al., 2011; van Oostende Triplet et al., 2014). Because importin-β binding to the C2 domain is inhibited by the RBD, we compared microtubule binding to the C-terminus and the C2 domain using co-sedimentation assays. Microtubules bound more strongly to the C2 domain than to the C-terminus (**Figure 8C**). In addition, a deletion that removes the NLS and a small region upstream (DFEINIE) that lies at the hinge of the RBD and C2 also bound to microtubules more strongly (unpublished data; Piekny and Glotzer, 2008). Therefore, the microtubule-binding domain is autoinhibited by the RBD, similar to the NLS. We did not observe a significant change in microtubule binding with the C2 NLS mutant (**Figure S4B**). Thus, the change in NLS mutant anillin localization in cells suggests that there is a reduction in its affinity for the equatorial cortex.

To further show that the localization of NLS mutant anillin at the equatorial plane is strongly regulated by microtubules, we monitored changes in its localization after depolymerizing astral microtubules using a low dose of nocodazole (33 nM). The localization of nonmutant and

mutant anillin broadened along the equatorial cortex to a similar extent, supporting the conclusion that microtubules were responsible for restricting mutant anillin localization (**Figures 7A, B**). We previously reported that both the central spindle and astral microtubules contribute to restricting anillin localization, and this is why we do not see anillin expanding into the polar regions of the cell (van Oostende Triplet et al., 2014).

2.5 Discussion

Our studies shed light on a microtubule-independent mechanism that ensures robust cytokinesis. Previous studies showed that HeLa cells lacking polymerized microtubules polarize, and the contractile protein anillin localizes away from chromatin (Kiyomitsu and Cheeseman, 2013). Ran-GTP is required for this polarization, because anillin fails to move away from chromatin after reducing the activity of its GEF, RCC1, or reducing Ran-GTP-importin binding using the drug Importazole (**Figure S2B**; Kiyomitsu and Cheeseman, 2013). Thus, a Ran-GTP gradient associated with chromatin may lead to relaxation of the polar cortex when the mitotic spindle shifts too close to one pole to restore the cleavage plane (Kiyomitsu and Cheeseman, 2013). Our studies add to this model by showing that anillin is a molecular target of the Ran pathway during cytokinesis. Anillin is a key regulator of cytokinesis that binds to multiple contractile ring components including RhoA, and we have shown that anillin can feed back to influence active RhoA in vivo (Piekny and Glotzer, 2008; Frenette et al., 2012). We propose that the Ran pathway modulates cytokinesis by affecting anillin's recruitment to the cortex. During mitotic exit, RhoA-GTP levels increase and bind to the RBD of anillin, causing a change in its conformation that makes other binding sites in the C-terminus more accessible, including the NLS and microtubule-binding domain. Importin binding may stabilize this open conformation to further enhance anillin's

recruitment to the cortex. However, in the vicinity of chromatin, high Ran-GTP would bind to importin(s) and prevent them from binding to, or promoting its release from cargo such as anillin, which would favor anillin's cytosolic localization. Free importins (*e.g.* not bound to Ran-GTP, but possibly bound to cargo) form an inverse gradient to Ran-GTP, with optimal levels likely occurring near the cortex, where importin-β could bind to anillin and favor its cortical recruitment (**Figure 8D**).

We have several pieces of evidence to support our model. First, we show that Ran-GTP levels influence the localization of contractile proteins and cause cytokinesis phenotypes. Reducing the levels of Ran-GTP led to the ectopic recruitment of anillin and myosin to regions of the cortex where they normally would not accumulate, likely causing a change in cortical properties at the cell poles and blocking furrow ingression (**Figure 3**). Consistent with a function for Ran-GTP in negatively regulating anillin, increasing the levels of active Ran in the equatorial furrow caused a reduction in anillin and cortical instability phenotypes similar to anillin loss-of-function (**Figure 4**). There are two ways that Ran-GTP could do this: 1) by directly binding to and competing importins from cargo/target proteins that promote or prevent a specific function, or 2) by regulating nuclear sequestration of cytokinesis regulators. Upshifting tsBN2 cells to inactivate RCC1 (the GEF for Ran) likely keeps the nuclear envelope from reforming causing cells to remain in a persistent cytokinesis-like state (**Figure 3**; Clarke and Zhang, 2008). This may occur because regulators of actomyosin contractility that are normally nuclear in telophase (*e.g.* Ect2) have continued access to the cortex when the nuclear envelope fails to form. However, our experiment targeting active Ran directly to the membrane provides evidence that Ran-GTP directly influences the cortex (**Figure 4**). Second, we found that anillin contains a highly conserved NLS in its C-terminus that binds to importin-β and is required for anillin's localization, cortical polarization and

cytokinesis (**Figures 5-8**). This site can function in response to the Ran pathway to mediate nuclear entry, but is autoinhibited by the RBD (**Figure 6**). The RBD also blocks accessibility to anillin's microtubule-binding site (**Figure 8**). This autoinhibition could ensure that anillin's C-terminus has access to importin or microtubules only when RhoA-GTP levels increase during mitotic exit. A recent study showed that anillin is also regulated by phosphorylation, via a site that lies just N-terminal to the RBD (Kim et al., 2017). An extension of our model is that phosphorylation may further influence RhoA-GTP binding, to couple the timing of changes in anillin's activity with its requirement for cytokinesis. We found that the C-terminal NLS is required for anillin's localization, because the equatorial domain of anillin is more restricted when the NLS is mutated (**Figures 7** and **8D**). This is similar to what we observed when astral microtubules were enriched in the equatorial plane via MCAK RNAi (van Oostende Triplet et al., 2014), suggesting a decrease in anillin's affinity for the equatorial cortex and a shift toward microtubules in spatially controlling anillin. Indeed, the localization of NLS mutant anillin changes/broadens after astral microtubule perturbation (**Figure 7**).

Our study reconciled two models that had been proposed to explain how Ran-GTP could influence the cortex (Silverman-Gavrila et al., 2008; Kiyomitsu and Cheeseman, 2013). One study showed that importin-α competes for septin binding in the C-terminus of anillin and could release anillin for septin binding in the vicinity of chromatin during cellularization (Silverman-Gavrila et al., 2008). A different study showed that Ran-GTP inhibited rather than promoted anillin's cortical localization during mitotic exit (Kiyomitsu and Cheeseman, 2013). Our data supports the latter model, as described above. However, we also found that overexpression of importin-β decreased the breadth of anillin's localization in the equatorial plane, similar to the NLS mutant, which cannot bind to importin-β. Thus, we propose a hybrid model where importin binding facilitates

anillin's cortical recruitment, but likely binds with low affinity to ensure that anillin can favorably bind to other proteins and lipids. Thus, importins could function as a molecular ruler, whose optimal levels favor the localization of cortical proteins at precise locations as opposed to when they are too high or too low.

A recent study identified a putative phospholipid-binding site in the C2 domain of anillin, which may partially overlap with the C-terminal NLS that we describe here (Sun et al., 2015). It found that this site functions cooperatively with the RBD to recruit anillin to the cortex (Sun et al., 2015). Our data fit with this previous finding, and importin binding could also influence phospholipid binding, leading to the enhancement of anillin's recruitment to the cortex. It is important to note that the NLS mutations used in this study are not in the predicted phospholipid-binding domain described in Sun et al., (2015). Further, although delayed, all of the anillin constructs containing mutations in the NLS localized to the cortex, likely due to their recruitment via other proteins and/or lipids.

The Ran pathway likely regulates the cortex during anaphase. During metaphase, Ran-GTP forms a gradient around chromatin where it regulates bipolar spindle formation (Kaláb et al., 2002; Kaláb et al., 2006; Clarke and Zhang, 2008). We propose that Ran-GTP also regulates cortical proteins during mitotic exit. We observed a strong correlation in the timing and spatial distribution of anillin's cortical localization with the distance of the segregating sister chromatids (**Figure 8**). This correlation was no longer apparent when the NLS was mutated, which was only recruited to a narrow region of the furrow ~ 6 min after anaphase onset, likely via the central spindle (**Figure 8**). The regulation of protein-protein interactions via importins is not a new concept, but our model expands on the understanding of how importins could regulate the conformation and function of cortical proteins. While our studies were performed in HeLa cells, which divide symmetrically, it

would be interesting to determine if the Ran-anillin pathway more dominantly regulates cytokinesis in asymmetrically dividing cells. Furthermore, this pathway may improve the robustness of cytokinesis in cancer cells with high chromosomal instability and altered ploidy, particularly because cancer cells with polyploidy have steeper Ran-GTP gradients (Hasegawa et al., 2013).

Chapter 3: Importin-binding mediates the intramolecular regulation of anillin during cytokinesis

Adapted from: Beaudet D., Pham N., Skaik N., and Piekny A. (2019). Intramolecular regulation of anillin during cytokinesis. *BioRxiv*. doi:10.1101/726471

3.1 Abstract

Cytokinesis occurs by the ingression of an actomyosin ring that cleaves a cell into two daughters. This process is tightly controlled to avoid aneuploidy, and we previously showed that active Ran coordinates ring positioning with chromatin. Active Ran is high around chromatin, and forms an inverse gradient to cargo-bound importins. We found that the ring component anillin contains an NLS that binds to importin and is required for its function during cytokinesis. Here we reveal the mechanism whereby importin-binding favors a conformation required for anillin's recruitment to the equatorial cortex. Active RhoA binds to the RhoA-binding domain (RBD) causing an increase in accessibility of the nearby C2 domain containing the NLS. Importin-binding then feeds back to the RBD for cortical recruitment. In addition to revealing a novel mechanism for the importin-mediated regulation of a cortical protein, we also show how importin-binding positively regulates protein function.

3.2 Introduction

Cytokinesis occurs at the end of mitosis to physically separate a cell into two daughters. This process must be strictly controlled to ensure that each daughter inherits the appropriate genetic material and cell fate determinants. Cytokinesis occurs due to the ingression of an actomyosin ring (Green et al., 2012). Contractile proteins localize broadly around the cortex in

early anaphase and are restricted to the equatorial zone prior to furrow ingression. Ring assembly and ingression is regulated by active RhoA, which binds to effectors that regulate F-actin and activate non-muscle myosin II (Piekny et al., 2005; Basant and Glotzer, 2018). Active RhoA also recruits the scaffold protein anillin, which crosslinks the actomyosin ring to the plasma membrane and feeds back to stabilize active RhoA for robust cytokinesis (Piekny and Glotzer, 2008; van Oostende Triplet et al., 2014; Sun et al., 2015; Budnar et al., 2019). Since anillin crosslinks key components of the cell during cytokinesis, understanding its molecular regulation can provide insight to how cytokinesis is regulated. In particular, the C-terminus of anillin contains a RhoA-GTP binding domain (RBD), a neighboring C2 domain, and a Pleckstrin Homology (PH) domain, which coordinate its localization through 1) binding to active RhoA, 2) binding to phospholipids, importins and/or microtubules via the C2 domain, and 3) binding to phospholipids and/or septins via the PH domain (Oegema et al., 2000; Piekny and Glotzer, 2008; Piekny and Maddox, 2010; Liu et al., 2012; van Oostende Triplet et al., 2014; Sun et al., 2015; Beaudet et al., 2017). However, which of these interactions is crucial for anillin function and how they are coordinated is not clear.

Multiple mechanisms regulate cytokinesis and are derived from spindle-dependent (*e.g.* Dechant and Glotzer, 2003; Somers and Saint, 2003; Bement et al., 2005; Bringmann and Hyman, 2005; Yüce et al., 2005; Zhao and Fang, 2005; Werner et al., 2007; Lewellyn et al., 2010; van Oostende Triplet et al., 2014; Pollard and O'Shaughnessy, 2019) and -independent pathways (*e.g.* von Dassow et al., 2009; Cabernard et al., 2010; Schenk et al., 2010; Sedzinski et al., 2011; Kiyomitsu and Cheeseman, 2013; Zanin et al., 2013; Rodrigues et al., 2015; Beaudet et al., 2017). The central spindle forms between segregating chromosomes during anaphase and contains anti-parallel bundled microtubules. Centralspindlin, a heterotetramer of Cyk-4 and MKLP1, bundles central spindle microtubules and forms a complex with the RhoA GEF, Ect2, which stimulates the

activation of RhoA in the equatorial cortex (Mishima et al., 2002; Mishima et al., 2004; Bement et al., 2005; Yüce et al., 2005; Petronczki et al., 2007; Burkard et al., 2009; Wolfe et al., 2009). Several studies showed that the membrane-localization of this complex is crucial for Ect2's GEF activity vs. spindle localization and the role of microtubules remains to be clarified (Frenette et al., 2012; Lakomtsev et al., 2012; Basant et al., 2015; Kotýnková et al., 2016). Astral microtubules emanate toward the poles and inhibit contractility at the nearby cortex. Cells treated with nocodazole to depolymerize microtubules cause a global increase in active RhoA and an increase in the breadth of accumulated contractile proteins (Chang et al., 2008; Murthy and Wadsworth, 2008; Zanin et al., 2013; van Oostende Triplet et al., 2014). Increasing the density of astral microtubules by depleting MCAK (a microtubule depolymerase) decreases the zone of accumulated contractile proteins, which is restored upon co-depletion of anillin (Rankin and Wordeman, 2010; Zanin et al., 2013; van Oostende Triplet et al., 2014). Anillin directly binds to microtubules, and its localization to microtubules in cells is enhanced by increased microtubule stability or density, and decreased by active RhoA (Tse et al., 2011; van Oostende Triplet et al., 2014). Thus, astral microtubules may sequester anillin at the cell poles, but not at the furrow to prevent contractility at the polar cortex (Tse et al., 2011; van Oostende Triplet et al., 2014). A recent study showed that in the early *C. elegans* embryo, the clearing of F-actin and anillin at the polar cortex depends on the astral microtubule-based TPXL-1-mediated activation of Aurora A kinase (Mangal et al., 2018). However, it is unclear if Aurora A activity directly impacts RhoA and/or anillin localization or if there are other proteins involved since few other molecular regulators of the astral pathway are known (Bringmann et al., 2007; Basant and Glotzer, 2018).

Chromatin-sensing is one of the microtubule-independent mechanisms that regulates cytokinesis. Importins bind to the nuclear localization signals (NLS) on cargo to mediate their

nuclear transport (Soniat and Chook, 2015). Active Ran is enriched in the nucleus and competes with importins to release cargo. During mitosis, the Ran gradient persists around chromatin where it controls spindle assembly (Li and Zheng, 2004; Kaláb et al., 2006; Clarke and Zhang, 2008; Kaláb and Heald, 2008). The dogma is that importin-binding to the NLS of a spindle regulator sterically blocks interactions with partners required for their function (Weaver and Walczak, 2015). Thus, active complexes assemble the spindle near chromatin where active Ran is high. However, findings from our lab and others supports a very different function for the regulation of cortical proteins by importin-binding (Deng et al., 2007; Dehapiot et al., 2013; Dehapiot and Halet, 2013; Samwer et al., 2013; Kiyomitsu and Cheeseman, 2013; Beaudet et al., 2017). For example, importins function as a ruler during meiosis or cytokinesis, where optimal levels facilitate polarization of the nearby cortex (Deng et al., 2007; Dehapiot et al., 2013; Dehapiot and Halet, 2013; Samwer et al., 2013; Beaudet et al., 2017). This mechanism senses chromatin position to ensure that the polar body or contractile ring are properly positioned. A recent study showed that importin-α is lipid-modified by palmitoylation in *Xenopus* egg extracts, and the authors proposed this creates a cortical sink of importin-α to reduce cytoplasmic levels for scaling spindle and nuclear size (Brownlee and Heald, 2019). It will be interesting to determine if palymitoylated importin-α can form functional complexes and mediate processes at the membrane.

Previous studies in our lab provided mechanistic insight to how importins regulate anillin. We found the NLS of anillin is required for its localization and function during cytokinesis (Beaudet et al., 2017). In addition, anillin contains a RhoA-binding domain (RBD) required for cortical recruitment, and we found that the RBD autoinhibits the adjacent NLS-containing C2 domain. Our model is that binding to active RhoA facilitates a conformational change in anillin that increases accessibility to the C2 domain, and importin-binding stabilizes this conformation

for optimal recruitment to the equatorial cortex. Here, we present data supporting this model. We found that active RhoA facilitates importin-binding, while inactive RhoA or mutating the RBD decreases importin-binding. Through live-imaging and FRAP experiments we found that mutating the NLS alters anillin's cortical properties. Anillin's localization and function are abolished when NLS mutations are combined with mutations that weaken the interface between the RBD and C2 domain. When stronger interface mutations are introduced into anillin, it similarly fails to localize to the furrow and fails to undergo cytokinesis. This data shows that the interface is crucial to drive feedback between the C2 domain and the RBD for cortical recruitment.

3.3 Materials and methods

3.3.1 Cell culture

HeLa cells were plated and grown in Dulbecco's Modified Eagle Medium (DMEM; Wisent), supplemented with 10% fetal bovine serum (FBS; Thermo Scientific), 2 mM L-glutamine (Wisent), 100 U penicillin and 0.1 mg/mL streptomycin (Wisent) and were maintained at 37°C with 5% CO_2. For transfection, cells were plated in DMEM media without antibiotics (PS), and transfected using Lipofectamine 2000 according to the manufacturer's protocol (Invitrogen), except that 3 μL of Lipofectamine was used per 2 mL of media with 0.5–2.0 μg DNA and 3 μL of 2 nM siRNAs, as described previously (Yüce et al., 2005; Piekny and Glotzer, 2008). Cells were imaged 24–26 hours after DNA transfection, and 27–30 hours after co-transfection of DNA and siRNAs. Anillin, Ect2 and MCAK siRNAs were used as described previously (Yüce et al., 2005; Piekny and Glotzer, 2008; van Oostende Triplet et al., 2014).

3.3.2 Plasmids

H2B:mRuby was generated from H2B:GFP, generously provided by G. Hickson (University of Montreal). GFP was replaced with mRuby using *BamHI* (New England Biolabs) and *XbaI* restriction enzymes (New England Biolabs), and the pcDNA3:mRuby2 plasmid was kindly provided by C. Brett (Concordia University). A stable HeLa mCherry:Tubulin cell line was generated previously (van Oostende Triplet et al., 2014). pEGFP-N1:Importin-β was obtained by Addgene, made by Patrizia Lavia (plasmid # 106941). GST:Importin-β was made by cloning Importin-β cDNA from the pEGFP-N1 vector into pGEX-4T using *NcoI* and *NotI* (New England Biolabs). The anillin constructs for mammalian cell expression (GFP-tagged) or protein expression (MBP or GST-tagged) were generated previously (Piekny and Glotzer, 2008; Frenette et al., 2012). The 850 KK 851-DE (NLS mutant), A703E; E721A (RBD mutant; Sun et al., 2015), 837 DFEINIE 843-AFAINIA (*weak* I/F mutant; Piekny and Glotzer, 2008), 735 LL 736-DD (*strong* I/F mutant) and combinations of mutations were generated in the anillin constructs by quickchange PCR. The His:RhoA and Myc:Ect2 (C-terminus) constructs were generated previously (Yüce et al., 2005; Frenette et al., 2012). All constructs were verified by sequencing.

3.3.3 Microscopy

Cells were fixed for immunofluorescence using 10% trichloroacetic acid (TCA) as described previously (Yüce et al., 2005). Fixed cells were immunostained for microtubules using 1:200 mouse anti-tubulin antibodies (DM1A, Sigma-Aldrich), anillin using 1:200 rabbit polyclonal anti-anillin antibodies (Piekny and Glotzer, 2008), GFP using 1:100 mouse Clones 7.1 and 13.1 (Roche) or 1:200 rabbit anti-GFP polyclonal antibodies generously provided by M. Glotzer (University of Chicago). Anti-rabbit or -mouse Alexa 488 and anti-mouse or -rabbit Alexa 568 (Invitrogen) secondary antibodies were used at a 1:250 dilution. DAPI (Sigma-Aldrich) was

added at a 1:1000 dilution (1 mg/mL stock) for 5 minutes before mounting the coverslips onto slides. Fixed cells were imaged using a Leica DMI6000B wide-field microscope with the 63x/1.4 PL APO oil immersion objective (pixel size 0.102 μm), and Z-stacks of 0.5 μm were acquired with a Hamamatsu OrcaR2 camera and Volocity software (PerkinElmer) using a piezo Z stage (MadCityLabs). Image files were exported as TIFFs, which were opened with ImageJ (NIH) and converted into maximum intensity Z-stack projections. Projections and merged colour images were then converted into 8-bit images and imported into Illustrator (Adobe) to make figures.

To perform live imaging, media was replaced with phenol red-free DMEM media. Cells were plated and transfected on 25 mm round coverslips (No. 1.5) placed in a 35 mm Chamlide magnetic chamber (Quorum). Cells were kept at 37˚C with 5% CO_2 using the INU-TiZ-F1 chamber (MadCityLabs). Live imaging was performed on an inverted Nikon Eclipse Ti microscope with a Livescan Swept Field confocal unit (Nikon), using the 60x/1.4 CFI PLAN APO VC oil immersion objective (pixel size 0.27 μm), a piezo Z stage (MadCityLabs), and with the iXON897 EMCCD camera (Andor). Images were acquired with 200 ms exposures using the 488 and 561 nm lasers (100 mW, Agilent) set between 20–40% power, depending on the intensity of fluorescent signals (settings were kept constant for related experiments), and multiple Z-stacks of 0.5 μm were taken every 60 seconds per cell using NIS-Elements acquisition software (Nikon), and a narrow GFP or dual filter (500-544 and 600-665 nm; Chroma). All of the images co-expressing GFP and mRuby probes were spectrally unmixed using the NIS-Elements acquisition software (Nikon). Image files were exported as TIFFs, which were opened with ImageJ (NIH) and converted into maximum intensity Z-stack projections. Projections and merged colour images were then converted into 8-bit images and imported into Illustrator (Adobe) to make figures, or saved as AVI movie files.

3.3.4 FRAP

To perform FRAP experiments, Cells were plated and transfected on 25 mm round coverslips (No. 1.5) placed in a 35 mm Chamlide magnetic chamber (Quorum). Cells were kept at 37˚C with 5% CO_2 using the INU-TiZ-F1 chamber (MadCityLabs). Live imaging and FRAP was performed using a Nikon C2 laser scanning confocal microscope using the 100X Plan Apo I (NA1.4) objective and Elements 4.0 acquisition software (Nikon). Timelapse images were acquired at resolution of 1024x1024 pixels every 2 seconds for a total of 60 seconds. Two time points were acquired prior to photobleaching and for up to 1 minute after photobleaching. Photobleaching of control and experimental ROI's took place for a total of 5 seconds by pulsing 10 times with the laser power set between 20–50%. Movies were exported as TIFFs then opened with ImageJ (NIH) for analysis. Fluorescence intensity of bleached and non-bleached ROIs were corrected for acquisition bleaching and normalized to background. The average intensity of ROIs were plotted over time using Prism software and the signal recovery rate and maximum recovery of signal were determined using non-linear regression fitting with the following formula:

$$F(t)= y_{max}\,(1 - e^{-k_{off}t})$$

Where $F(t)$ described the fraction of fluorescence recovery for each time point after photobleaching compared to the pre-bleached signal, y_{max} described the maximum fluorescence recovery after photobleaching, and k_{off} described the dissociation rate. The half-life ($\tau_{1/2}$) or time taken to reach half the maximum fluorescence recovery after photobleaching were determined by the following equation:

$$\tau_{1/2} = ln(2)/k_{off}$$

And the immobile fraction was determined as follows:

$$F_{imm.} = 1 - y_{max}$$

Where, F_{imm} was the percent difference between the initial fluorescence signal before photobleaching and the maximum signal recovered (y_{max}) after photobleaching.

3.3.5 Protein purification, pull-downs, and PIP strips

The following proteins were made from *E. coli* BL21 cells: His:RhoA, GST, GST:Importin-β, GST:Anillin (AHD; 608-940), MBP, MBP:Anillin (C2; 750-872), MBP:Anillin (RBD + C2; 672-872), and MBP:Anillin (C-term; 608-1087), as well as containing mutations in the NLS (850 KK 851-DE), RBD (A703E; E721A), or interface (L735D; L736D). Bacteria were resuspended in lysis buffer [2.5 mM $MgCl_2$, 50 mM Tris, 150 mM NaCl pH 7.5, 0.5% Triton X-100, 1 mM dithiothreitol (DTT), 1 mM phenylmethanesulfonyl fluoride (PMSF) and 1 X protease inhibitors (Roche)], incubated with 1 mg/mL lysozyme on ice for 30 minutes, then sonicated three times. Extracts were incubated with pre-equilibrated amylose resin (New England Biolabs) or glutathione sepharose 4B (GE Lifesciences) for 5 hours or overnight at 4˚C with rotation. After washing, beads were stored as a 50% slurry at 4˚C or eluted in equivalent volumes of 100 mM maltose or 10 mM glutathione (pH 8.0) on ice for 2 hours. Protein concentration was determined by running samples by SDS-PAGE and measuring the density of bands in comparison to known concentrations of BSA and/or by Bradford assay for eluted proteins.

To test for binding, proteins were pulled down from cell lysates after transfection or using eluted recombinant purified protein. Transfected Hela cells were lysed in 50 mM Tris pH7.6, 150 mM NaCl, 5 mM $MgCl_2$, 0.5% Triton X-100, 1 mM DTT, 1 mM PMSF with 1 X protease inhibitors (Roche) and incubated with 5-10 μg of purified MBP-tagged anillin or GST-tagged importin-β protein on beads at 4°C overnight. Eluted proteins were added to beads at final

concentrations as indicated. After binding, beads were washed 3–4 X with 50 mM Tris pH 7.6, 150 mM NaCl, 5 mM $MgCl_2$ before adding SDS sample buffer to denature the proteins for SDS-PAGE. All samples were run by SDS-PAGE and wet-transferred to nitrocellulose membrane for western blotting. All blots were reversibly stained with Ponceau S to show total protein. The blots were blocked with 5% milk for 20 minutes, then incubated with either mouse anti-MBP antibodies at a dilution of 1:5000 (New England Biolabs) or 1:2500 mouse anti-GFP antibodies (Roche) in 1× PBS-T (0.140 M NaCl, 2.7 mM KCl, 10 mM Na_2HPO_4, 1.8 mM KH_2PO_4, 0.5% Triton X-100) for 1-2 hours at room temperature. After washing the membrane 3-4 X with 1 X PBS-T, secondary antibodies [anti-rabbit-HRP or anti-mouse-HRP (Cedarlane)] were added as per manufacturer's instructions in 1× PBS-T for 1 hour. The blots were developed using enhanced chemiluminescence (ECL) western blotting detection reagents (GE Amersham) and visualized on a GE Amersham Imager 600.

PIP strips (Echelon Biosciences) were blocked with 3% milk in 1× PBS-T at 4°C overnight. PIP strips were removed from blocking solution and incubated with 1 μg/mL of purified recombinant protein for 1 hour at room temperature. After washing 3–4 X with 1× PBS-T the strips were incubated with 1:5000 mouse anti-GST antibodies (Sigma). The secondary antibodies (anti-rabbit-HRP or anti-mouse-HRP) were then added in 1× PBS-T for 1 hour. After washing the membranes 3-4 X with 1 X PBS-T, the signal was developed using enhanced chemiluminescence (ECL) western blotting detection reagents (GE Amersham) and visualised on a GE Amersham Imager 600. Images were converted to 8-bit by ImageJ, and made into figures using Adobe Photoshop and Illustrator (Adobe).

3.3.6 Co-sedimentation assays

Microtubules were prepared from lyophilized microtubules (Cytoskeleton) as per manufacturer's instructions in resuspension buffer (15 mM PIPES, 1 mM $MgCl_2$, 20 μM Taxol; Bioshop) at room temperature for 10–15 minutes with gentle mixing. Aliquots of 45.5 μM were flash frozen and stored at -80˚C, then thawed in a circulating water bath and diluted with resuspension buffer to 9.1 μM. Purified anillin and importin proteins were pre-spun by centrifugation at 279,000 g for 30 minutes at room temperature. Co-sedimentation reactions were prepared in 200 µL polycarbonate tubes (Beckman Coulter) with 0.5–4 µM of microtubules and 1 µM of purified anillin, or 4 µM of microtubules, 1 µM of purified anillin and 0.2–1.5 µM of purified importin-β, 150 mM NaCl and BRB80 buffer (80 mM PIPES pH 6.8, 1 mM EGTA, 1 mM $MgCl_2$) containing 1 mM DTT and 10 µM Taxol. The reactions were kept at room temperature for 15 minutes, then centrifuged at 279,000 g for 30 minutes. The supernatants were collected, and pellets were washed and re-suspended in BRB80. Sample buffer was added to supernatants and resuspended pellets, which were then run by SDS-PAGE and stained with Coomassie Blue. Scanned gels were analyzed in ImageJ to measure the concentration of proteins using line plots to determine pixel intensities that were imported into Excel (Microsoft). After correcting for background, the average intensity was determined. The average amounts of bound anillin (Y axis) were plotted against free microtubule concentration (X axis) using GraFit version 7.0.3. The K_D and binding capacity were determined using non-linear regression (n=3 assays). For the competition assay, after correcting for background, the pixel intensity of anillin in the supernatant was divided by the pixel intensity of anillin in the pellet to obtain a ratio of anillin (S/P) for each concentration of importin-β. Anillin ratios for importin-β concentrations 0.2-1.5 µM were compared to control and data was analyzed using the Student's t test (n=3 assays).

3.3.7 Quantification

The breadth and ratio of cortical vs. cytosol accumulation for anillin were performed using ImageJ. Maximum intensity Z-projections were generated for each cell, and the breadth was determined using a line scan drawn along the cell cortex. The breadth was determined as the number of pixels above half of the maximum intensity (width of the peak) after subtracting cytosol levels, which was divided by the total number of pixels to give a ratio of breadth to length. To measure the ratio of cortical accumulation vs. cytosol, the average intensity was determined in an area drawn around the cortex from one pole to the other. This value was then divided by the average fluorescence intensity from the average of 3 ROI's in the cytosol. Similar timepoints were selected for anaphase just before ingression based on time from anaphase onset. All data was imported into Excel (Microsoft), where calculations were performed including standard deviations and student t tests, and to generate graphs. All of the images and graphs were transferred to Illustrator (Adobe) to make figures.

3.4 Results

3.4.1 The C-terminus has different cortical retention properties compared to full-length anillin

Anillin has multiple binding domains that crosslink the main components of the cytokinesis machinery (**Figure 9A**). The C-terminus contains a RhoA-binding domain (RBD) that binds to active RhoA, a C2 domain with an NLS and binding sites for phospholipids, microtubules and Ect2, and a PH domain that binds to phospholipids and septins (Piekny and Maddox, 2010; Sun et

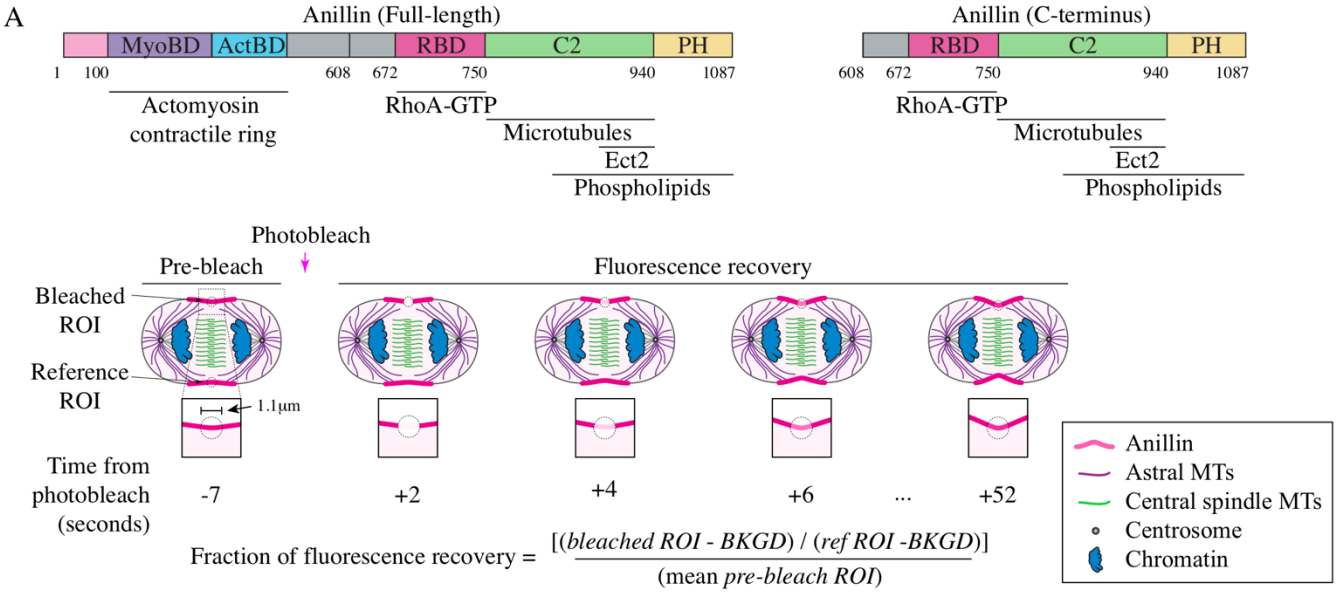

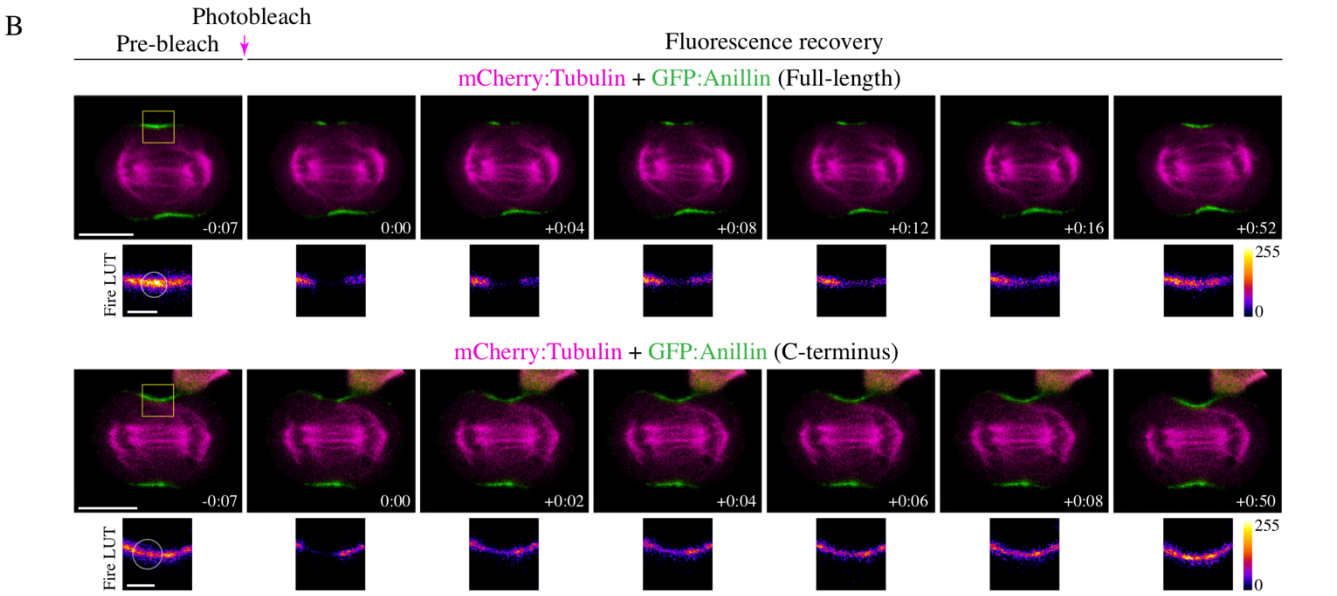

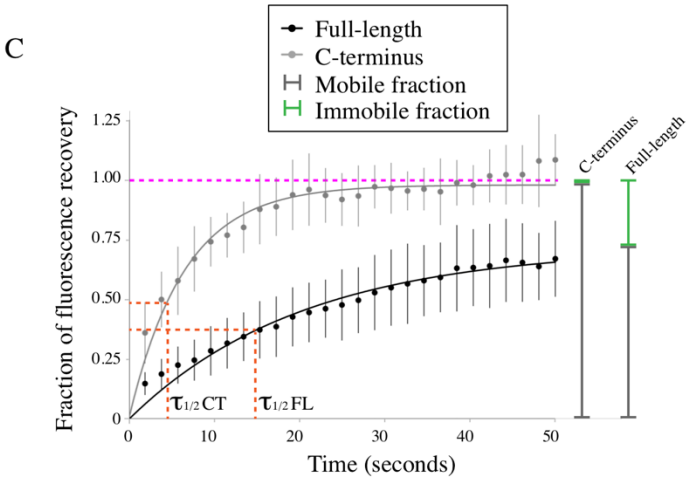

Anillin's cortical affinity parameters

	Full-length	C-terminus
y_{max}	0.7233 (0.02110)	0.9857 (0.009905)
k_{off} (s^{-1})	0.04717 (0.003119)	0.1483 (0.007237)
$\tau_{1/2}$ (s)	14.70	4.674

Figure 9. The C-terminus has different cortical properties compared to full-length anillin

A) The structures of full-length and the C-terminus of anillin are shown, with binding domains as indicated (pink = contains N-terminal NLS; purple = MyoBD, binds myosin; blue = ActBD binds actin; dark pink = RhoA-GTP binding domain (RBD), binds active RhoA; green = C2, binds microtubules, phospholipids, Ect2, and contains C-terminal NLS that binds Importin-β; yellow = Pleckstrin Homology (PH), binds phospholipids). Cartoon schematics show the fluorescence recovery after photobleaching (FRAP) of a region of interest (ROI) compared to a reference ROI in a cell expressing anillin (pink) during anaphase and early ingression. The photobleached region is shown in the boxed inset. Other components of the cell are indicated in the legend (astral microtubules in purple, central spindle microtubules in green, centrosomes in grey, and chromatin in blue). The equation used to determine the fraction of fluorescence recovery is indicated (background; BKGD). **B**) Timelapse images show FRAP of HeLa cells expressing mCherry:Tubulin (magenta) and GFP-tagged full-length (green; top panels) or the C-terminus of anillin (green; bottom panels). The boxed insets show the ROI's that were photobleached in Fire LUTs. The scale bars are 10 μm or 2 μm for boxed insets. Indicated times are before (-) or after (+) photobleaching. **C**) A graph shows the fraction of fluorescence recovery over time for full-length (n=31) and the C-terminus (n=15) of anillin. The Y-axis shows the fraction of recovery (corrected) and the X-axis shows the time in seconds. The green lines indicate the immobile fraction, while the grey lines show the mobile fraction. Bars show standard deviation (SD). The table shows the maximum recovery (y_{max}), dissociation rate (k_{off}) and half-life ($\tau_{1/2}$) of full-length and C-terminus of anillin. Standard errors are shown in parentheses (SEM).

al., 2015). Prior studies showed that anillin requires active RhoA for its recruitment to the equatorial cortex, and the C-terminus colocalizes with RhoA during cytokinesis. Thus, the C-terminus of anillin is now being used as a reporter for active RhoA (Piekny and Glotzer, 2008; Sun et al., 2015; Wagner and Glotzer, 2016). However, we do not fully understand how interactions in the C-terminus are coordinated for anillin's localization and function.

To characterize the cortical properties of anillin, we performed fluorescence recovery after photobleaching (FRAP) experiments on HeLa cells expressing GFP-tagged full-length anillin and co-expressing mCherry:Tubulin using equatorially positioned cortical regions of interest (ROI's). The % of fluorescence recovery was determined by measuring the fluorescence signal of the photobleached ROI relative to the pre-bleached ROI over 50 seconds at 2 second intervals. The bleached ROI's were corrected for background and photobleaching due to image acquisition by internally controlling each experiment with a reference ROI on the opposite side of the cortex (**Figure 9A**). First, we compared anillin's cortical retention during early vs. late ingression (**Figure S5**). The stage of ingression was determined by the ratio of the length of the ingressed cortex over the width of the cell at the equator; where $R > 0.6$ was 'early' and $R < 0.6$ was 'late' (**Figure S5A**). There were no significant differences in the dissociation rates (k_{off}) between early and late ingression, however, there was an increase in the immobile fraction during late ingression (**Figure S5B** and **S5C**). This suggests that anillin has stronger cortical retention during late cytokinesis, which may be important for the contractile ring – midbody transition.

Next, we determined how cortical properties differ between full-length anillin and the C-terminus (**Figure 9B**). As shown in the table, full-length anillin has greater cortical retention and a slower dissociation rate compared to the C-terminus (**Figure 9C**). The average k_{off} for full-length anillin was $0.047s^{-1}$ and recovered to a maximum of 72.33% of the pre-bleached intensity

compared to C-terminus, which had an average k_{off} of 0.1483s^{-1} and recovered to 98.57% of the pre-bleached intensity (**Figure 9C**). The faster dissociation rate and higher recovery suggests that the C-terminus is more mobile and has lower cortical retention compared to full-length anillin.

3.4.2 The C-terminal NLS regulates anillin's cortical affinity during cytokinesis

We previously showed that the NLS influences anillin's localization to the cortex prior to ingression, and we wanted to determine how importin-binding regulates anillin's cortical properties (Beaudet et al., 2017; **Figure 12A** and **13A**). First, we show that anillin directly binds to importin, since GST:Importin-β binds to MBP:Anillin (C2 domain) *in vitro* and mutating the NLS significantly reduces binding (**Figure 10A**). To elucidate how the loss of importin-β binding alters anillin's turnover and retention at the equatorial cortex, we performed FRAP experiments as described for Figure 1. HeLa cells co-expressing mCherry:Tubulin and GFP-tagged C-terminus of anillin containing the NLS mutations were measured during early ingression (**Figure 10B**). Mutating the NLS caused a decrease in the mobile fraction and a faster dissociation rate compared to the control. For example, the NLS mutant had an average k_{off} of 0.3230s^{-1} and recovered to 73.60% of the pre-bleached signal intensity compared to control, which had an average k_{off} of 0.1483s^{-1} and recovered to 98.57% of the pre-bleached signal intensity (**Figure 10B** and **C**). This data suggests that importin-binding improves anillin's retention by reducing dissociation, but also makes anillin more dynamic in its ability to exchange with the cortex.

Astral microtubules also regulate the localization of anillin during cytokinesis. We previously showed that overextending the astral microtubules with MCAK RNAi causes a delay in anillin's cortical recruitment and localization to a narrow region of the equatorial cortex similar

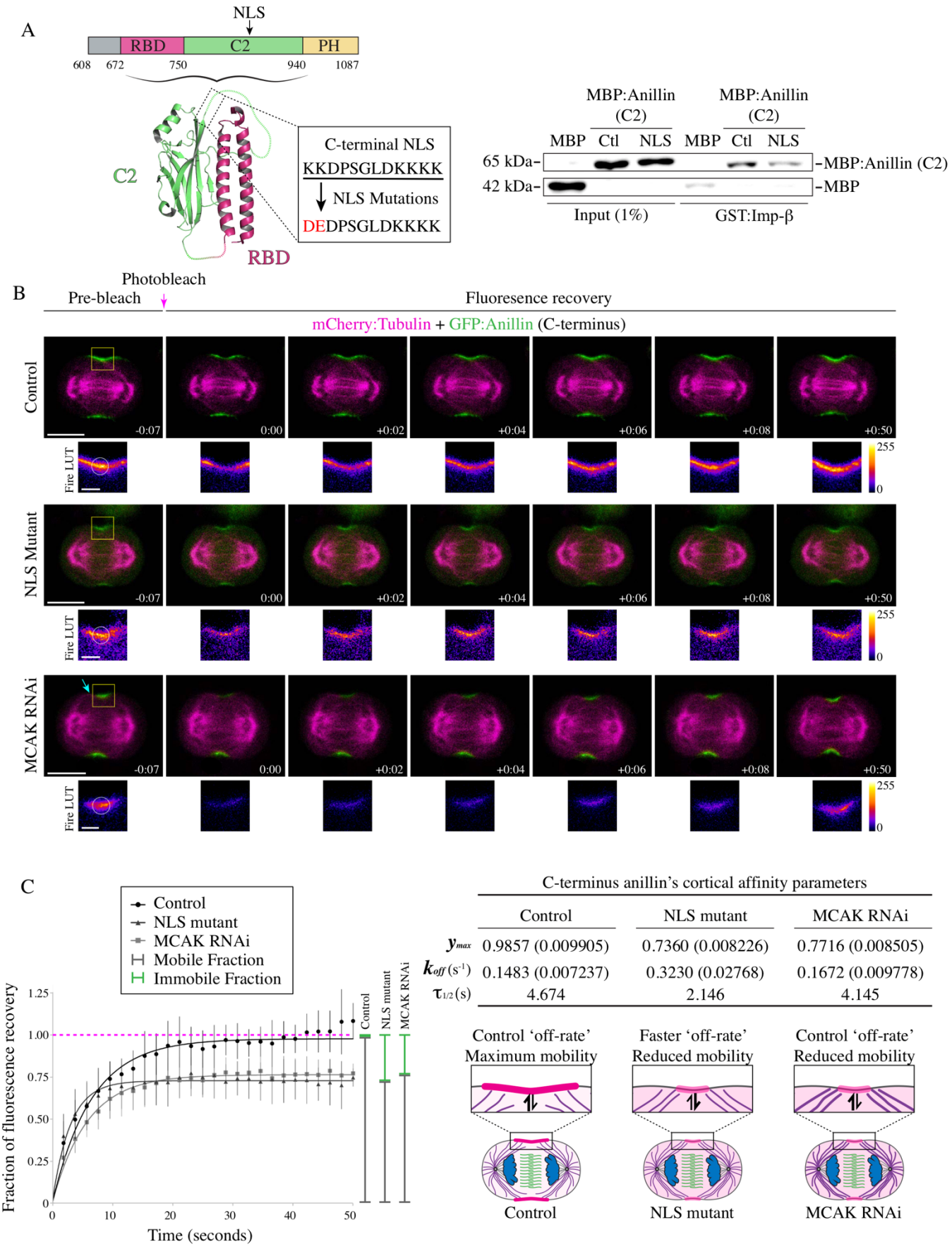
A
NLS
RBD
C2
PH
608
672
750
940
1087
C2
RBD
C-terminal NLS
KKDPSGLDKKKK
NLS Mutations
DEDPSGLDKKKK
MBP:Anillin (C2)
MBP:Anillin (C2)
MBP Ctl NLS MBP Ctl NLS
65 kDa-
42 kDa-
-MBP:Anillin (C2)
-MBP
Input (1%)
GST:Imp-β
B
Photobleach
Pre-bleach
Fluoresence recovery
mCherry:Tubulin + GFP:Anillin (C-terminus)
Control
NLS Mutant
MCAK RNAi
-0:07
0:00
+0:02
+0:04
+0:06
+0:08
+0:50
Fire LUT
255
0
C
Control
NLS mutant
MCAK RNAi
Mobile Fraction
Immobile Fraction
Fraction of fluorescence recovery
Time (seconds)
Control
NLS mutant
MCAK RNAi
C-terminus anillin's cortical affinity parameters
Control
NLS mutant
MCAK RNAi
y_{max} 0.9857 (0.009905) 0.7360 (0.008226) 0.7716 (0.008505)
k_{off} (s^{-1}) 0.1483 (0.007237) 0.3230 (0.02768) 0.1672 (0.009778)
$\tau_{1/2}$ (s) 4.674 2.146 4.145
Control 'off-rate'
Maximum mobility
Faster 'off-rate'
Reduced mobility
Control 'off-rate'
Reduced mobility
Control
NLS mutant
MCAK RNAi

Figure 10. The C-terminal NLS regulates anillin's cortical affinity during cytokinesis

A) A cartoon schematic shows the C-terminus of anillin, with binding domains and the NLS as indicated (dark pink = RBD; green = C2; yellow = PH). Underneath is a ribbon structure of the RBD (pink) and C2 domain (green). The amino acids of the NLS and those that were mutated (850 KK 851 – DE) are shown in the box. On the right, immunoblots show the *in vitro* binding of GST-tagged Importin-β (Imp-β) with MBP-tagged C2 domain (Ctl) vs. the C2 domain with the NLS mutations (NLS). Inputs are shown on the left, and pull-downs on the right. **B**) Timelapse images show FRAP of HeLa cells expressing mCherry:Tubulin (magenta) and GFP-tagged C-terminus of anillin (green), or with the NLS mutations, or after treatment with MCAK RNAi. The boxed insets show the ROI's that were photobleached in Fire LUTs. The scale bars are 10 μm or 2 μm for boxed insets. The blue arrow points to overextended microtubules. Indicated times are before (-) or after (+) photobleaching. **C**) A graph shows the fraction of fluorescence recovery (Y-axis) over time (X-axis; seconds) for control (n=15), NLS mutant anillin (n=12), or after MCAK RNAi (n=8). The green lines indicate the immobile fraction, while the grey lines show the mobile fraction. Bars show SD. The table shows the maximum recovery (y_{max}), dissociation rate (k_{off}) and half-life ($\tau_{1/2}$) for each condition as indicated. SEM are shown in parentheses. Below the table, cartoon schematics of cells show how mutating the NLS causes a faster off-rate vs. MCAK RNAi, which has an off-rate that is similar to control. However, both the NLS mutant and MCAK RNAi have reduced mobility.

to the NLS mutant (**Figure 10B**; van Oostende Triplet et al., 2014). We also found that disrupting the astral microtubules caused NLS mutant anillin to spread along the equatorial cortex (Beaudet et al., 2017). Next, we determined how microtubules influence anillin's cortical turnover and retention. FRAP experiments were performed using HeLa cells treated with MCAK RNAi, co-expressing mCherry:Tubulin and GFP-tagged C-terminus of anillin as described for Figure 9 and 10A (**Figure 10B** and **C**). MCAK-depleted cells had an average k_{off} of $0.1672s^{-1}$ and the fluorescence signal recovered to 77.16% of the pre-bleached signal. Thus, astral microtubules decrease the mobility of cortical anillin, but have no impact on its dissociation. This suggests that the NLS mutant alters a cortical property of anillin independent of microtubules.

We previously found that the microtubule-binding region of anillin maps to the C2 domain, but the precise binding site was not determined (van Oostende Triplet et al., 2014; Beaudet et al., 2017). We wanted to determine if the importin and microtubule binding regions overlap, and if their binding is competitive. First, we performed co-sedimentation assays to test how mutating the NLS changes anillin's affinity for microtubules. This was done using 1 μM of recombinant MBP-tagged C2 domain of control or NLS mutant anillin with varying concentrations of polymerized Taxol-stabilized microtubules (0.5 – 4 μM) and quantifying the amount of protein in the pellets vs. supernatants on a Coomassie-stained gel (**Figure S6A**). Anillin's affinity for microtubules was quantified by comparing bound (pellet) vs. unbound (supernatant) protein, and was found to be 0.089 μM for control anillin compared to 0.96 μM for NLS mutant anillin (**Figure S6A**). This ~10-fold decrease in affinity suggests that the NLS is partially required for microtubule binding. Next, we determined if importin competes with microtubules for anillin-binding. To test this, we performed co-sedimentation assays using a fixed 1:2.5 μM ratio of anillin (MBP:Anillin C2) and microtubules, and titrated in varying concentrations of recombinant GST:Importin-β (0.2 – 1.5

μM; **Figure S6B**). Increasing the concentration of importin-β reduced, but did not eliminate anillin-binding to microtubules (**Figure S6B**). This data suggests that importin and microtubules partially compete for anillin binding at a site that includes the NLS. Thus, when the NLS is mutated, cytokinesis phenotypes could be caused by a reduction in importin- and/or microtubule-binding. However, we previously showed that depolymerizing microtubules using a low dose of nocodazole increases anillin's cortical enrichment, suggesting that reducing anillin's affinity for microtubules would increase anillin's retention or mobility. Since the phenotypes caused by the NLS mutant are the opposite, they more likely arise due to loss of importin-binding and a decrease in cortical affinity.

Previous studies showed that the C2 domain can bind to $PI4,5P_2$ phospholipids (Sun et al., 2015; Budnar et al., 2019). Although the NLS mutations are outside of the putative lipid-binding site, we wanted to be sure that they did not impact lipid-binding. We compared the binding profiles of recombinant control GST:Anillin RBD + C2 with the NLS mutant using strips blotted with a variety of phospholipids including mono, di and tri-phosphorylated (3,4,5) lipids and found no change in their profiles (**Figure S6C**). Interestingly, there was a strong lipid preference for PI3P. We previously showed that GFP:Anillin C-terminus bound preferentially to $PI4,5P_2$ lipids, suggesting that either the PH domain, and/or complexes formed in cells influence anillin's lipid preference (Frenette et al., 2012).

3.4.3 The NLS is auto-inhibited by the RBD and is relieved via RhoA binding

Our previous study showed that the NLS in the C2 domain is intramolecularly inhibited by the RBD, since removing the RBD increases anillin's affinity for importin-β from cell lysates (Beaudet et al., 2017). This inhibition is direct because MBP:Anillin C2 binds more strongly to

GST:Importin-β *in vitro* compared to MBP:Anillin C-terminus (**Figure 11A**). To determine if active RhoA relieves intramolecular inhibition from the RBD, pull-down assays were performed using lysates from cells where RhoA activity was manipulated. Lysates collected from cells expressing GFP:Anillin (C-terminus) were loaded with 5 mM of GDP or GTP to generate higher levels of GTPases bound to GDP or GTP as described previously (Piekny and Glotzer, 2008; **Figure 11B**). GST:Importin-β pulled down more anillin from lysate loaded with GTP compared to lysate loaded with GDP. Since this assay was not selective for RhoA, we determined how altering RhoA activity impacts importin-binding to anillin. MBP:Anillin (RBD + C2) was used to pull-down GFP-tagged Importin-β from lysates where the C-terminus of Ect2, which has unregulated GEF activity toward RhoA, was overexpressed in cells (Solski et al., 2004; Frenette et al., 2012), or where Ect2 RNAi was used to deplete endogenous Ect2 to reduce active RhoA (**Figure 11C**). We found that importin-β was more strongly pulled down with increased levels of active RhoA compared to lysates with reduced levels of active RhoA. We also determined how introducing mutations into the RBD that disrupt RhoA-binding (A703E, E721A; Sun et al., 2015) affect anillin's affinity for importin. When MBP:Anillin (RBD + C2) containing these RBD mutations were used to pull-down GFP-tagged Importin-β from lysates, importin-binding was drastically reduced compared to control (**Figure 11D**) regardless of Ect2 levels or activity. This data suggests that importin-binding to anillin is regulated by active RhoA, and our model is that RhoA-binding causes a conformational change that exposes the NLS in the C2 domain (**Figure 11E**).

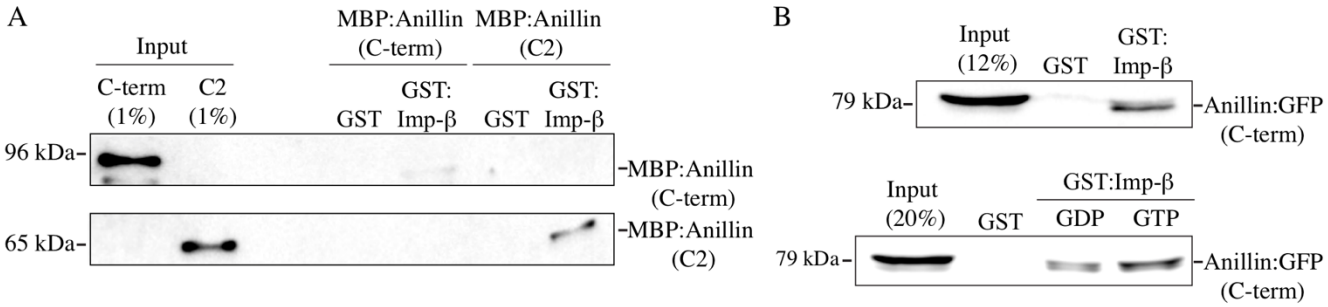
A
Input
MBP:Anillin (C-term)
MBP:Anillin (C2)
C-term (1%)
C2 (1%)
GST
GST: Imp-β
GST
GST: Imp-β
96 kDa
MBP:Anillin (C-term)
65 kDa
MBP:Anillin (C2)
B
Input (12%)
GST
GST: Imp-β
79 kDa
Anillin:GFP (C-term)
Input (20%)
GST
GST:Imp-β
GDP
GTP
79 kDa
Anillin:GFP (C-term)

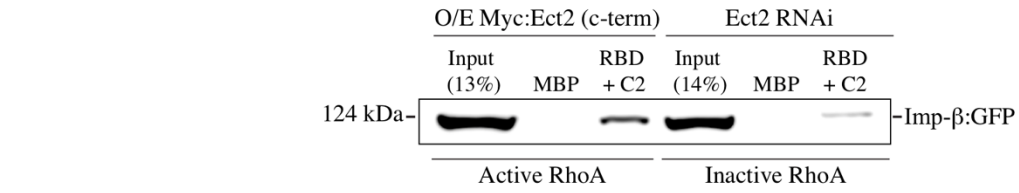
C
O/E Myc:Ect2 (c-term)
Ect2 RNAi
Input (13%)
MBP
RBD + C2
Input (14%)
MBP
RBD + C2
124 kDa
Imp-β:GFP
Active RhoA
Inactive RhoA

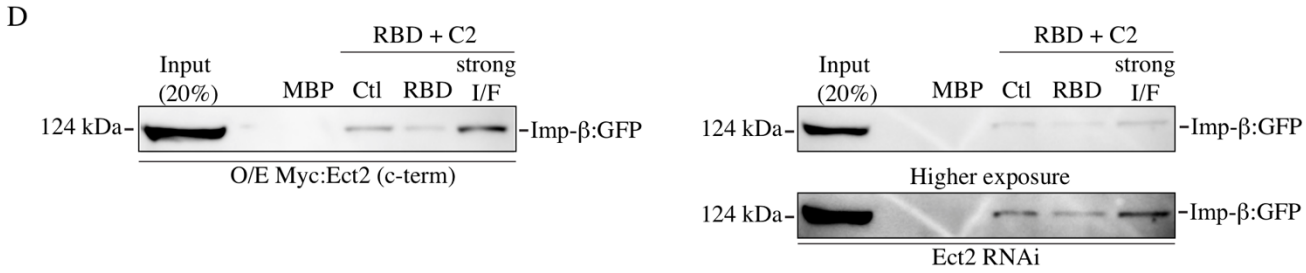
D
RBD + C2
Input (20%)
MBP
Ctl
RBD
strong I/F
124 kDa
Imp-β:GFP
O/E Myc:Ect2 (c-term)
RBD + C2
Input (20%)
MBP
Ctl
RBD
strong I/F
124 kDa
Imp-β:GFP
Higher exposure
124 kDa
Imp-β:GFP
Ect2 RNAi

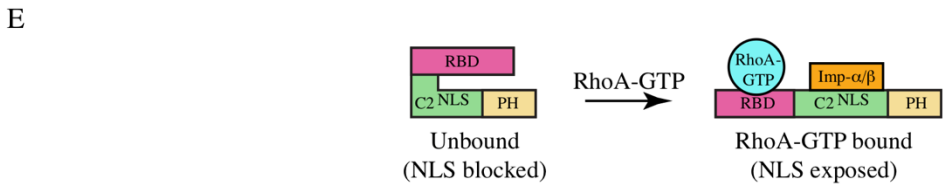
E
RBD
C2
NLS
PH
Unbound (NLS blocked)
RhoA-GTP
RhoA-GTP
Imp-α/β
RBD
C2
NLS
PH
RhoA-GTP bound (NLS exposed)

Figure 11. The NLS is inhibited by the RBD and is relieved via RhoA binding

A) Immunoblots show *in vitro* binding of purified GST or GST-tagged importin-β (Imp-β) with MBP-tagged C-terminus of anillin (C-term; top) or the C2 domain (bottom). **B**) Immunoblots show pull-downs of GFP-tagged C-terminus of anillin (C-term) from HeLa cell lysates with purified GST or GST-tagged importin-β (top). Cell lysates were preloaded with 5 mM GDP or 5 mM GTP as indicated (bottom). **C**) An immunoblot shows pull-downs of GFP-tagged importin-β from lysates from cells overexpressing (O/E) Myc-tagged Ect2 C-terminus to generate active RhoA (left), or after Ect2 RNAi to reduce active RhoA (right), with purified MBP or MBP-tagged anillin (RBD + C2). **D**) Immunoblots show pull-downs of GFP-tagged importin-β from lysates as in C) with MBP, MBP-tagged anillin (RBD + C2; Ctl) or with RBD mutations (RBD), or mutations that strongly disrupt the RBD-C2 interface (strong I/F). **E**) A cartoon schematic shows how RhoA-GTP (blue) binding to the RBD (pink) could relieve inhibition of the C2 domain (green; NLS is indicated) to enable importin-α/β (orange) binding to the NLS (PH domain is in yellow).

3.4.4 Importin-binding enhances anillin's affinity for the cortex

Mutating the NLS reduces anillin's cortical affinity, implying that this mutant could impact anillin's recruitment by active RhoA. We wanted to determine how the RBD and C2 domains are coordinated to drive anillin's localization and function for cytokinesis. To test this, we performed localization studies in HeLa cells co-expressing H2B:mRuby to visualize chromatin and GFP-tagged C-terminal control or mutant anillin constructs. Prior studies showed that decreasing active RhoA or mutating the RBD (A703E, E721A) prevents anillin's accumulation at the equatorial cortex (Piekny and Glotzer, 2008; Sun et al., 2015). We determined how mildly disrupting the interface (I/F) between the RBD and C2 domain (843-DFEINIE to AFAINIA; Piekny and Glotzer, 2008), mutating the NLS (NLS mutant; Beaudet et al., 2017) or combining the I/F and NLS mutations affects anillin localization compared to the RBD mutant (**Figure 12A**). At anaphase onset, the C-terminus of anillin was broadly cortically localized, followed by its restriction to the equatorial cortex prior to ingression (**Figure 12A** and **B**). As expected, anillin failed to localize to the cortex when the RBD was mutated (**Figure 12A** and **B**). Mutating the I/F or NLS reduced the breadth of anillin's cortical localization, causing it to be restricted to a narrow region compared to control anillin (**Figure 12A** and **B**). Interestingly, anillin failed to localize to the cortex altogether when the NLS and I/F mutations were combined, similar to the RBD mutant (**Figure 12A** and **B**). We quantified the changes in localization for the different mutants in two ways. First, we measured the breadth of anillin by drawing a line scan around the perimeter of the cell, then added the number of pixels above 50% maximum levels and determined their ratio vs. the total number of the perimeter. The ratio of anillin containing the NLS or I/F mutations was significantly lower compared to control anillin (**Figure 12B**). Next, we measured the ratio of cortical vs. cytosolic anillin, and found that while the I/F mutant was moderately enriched in the cytosol, the I/F + NLS

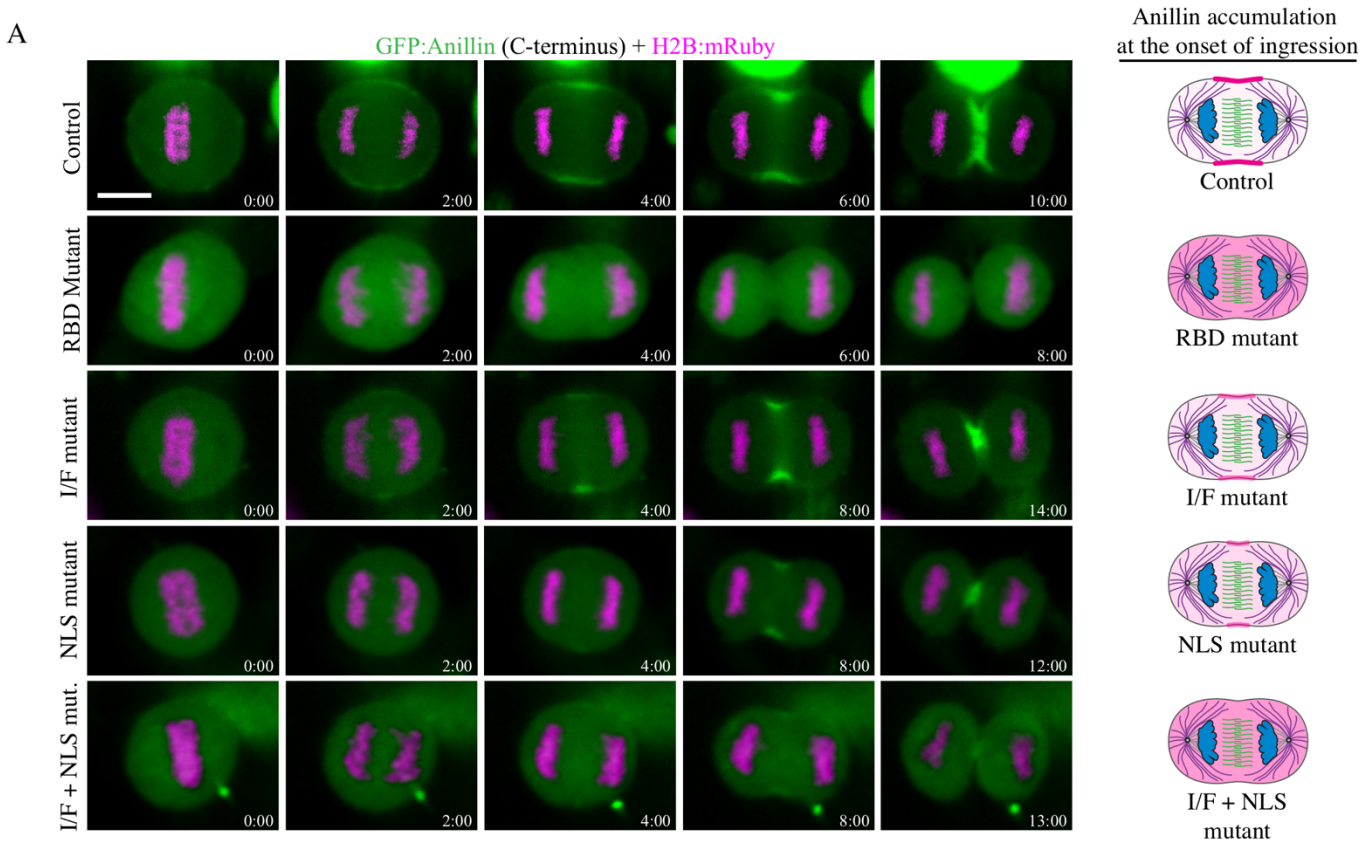
A
GFP:Anillin (C-terminus) + H2B:mRuby
Control
RBD Mutant
I/F mutant
NLS mutant
I/F + NLS mut.
0:00
2:00
4:00
6:00
8:00
10:00
12:00
13:00
14:00
Anillin accumulation
at the onset of ingression
Control
RBD mutant
I/F mutant
NLS mutant
I/F + NLS
mutant

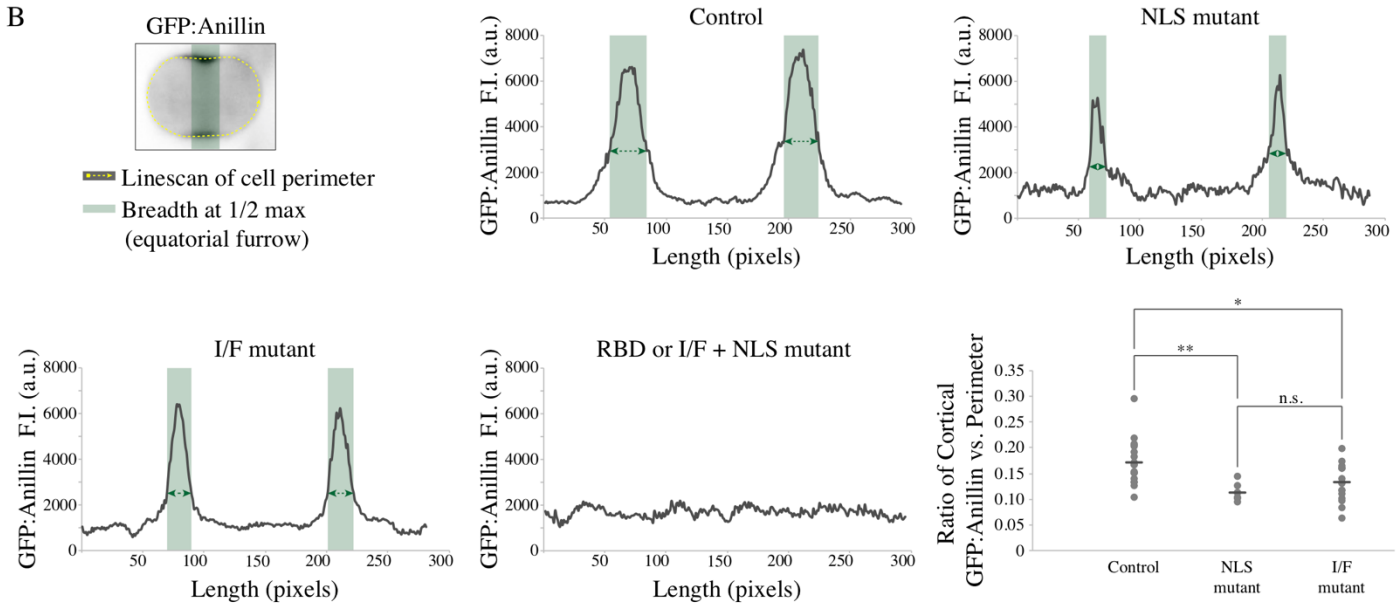
B
GFP:Anillin
Linescan of cell perimeter
Breadth at 1/2 max
(equatorial furrow)
Control
NLS mutant
I/F mutant
RBD or I/F + NLS mutant
GFP:Anillin F.I. (a.u.)
Length (pixels)
Ratio of Cortical
GFP:Anillin vs. Perimeter
n.s.
Control
NLS
mutant
I/F
mutant

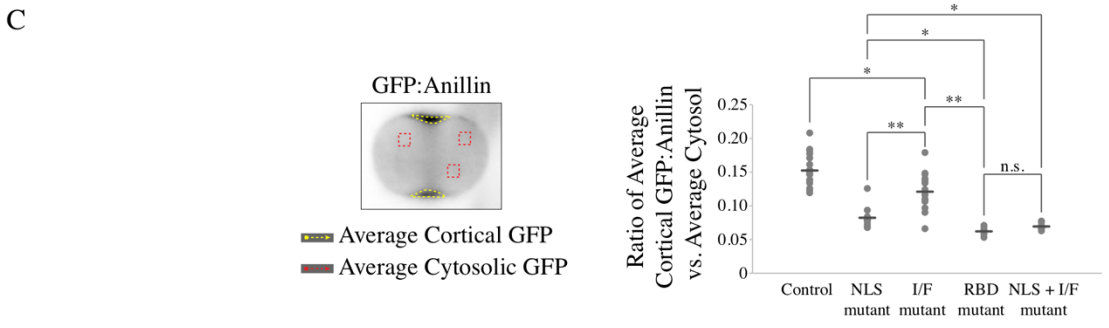
C
GFP:Anillin
Average Cortical GFP
Average Cytosolic GFP
Ratio of Average
Cortical GFP:Anillin
vs. Average Cytosol
n.s.
Control
NLS
mutant
I/F
mutant
RBD
mutant
NLS + I/F
mutant

Figure 12. Importin-binding enhances anillin's affinity for the equatorial cortex

A) Timelapse images show HeLa cells expressing GFP-tagged C-terminus anillin constructs (green) and H2B:mRuby (magenta; to show chromatin) as indicated: control (n=18), RhoA-binding domain mutant (RBD mutant; A703E, E721A; n=5), RBD-C2 interface mutant (I/F mutant; 843-DFEINIE to AFAINIA; n=15), NLS mutant (n=12), and a combination of the I/F + NLS mutations (I/F + NLS mutant; n=8). Times are indicated from anaphase onset. The scale bar is 10 μm. Cartoon cells show changes in the distribution of anillin (pink) at the onset of ingression for the different constructs as indicated. **B**) Graphs of line scans are shown for the different constructs as in A), with fluorescence intensity on the Y-axis and length (pixels) on the X-axis. The line scan (dotted yellow) was drawn as shown on the cell image (upper left). Regions of the cortex above 50% maximum levels are highlighted in green and represent accumulated anillin. To the right, a dot plot shows changes in the ratio of the breadth of accumulated anillin vs. total cell perimeter (Y-axis) for the control and mutants as indicated. The means are indicated by the dark grey lines, and significance was determined using the Student's t test (* $p < 0.05$, ** $p < 0.001$). **C**) The cell image (left) shows the area (yellow dotted line) measured to determine the average intensity of GFP-tagged anillin at the cortex, and the ROI's (red boxes) used to calculate the average intensity of anillin in the cytosol. The dot plot shows the average ratio of cortical anillin vs. cytosol (Y-axis) for the control and mutants in A) as indicated. The means are indicated by the dark grey lines, and significance was determined using the Student's t test (* $p < 0.05$, ** $p < 0.001$).

mutant were strongly enriched in the cytosol similar to the RBD mutant (**Figure 12C**). This data suggests that RhoA and importin-binding work together to control anillin's cortical localization during cytokinesis.

We further assessed the impact of these mutations on anillin's function in the context of the full-length protein and its requirement for cytokinesis. Constructs containing RNAi-resistant GFP-tagged full-length anillin, or with mutations in the NLS, I/F, or both, were expressed in HeLa cells depleted of endogenous anillin and co-expressing mCherry:Tubulin to visualize the mitotic spindle. Cells were imaged after anaphase onset to assess localization and cytokinesis phenotypes (**Figure 13A**). As expected, anillin localized to the cortex ~2 minutes after anaphase onset and was restricted to the equatorial cortex as the contractile ring ingressed (100% of cells successfully ingressed; **Figure 13A** and **B**). Cortical recruitment of the I/F mutant was delayed until ~4 minutes after anaphase onset, and was restricted to a narrow region. A small proportion of cells expressing the I/F mutant failed cytokinesis (22.7%; **Figure 13B**) and those that completed ingression took longer compared to control cells (17.8 ± 4.3 mins vs. 12.3 ± 2.7 mins; **Figure 13C**). Cortical recruitment of the NLS mutant was also delayed and restricted to a narrow region. As previously reported, a subset of cells expressing the NLS mutant failed cytokinesis (36.4%; **Figure 13A** and **B**), and those cells that completed ingression took longer compared to control cells (16.4 ± 3.5 mins; **Figure 13C**). Anillin containing both the NLS and I/F mutations failed to localize to the cortex, and the majority of cells failed cytokinesis (70.6%; **Figure 13A** and **B**). Those cells that ingressed were significantly delayed compared to control cells (19.2 ± 1.6 mins; **Figure 13C**).

To further assess how these mutations affect cytokinesis at the population level, we performed experiments as above on asynchronous populations of HeLa cells. We calculated the proportion of binucleate cells for each construct as a read-out for cytokinesis failure (**Figure 13D**).

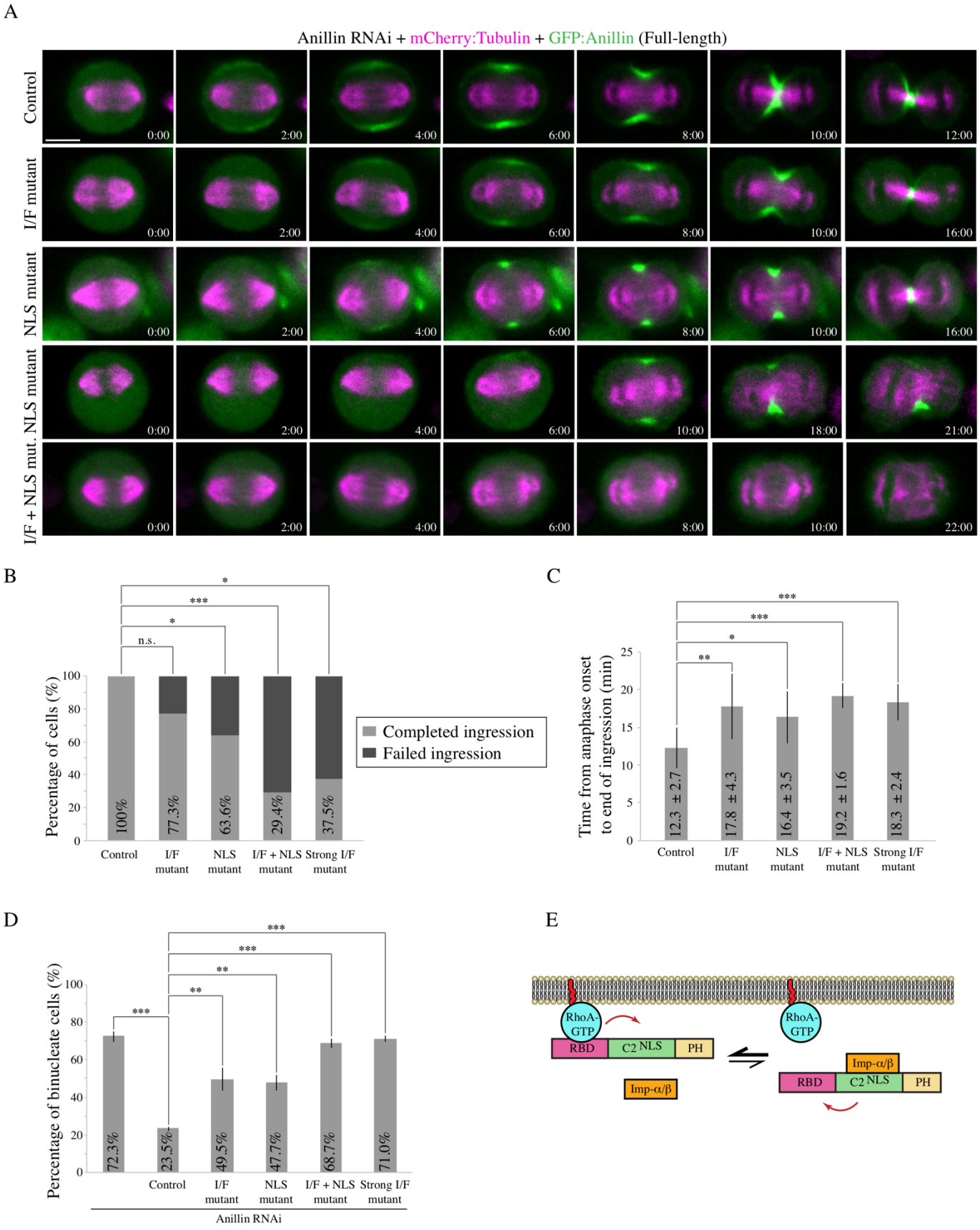
A
Anillin RNAi + mCherry:Tubulin + GFP:Anillin (Full-length)
Control
I/F mutant
NLS mutant
I/F + NLS mut. NLS mutant
0:00
2:00
4:00
6:00
8:00
10:00
12:00
16:00
18:00
21:00
22:00
B
Percentage of cells (%)
n.s.
*
***
Completed ingression
Failed ingression
100%
77.3%
63.6%
29.4%
37.5%
Control
I/F mutant
NLS mutant
I/F + NLS mutant
Strong I/F mutant
C
Time from anaphase onset to end of ingression (min)
**
12.3 ± 2.7
17.8 ± 4.3
16.4 ± 3.5
19.2 ± 1.6
18.3 ± 2.4
D
Percentage of binucleate cells (%)
72.3%
23.5%
49.5%
47.7%
68.7%
71.0%
Anillin RNAi
E
RhoA-GTP
RBD
C2 NLS
PH
Imp-α/β

Figure 13. Anillin requires importin-binding and the interface between the RBD and C2 domains for cytokinesis

A) Timelapse images show HeLa cells treated with anillin RNAi to deplete endogenous anillin, expressing various RNAi-resistant GFP-tagged full-length anillin constructs (green) and mCherry:Tubulin (magenta) as indicated: control, RBD-C2 interface mutant (I/F mutant), NLS mutant, and a combination of the I/F + NLS mutations (I/F + NLS mut.). Times are indicated from anaphase onset. The scale bar is 10 μm. **B**) A bar graph shows the percentage of cells (Y-axis) that failed ingression (light grey) compared to those that completed ingression (dark grey) for the different constructs in A) as indicated: control (n=15), I/F mutant (n=22), NLS mutant (n=22), I/F + NLS mutant (n=17), and *strong* I/F mutant (Strong I/F mutant; L735D, L736D; n=16). The data were analyzed using Fisher's exact test (n.s., not significant; *p < 0.05; **p < 0.001; ***p ≤ 0.0001). **C**) A bar graph shows the time from anaphase onset to the end of ingression (Y-axis) in cells rescued with the various anillin constructs in A): control (n=15), I/F mutant (n=17), NLS mutant (n=14), I/F + NLS mutant (n=5) and Strong I/F mutant (n=6). Bars indicate SD, which are also shown as time on the graph. Data was analyzed and p values were determined by Student's t test (*p < 0.05; **p < 0.001; ***p ≤ 0.0001). **D**) A bar graph shows the percentage of binucleate cells (Y-axis) as a readout for cytokinesis failure in populations of asynchronous HeLa cells after anillin RNAi and co-expressing with the indicated RNAi-resistant constructs. Bars show SD (n=3 replicates for each condition). Data was analyzed and p values were determined by the Student's t test (**p < 0.001; ***p ≤ 0.0001). **E**) A schematic shows how importin-binding (orange) may increase RhoA-binding (RhoA-GTP in blue; RBD in pink) or reduce its off-rate by stabilizing a favorable conformation of the RBD and C2 domain (green; NLS also shown). The PH domain is in yellow.

There was a significant increase in the proportion of binucleate cells depleted of endogenous anillin and expressing RNAi-resistant I/F mutant anillin (49.5% compared to cells expressing control anillin 23.5%), which was also observed in cells expressing the NLS mutant (47.7%). However, there was an even greater increase in the proportion of binucleate cells expressing anillin with both the NLS and I/F mutations, which was similar to the anillin RNAi control (68.7% vs. 72.3%). This data shows that weakening the interface of the RBD and C2 causes a dramatic change in anillin's recruitment when importin-binding is lost, suggesting that there is feedback from the C2 domain to the RBD to facilitate RhoA-binding (**Figure 13E**). To test this hypothesis, we performed *in vitro* experiments to determine how importin-binding influences anillin's interaction with RhoA. MBP:Anillin RBD + C2 was used to pull down His-tagged RhoA-GDP or RhoA-GTP in the presence or absence of GST:Importin-β (**Figure S7**). Adding importin-β increased anillin's affinity for GTP-bound RhoA, suggesting that importin-binding alters the RBD to make it more accessible and/or to stabilize its interaction with active RhoA (**Figure 13E**).

3.4.5 Cortical recruitment of anillin relies on the interface between the RBD and C2

Our data suggests that the interface between the RBD and C2 domains contributes to anillin function. While active RhoA-binding makes the C2 more accessible for importin-binding, importin-binding also makes the RBD for accessible for binding to active RhoA. To further test how the interface mediates anillin's ability to interact with importin-β or RhoA, we created point mutations within the RBD (*strong* I/F mutant; L735D, L736D) to specifically disrupt hydrophobic interactions with the C2 domain (**Figure 14A**). Based on their position, these mutations should more strongly disrupt the interface vs. the mutations described above (843-DFEINIE to AFAINIA). First, we assessed how the *strong* I/F mutations affect autoinhibition of the NLS in

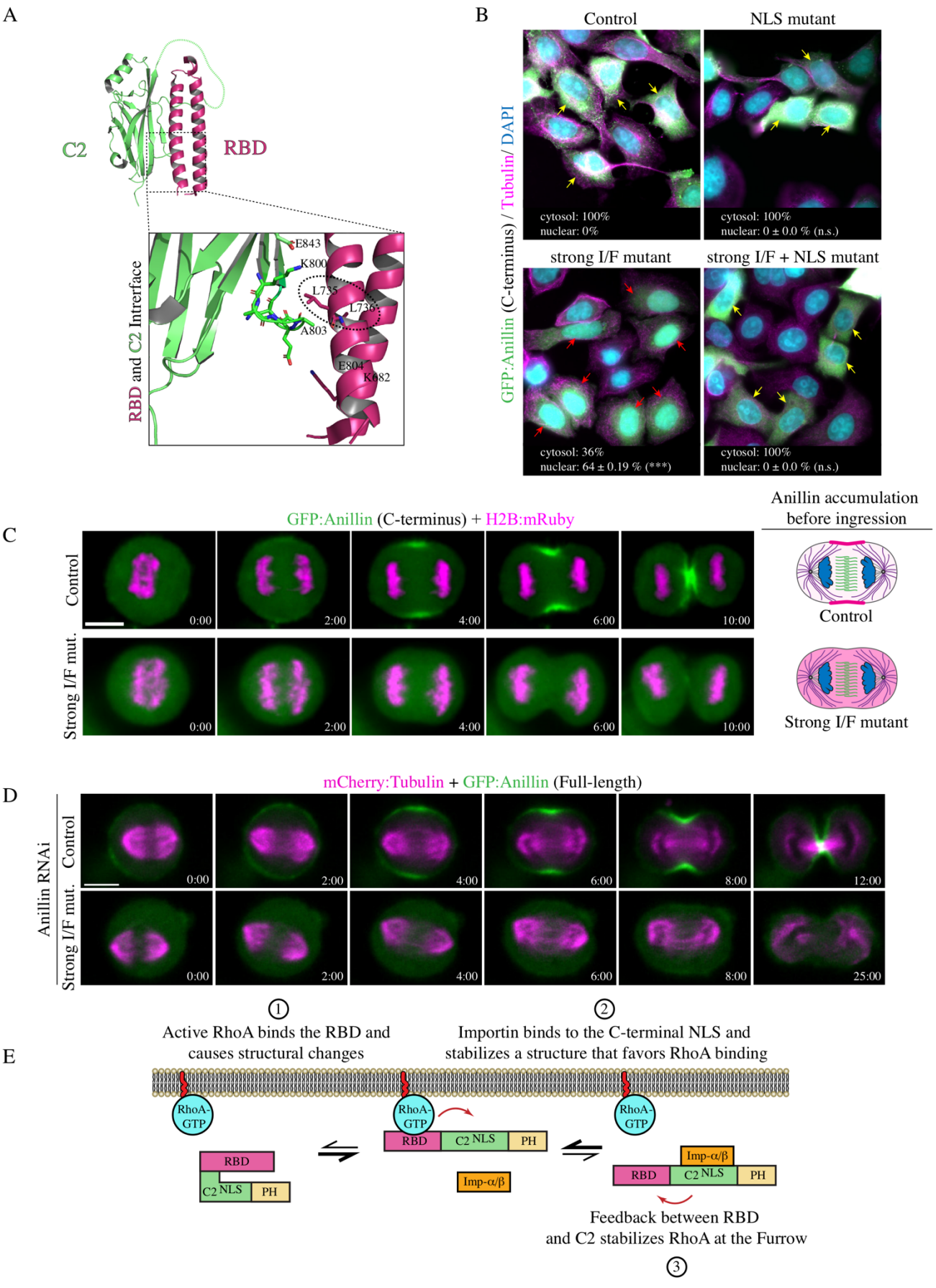
A
C2
RBD
RBD and C2 Intrerface
E843
K800
L735
L736
A803
E804
K682
B
Control
NLS mutant
GFP:Anillin (C-terminus) / Tubulin/ DAPI
cytosol: 100%
nuclear: 0%
cytosol: 100%
nuclear: 0 ± 0.0 % (n.s.)
strong I/F mutant
strong I/F + NLS mutant
cytosol: 36%
nuclear: 64 ± 0.19 % (***)
cytosol: 100%
nuclear: 0 ± 0.0 % (n.s.)
C
GFP:Anillin (C-terminus) + H2B:mRuby
Control
Strong I/F mut.
0:00
2:00
4:00
6:00
10:00
Anillin accumulation before ingression
Control
Strong I/F mutant
D
mCherry:Tubulin + GFP:Anillin (Full-length)
Anillin RNAi
Control
Strong I/F mut.
0:00
2:00
4:00
6:00
8:00
12:00
25:00
E
① Active RhoA binds the RBD and causes structural changes
② Importin binds to the C-terminal NLS and stabilizes a structure that favors RhoA binding
RhoA-GTP
RBD
C2
NLS
PH
Imp-α/β
Feedback between RBD and C2 stabilizes RhoA at the Furrow
③

Figure 14. The interface between the RBD and C2 domains is required for feedback for robust cortical recruitment and cytokinesis

A) A ribbon structure shows the intramolecular interface between the RBD (pink) and C2 domain (green). The boxed inset (left) shows the amino acids that form electrostatic and hydrophobic interactions at the interface. The amino acids that were mutated to generate a *strong* I/F mutant are circled (L735D and L736D). **B**) Images show fixed HeLa cells expressing GFP-tagged anillin C-terminus, or the NLS mutant, *strong* I/F mutant, or *strong* I/F + NLS mutant, stained for GFP (green), tubulin (red), and DAPI (DNA; blue). Yellow arrows point to cytosol localization, while red arrows point to nuclear localization. The percentage of cytosolic vs. nuclear localization is indicated for each condition. SD are shown (n=3 replicates for each condition) and significance was determined using the Student's t test (n.s., not significant, *** $p < 0.0001$). **C**) Timelapse images show HeLa cells expressing GFP-tagged C-terminus anillin or containing the *strong* I/F mutations (green) and H2B:mRuby (magenta; to show chromatin; control, n=18; *strong* I/F mutant, n=7). Times are indicated form anaphase onset. The scale bar is 10 μm. Cartoon cells on the right show changes in the distribution of anillin (pink) at the onset of ingression for control vs. the *strong* I/F mutant. **D**) Timelapse images show HeLa cells treated with anillin RNAi and co-expressing RNAi-resistant GFP-tagged full-length (control; n=15) or *strong* I/F mutant (n=16) anillin (green), and mCherry:Tubulin (magenta). Times are indicated form anaphase onset. The scale bar is 10 μm. Times are indicated form anaphase onset. The scale bar is 10 μm. **E**) A cartoon schematic shows how importin-binding enhances the RhoA-mediated recruitment of anillin to the equatorial cortex during cytokinesis. (1) RhoA is activated at anaphase onset and binds to the RBD (pink) to recruit anillin to the equatorial cortex. Active RhoA (blue) increases anillin's affinity for importin by causing conformational changes between the RBD and C2 domain (green). (2) Near

the cortex, importin-β (orange) binds to anillin via the C-terminal NLS, which (3) feeds back by stabilizing a conformation that enhances RhoA binding to the RBD via increasing affinity or reducing dissociation.

the C2 domain. We previously showed that the C-terminus of anillin fails to localize to the nucleus in interphase cells, but is nuclear after removing the RBD (Beaudet et al., 2017). We measured changes in the nuclear localization of the C-terminus of GFP-tagged anillin with mutations in the NLS, *strong* I/F, or *strong* I/F + NLS. Based on relative levels, their distribution was categorized as nuclear or cytosolic, and only considered if their average fluorescence intensity was over 1500 a.u. As expected, the C-terminus localized primarily to the cytosol in interphase cells (**Figure 14B**). Introducing the *strong* I/F mutations caused the C-terminus to localize to the nucleus in approximately 64% of the cells, which was lost when the NLS was also mutated (**Figure 14B**). Therefore, the *strong* I/F mutations are sufficient to relieve autoinhibition from the RBD, and do not impact importin-binding.

Next, we wanted to compare how the *strong* I/F mutant affects importin-binding after manipulating active RhoA or RhoA-binding as in Figure 11C. We used recombinant MBP:Anillin (RBD + C2) control, RBD mutant, or the *strong* I/F mutant to pull-down GFP-tagged Importin-β from lysates +/- active RhoA (**Figure 11D**). As before, we used overexpression (O/E) of the C-terminus of Ect2 [Myc:Ect2 (C-term)] to generate active RhoA, and Ect2 RNAi to reduce active RhoA. We found that Importin-β:GFP had higher affinity for the *strong* I/F mutant compared to control regardless of the levels of active RhoA, while the RBD mutant showed the opposite trend (**Figure 11D**). This data supports the idea that the *strong* I/F mutant mimics an 'open' conformation of anillin that no longer requires RhoA-binding for increased accessibility of the NLS.

Next, we determined how disrupting the interface affects anillin's localization and function during cytokinesis. Cells expressing GFP-tagged C-terminus of anillin or with the *strong* I/F mutations, and H2B:mRuby to visualize chromatin, were imaged after anaphase onset. As

previously described, anillin localized to the cortex ~2 minutes after anaphase onset and accumulated at the equatorial cortex during ingression. However, anillin containing the *strong* I/F mutations failed to localize to the cortex and remained cytosolic through ingression (**Figure 14C**). To determine how the *strong* I/F mutant impacts anillin's function for cytokinesis, RNAi-resistant GFP-tagged full-length anillin or containing the *strong* I/F mutations were imaged in HeLa cells depleted of endogenous anillin and co-expressing mCherry:Tubulin (**Figure 14D**). Full-length anillin localized similar to the C-terminus as previously described and all cells completed ingression, while the *strong* I/F mutant failed to localize to the cortex and the majority of cells failed to ingress (62.5%; **Figure 13B**). Cells that successfully ingressed were significantly delayed compared to control cells (18.3 ± 2.4 mins; **Figure 13C**). Thus, the localization and phenotype of the *strong* I/F mutant resembles constructs containing mutations in the RBD, or in both the I/F (*weak*; 843-DFEINIE to AFAINIA) and NLS. We also assessed how the *strong* I/F mutations impact cytokinesis at the population level and found that the proportion of binucleate cells was similar to the anillin RNAi control (71% vs. 72.3%; **Figure 13D**). This data suggests that the cortical affinity of anillin is regulated by importin-binding, which we propose feeds back through the interface to influence anillin's cortical recruitment by RhoA.

3.5 Discussion

Our studies shed light on how anillin's function for cytokinesis is regulated at the intramolecular level by active RhoA and importin-β. Our previous study showed that cytokinesis is regulated by Ran-GTP, which may coordinate ring positioning with chromatin (Beaudet et al., 2017). We also showed that anillin is a target of this pathway, as it contains a highly conserved NLS that binds to importin-β, and is required for its proper localization and function during

cytokinesis (Beaudet et al., 2017). As described earlier, a gradient of active Ran persists around chromatin, and importin-bound cargo form an inverse gradient (Kaláb and Heald, 2008). Having high importins free to bind to cargo near the equatorial cortex could help regulate cortical proteins required for cytokinesis. Here we delve into the mechanism by which importin-binding regulates anillin function. Our model (**Figure 14E**) is that when the levels of active RhoA increase upon anaphase onset, the binding of active RhoA to the RBD causes a conformational change in anillin that makes the neighbouring C2 domain more accessible to binding partners. One of these partners is Importin-β, which binds to the NLS in the C2 domain. Importin-binding then stabilizes the open conformation to reinforce binding to active RhoA as well as to other factors required for anillin's recruitment and retention at the equatorial cortex. Our binding data supports this model by showing that active RhoA increases anillin's affinity for importin, and vice versa. Our localization data also shows the importance of the interface between the RBD and C2 domain, which is required for feedback likely to position the domains for binding RhoA and importin with optimal affinity.

While our work focused on importin-binding, it is important to note that the C2 domain also contains binding sites for microtubules and phospholipids that may be autoinhibited by the RBD. Further, microtubule or lipid binding to the C2 domain also could influence anillin's affinity for active RhoA. We previously found that there was an inverse correlation with anillin's localization to microtubules vs. the cortex, depending on the levels of active RhoA or the stability of microtubules (van Oostende Triplet et al., 2014). In addition, a recent study showed that phospholipid binding may facilitate feedback to reinforce RhoA binding (Budnar et al., 2019).

3.5.1 Importin-binding regulates anillin's affinity for the equatorial cortex

Anillin is recruited to the equatorial cortex by active RhoA and is restricted from the polar cortices by astral microtubules. Previous studies showed that reducing active RhoA or stabilizing microtubules with Taxol increase anillin's localization to microtubules, suggesting that they compete with each other (van Oostende Triplet et al, 2014). We also found that mutating the NLS to reduce importin-binding weakens anillin's cortical affinity, since its recruitment is delayed and more restricted compared to non-mutant anillin. In addition, disrupting astral microtubules causes the NLS mutant to spread along the cortex, suggesting that the weakened affinity favors a transition in its localization to microtubules (Beaudet et al., 2017). Here we continued to explore how importin-binding affects anillin's cortical properties by performing FRAP studies. NLS mutations that reduce importin-binding decreased anillin's mobility and increased its off-rate (**Figures 9** and **10**). The reduced mobility likely reflects the shift onto microtubules, since we also saw reduced mobility of anillin when microtubules were overextended by MCAK RNAi (**Figure 10**). Interestingly, when the NLS is mutated, anillin's affinity for microtubules is not increased per se, since we found via co-sedimentation assays that its affinity is partially reduced (**Figure S6**). Thus, the reduced mobility via the NLS may be indirect due to an increase in microtubule localization caused by an overall reduced affinity for RhoA. We also saw an increased off-rate with the NLS mutant that we did not see with MCAK RNAi, which may indicate that importin-binding specifically regulates cortical retention.

3.5.2 RhoA-binding relieves autoinhibition of the C2 domain from the RBD

We previously found that the C2 domain in the C-terminus of anillin had higher affinity for importin and microtubules when the RBD was removed (Beaudet et al., 2017). Since the RBD binds to active RhoA, we proposed a model where active RhoA-binding could induce a

conformational change that makes the C2 more accessible. Here, we tested this model by changing the levels of active RhoA or mutating the RBD and seeing how this influenced importin-binding. In support of our model, when active RhoA levels were high (*e.g.* overexpressed GEF domain of Ect2), we saw increased importin-binding compared to when active RhoA levels were low (*e.g.* Ect2 RNAi), or when the RBD was mutated (**Figure 11**). Thus, similar to other RhoA effectors, such as mDia, intramolecular autoinhibition could ensure that anillin's other interactions such as binding to phospholipids, are closely linked to when active RhoA levels increase during mitotic exit, and in the region of the equatorial cortex (Li and Higgs, 2003; Lammers et al., 2005).

3.5.3 Feedback at the interface between the RBD and C2 domain drives anillin's equatorial recruitment

Our data shows that the NLS of anillin influences its cortical properties. One hypothesis is that the C2 domain feeds back to the RBD to improve accessibility to active RhoA or reduce its off-rate. Indeed, when the NLS mutations were combined with mutations that weaken the interface between the RBD and C2, anillin failed to be recruited to the cortex and failed to support cytokinesis, similar to mutations that disrupt the RBD (**Figures 12** and **13**). Introducing mutations predicted to more strongly disrupt the interface similarly failed to localize or function, even though binding to importin increased (**Figures 13** and **14**). Thus, we hypothesize that communication at this interface enables feedback between the RBD and C2 domain that drives the RhoA-mediated recruitment of anillin. Since the C2 domain has binding sites for other factors, it would be interesting to determine how these other interactions also impact binding to RhoA. For example, as described above, stabilizing microtubules competes anillin from the cortex. Since the microtubule- and importin-binding sites overlap, stabilizing microtubules may outcompete

importins and sterically hinder the RBD for optimal RhoA binding. In addition, previous studies suggest that there is cooperativity between anillin's interaction with phospholipids and RhoA, which could involve a feedback mechanism (Sun et al., 2015; Budnar et al., 2019). The lipid binding site is predicted to be at a loop near the NLS, and lipid binding could increase accessibility of the RBD to RhoA, similar to importin. Anillin likely is also regulated by post-translational modifications that may influence its conformation. For example, a recent study showed that phosphorylation at a site that lies just N-terminal to the RBD enhances anillin's cortical association and is required for cytokinesis (Kim et al., 2017). This area is under-explored and it would be interesting to see how phosphorylation by different cell cycle kinases influences anillin's structural changes and function for cytokinesis.

Chapter 4: Conclusion and Model

4.1 Overview

Cytokinesis is a fundamental process that occurs at the end of mitosis and is required for the development and maintenance of any organism. This process is dependent on an actomyosin contractile ring, which assembles at the equatorial plane between segregating chromatids. We study the mechanisms that spatially and temporally regulate the division plane in mammalian cells. Mitotic spindle pathways and microtubule-independent pathways regulate the division plane to ensure that cytokinesis is coupled with chromosome segregation. Failure to do so could lead to fate changes and aneuploidy, which could cause cancer. Spindle-dependent mechanisms have been studied more robustly, and likely are the predominant way to generate active RhoA at the equatorial cortex in symmetrically dividing cells. However, cells that are polarized and/or have altered ploidy may rely on additional mechanisms to ensure that cytokinesis occurs properly. Our knowledge of the microtubule-independent pathways that regulate cytokinesis is more limited and requires further investigation, especially in different cell types and model systems.

This thesis elucidates a role for Ran-GTP in regulating the equatorial cortex for cytokinesis. Based on our findings we propose a model where anillin integrates signals from Ran-GTP via importin-binding and active RhoA to spatially regulate the division plane (**Figure 15**). At the onset of anaphase, active RhoA recruits anillin to the cortex by binding to the RBD. This induces conformational changes between the RBD and C2 domain to enable accessibility for importin-binding to an NLS within the C2 domain. Ran-GTP forms a gradient during mitosis, with the highest levels of active Ran close to chromatin and lower levels towards the cortex. Since Ran-GTP releases importins from cargo, there is an inverse gradient where importins are free to bind

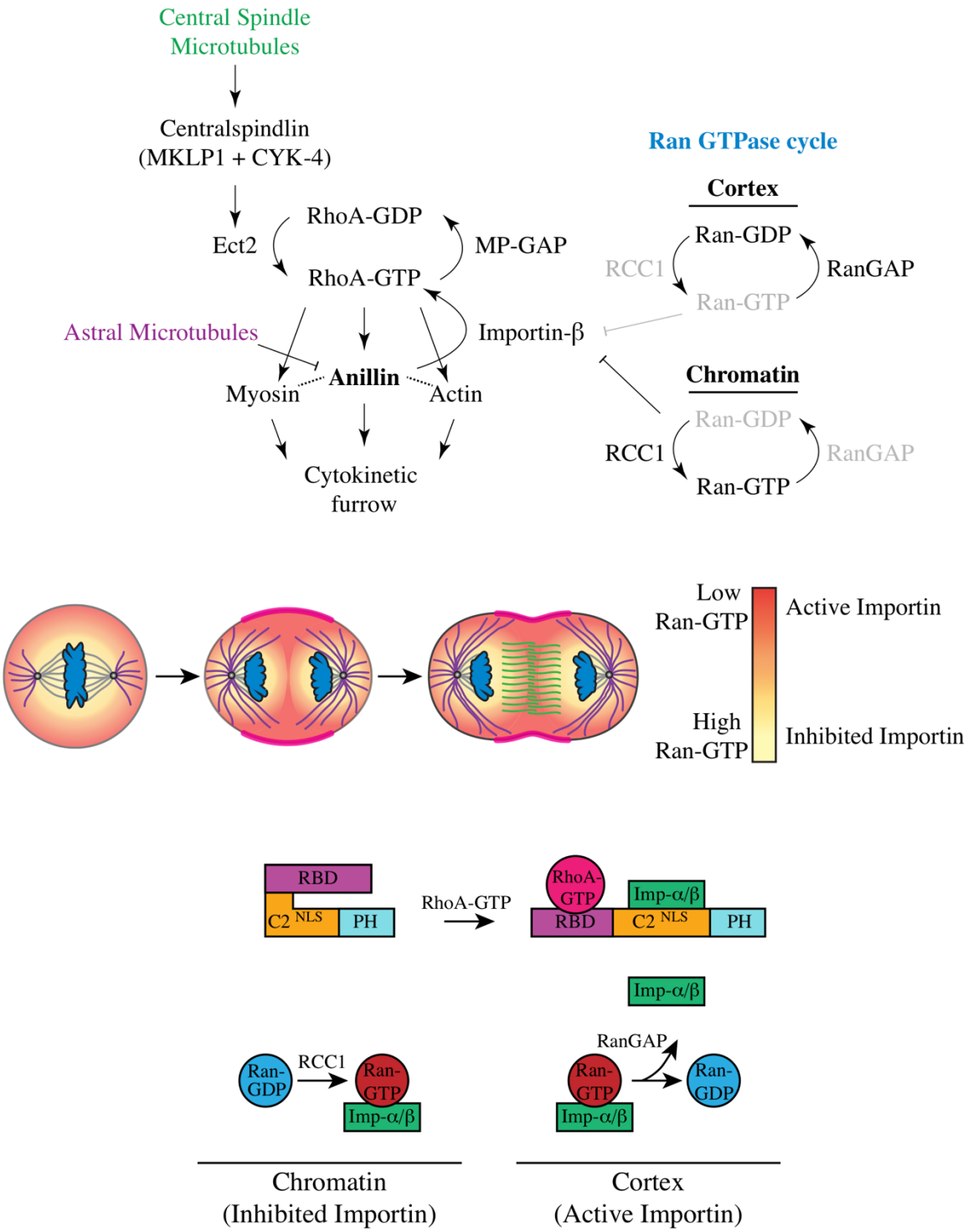
Central Spindle Microtubules
Centralspindlin (MKLP1 + CYK-4)
Ect2
RhoA-GDP
RhoA-GTP
MP-GAP
Astral Microtubules
Myosin
Anillin
Actin
Importin-β
Cytokinetic furrow
Ran GTPase cycle
Cortex
Ran-GDP
RCC1
RanGAP
Ran-GTP
Chromatin
Ran-GDP
RCC1
RanGAP
Ran-GTP
Low Ran-GTP
Active Importin
High Ran-GTP
Inhibited Importin
RBD
C2 NLS
PH
RhoA-GTP
RhoA-GTP
Imp-α/β
RBD
C2 NLS
PH
Imp-α/β
RanGAP
Ran-GDP
RCC1
Ran-GTP
Imp-α/β
Ran-GTP
Imp-α/β
Ran-GDP
Chromatin
(Inhibited Importin)
Cortex
(Active Importin)

Figure 15. Importin-mediated regulation of anillin during cytokinesis

The pathway shows how different inputs are integrated by anillin to spatially position the cytokinetic furrow. The central spindle signals to the overlaying cortex to activate RhoA-GTP, which subsequently leads to the recruitment of anillin and other contractile proteins to form the cytokinetic furrow. Astral microtubules restrict anillin from the polar cortex, while importins enhance anillin's recruitment to the equatorial cortex. Ran GTPase cycles between active and inactive forms and the Ran-GTP gradient spatially defines importins ability to regulate anillin function. Importins are bound to Ran-GTP near chromatin where levels of Ran-GTP are high, and are free to bind to cargo near the cortex where Ran-GTP levels drop below a threshold concentration. Under the pathway, the cartoon cells show the different stages of mitosis to conceptualize the spatial range of the Ran-GTP gradient during metaphase, anaphase, and early telophase. While the gradient is spherical in metaphase, as chromatin moves toward the cell poles in anaphase, the gradient changes such that importins free to bind to cargo would enrich near the equatorial cortex. Below, a schematic shows how anillin's function is regulated by active RhoA upon anaphase onset and subsequently by importins near the cortex. Active RhoA binds to anillin causing conformational changes between the RBD and C2 domain to expose binding sites for importin and potentially other binding partners. Importin-binding stabilizes a conformation that further enhances RhoA-binding. Feedback between the RBD and C2 domains enables anillin's cortical enrichment.

to cargo near the cortex (**Figure 15**). Our data suggests that importins bind to anillin in proximity to the equatorial cortex and stabilize a conformation that favors cortical recruitment. Importin-binding promotes positive feedback between anillin and active RhoA, which is coordinated through an intramolecular interface between the RBD and C2 domain (**Figure 15**). Thus, intramolecular regulation of anillin by RhoA and importins is crucial for anillin's cortical localization and function for cytokinesis.

The premise of this thesis stems from studies where chromatin-associated Ran-GTP was shown to regulate cortical proteins. The majority of studies on the mitotic Ran-GTP gradient have focused on its role in bipolar spindle assembly (Kaláb et al., 2002; Kaláb et al., 2006). During mitosis, Ran-GTP levels are highest around chromatin and form an inverse gradient to importins that are bound to cargo. Near chromatin, Ran-GTP binds to importins and releases them from cargo that include spindle assembly factors (Kaláb and Heald, 2008; Weaver and Walczak, 2015). The textbook model is that when importins are released from these factors, they form active complexes with binding partners to help build a bipolar spindle (Weaver and Walczak, 2015). However, more recent studies suggest that this model is too simplistic. For example, either importin-α or -β can bind to NLS sites with different additional contact sites that could affect the cargo in different ways (Kaláb and Heald, 2008). While some contacts could sterically hinder binding to a partner, others could induce intramolecular changes that alter binding affinity to multiple partners. In addition, the Ran-GTP gradient is quite steep, suggesting that even at short distances away from chromatin, some factors likely would not be sufficiently released from importins where they are functionally required. Therefore, an updated model should be considered where the Ran-GTP gradient acts as a molecular ruler, and each factor regulated by the gradient could have a unique response based on different binding affinities for importin-α and/or -β and its binding partners.

Few studies have investigated the regulation of cortical proteins by the Ran-GTP gradient. In mouse oocytes, the Ran-GTP gradient was shown to function as a molecular ruler to position contractile proteins with respect to chromatin position for polar body extrusion (Deng et al., 2007). In oocytes, a very small meiotic spindle forms near the cortex to segregate chromatin. A signal associated with chromatin is crucial to organize the cortex to ensure that a complement of chromosomes is extruded during meiosis (Deng et al., 2007). Subsequent studies suggest that Cdc42 could be regulated by the Ran pathway to form the polar cap (Dehapiot et al, 2013; Dehapiot and Halet, 2013). In *Drosophila* syncytial embryos, Ran-GTP influences pseudocleavage (Silverman-Gavrila et al., 2008). They found that anillin's recruitment to the newly formed membrane is reduced by the overexpression of importin-α, which also reduces its interaction with septins (Silverman-Gavrila et al., 2008). Their model is that in the presence of high Ran-GTP, anillin is released from importins to permit septin-binding at the cortex. However, one issue with this model is that membranes invaginate between nuclei, not close to them, suggesting that the location where anillin accumulates is where the levels of Ran-GTP would be low, not high. In addition, their study was based on overexpression, not loss-of-function, making their data difficult to interpret. Another study from Kiyomitsu and Cheeseman (2013) hypothesized that Ran-GTP plays a role in human cells to recover the division plane when the mitotic spindle shifts too close to one pole. In cells lacking polymerized microtubules and forced to exit mitosis, anillin clears from regions of the cortex near chromatin and this clearance depends on Ran-GTP. However, they did not study the requirement for Ran-GTP in cytokinesis of cells with intact spindles. Importantly, their model suggests that Ran-GTP has an inhibitory role in regulating cortical proteins, which contradicts the model proposed by Silverman-Gavrila et al., (2008).

Data supporting our model is presented in Chapters 2 and 3. In Chapter 2, we describe how a chromatin-based pathway functions via Ran-GTP to regulate cytokinesis. Altering Ran-GTP levels, or ectopically localizing active Ran to the equatorial cortex influences the localization of contractile proteins and causes cells to fail cytokinesis (**Figures 3** and **4**). We show that in cells depleted of active Ran, the localization of contractile proteins broadens, and they fail cytokinesis due to incomplete membrane ingression. This data suggests that active Ran is crucial for successful cytokinesis and that it signals to the cortex to restrict the zone of contractile ring assembly. In support of this, the cleavage furrow oscillates in cells that have ectopically localized active Ran at the equatorial furrow (**Figure 4**). Interestingly, this phenotype is also observed in cells depleted of anillin; the contractile ring is not securely anchored to the plasma membrane and oscillates around the cell as it constricts (Piekny and Glotzer, 2008). This data suggests that anillin is a target of the Ran pathway. Indeed, anillin is required to polarize the cortex in cells lacking microtubules and forced to exit mitosis in response to chromatin position (**Figure 5**; Kiyomitsu and Cheeseman, 2013). Anillin depletion blocks polarization and reintroducing either full-length or the C-terminus of anillin rescues polarization (**Figure 5**). This suggests that anillin responds to microtubule-independent cues that polarize the cortex. Using the logic that a component of the Ran pathway should contain an NLS, we found that human anillin contains a conserved NLS in its C-terminal C2 domain that interacts with importin-β and is required for polarization (**Figures 5, 6,** and **10**; Oegema et al., 2000). Interestingly, Silverman-Gavrila et al., (2008) showed that *Drosophila* anillin also binds to importins through a C-terminal NLS that aligns well with human anillin (**Figure 6**). Although their paper proposed that importins negatively regulate anillin's cortical recruitment via competing with septin-binding, their findings support the model that Ran-regulation of anillin's cortical localization is conserved (Silverman-Gavrila et al., 2008). We show

that the C-terminal NLS is required for anillin's localization and function during cytokinesis (**Figures 7**). Mutating the NLS delays anillin's cortical accumulation and causes it to localize to a narrow region compared to control anillin. In addition, a subset of cells depleted of endogenous anillin and co-expressing NLS mutant anillin fail cytokinesis due to oscillation of the cleavage furrow. We also found that anillin accumulation strongly correlates with the distance of chromatin to the cortex (**Figure 8**). As chromatin moves further away from the midzone, the intensity of anillin accumulation increases at the equatorial cortex proportional to the distance of chromatin to the anillin-enriched cortex. Mutating the NLS perturbs this correlation and anillin only accumulates at the cortex when signals from the central spindle are generated and are sufficient to recruit anillin. This data supports the hypothesis that importin-binding to anillin during early anaphase promotes its cortical accumulation at areas of the cortex that are furthest away from chromatin.

Our evidence also supports the idea that Ran-GTP functions as a molecular ruler to position contractile proteins a specific distance from chromatin similar to that proposed by Deng et al., (2007) for polar body extrusion. We found that overexpressing importin-β proportionally decreases the breadth of anillin accumulation, similar to NLS mutant anillin (**Figure 7**), suggesting that the local concentration of importin(s) is crucial for directing the accumulation of anillin at the cortex. At high concentrations, importin(s) could out-compete anillin's other interactions, such as binding to phospholipids or septins. Our model reconciles the findings by both Silverman-Gavrila et al., (2008) and Kiyomitsu and Cheeseman, (2013), where the Ran-regulation of anillin/cortical proteins was studied in different contexts. Silverman-Gavrila et al., (2008) investigated the role of importin-binding to anillin by the overexpression of importin-α, while Kiyomitsu and Cheeseman,

(2013) reduced Ran-GTP levels using a mutant. Both findings could be supported by the concept that importin(s) function as a molecular ruler to regulate anillin's cortical recruitment.

In addition, we describe how the C2 domain of anillin could be autoinhibited by the neighbouring RBD. The C-terminal NLS is located in a disordered loop emanating from the C2 domain, and removing the RBD increased anillin's affinity for importins and microtubules *in vitro* (**Figures 6** and **8**). The structure of the C-terminus of human anillin bound to RhoA-GTP was solved by Sun et al., (2015), which demonstrated the boundaries of the RBD and adjacent C2 domain. However, they were unable to resolve the disordered loop that contains the NLS. Our data showed that the RBD blocks binding sites within the C2 domain, and we propose that this inhibition is relieved by binding to active RhoA in a cell cycle-dependent manner (*discussed further below*). While RhoA-binding is required for accessibility of the C2 domain to binding partners, subsequent importin-binding could stabilize this 'open' conformation for robust cortical recruitment.

In Chapter 3, we delve deeper into the mechanism by which anillin function is regulated at the intramolecular level by active RhoA and importins. FRAP experiments were used to better understand anillin's cortical properties, where the maximum fluorescence recovery is a readout for mobility and the dissociation rate reveals its turnover at the furrow. Full-length anillin has lower mobility and turnover compared to the C-terminus (**Figure 9**). This is likely due to interactions with actin and myosin via the N-terminal domains, which enhances its retention at the equatorial furrow. The fast turnover and low cortical retention of the C-terminus is reminiscent of RhoA's cortical properties, which supports the idea that RhoA-binding governs properties of the C-terminus (Budnar et al., 2019). In support of our previous data, we found that mutating the C-terminal NLS changes the mobility and dissociation rate of cortical anillin (**Figure 10**),

demonstrating that importin also influences anillin's cortical recruitment or maintenance. We previously found that the overextension of astral microtubules using MCAK RNAi also decreases the amount of anillin in the equatorial furrow. We proposed that reducing anillin's cortical affinity favours its localization to microtubules. Thus, to determine if reduced cortical localization of NLS mutant anillin is strictly due to an enhanced affinity for microtubules, we determined the effect of the mutation on microtubule-binding using co-sedimentation assays, and FRAP of the C-terminus of anillin in MCAK RNAi treated cells. We found that introducing the NLS mutation slightly decreased vs. increased the binding of microtubules to the C2 domain. In addition, in MCAK RNAi cells, anillin's mobility at the equatorial cortex was reduced, however, its turnover was not affected. This data suggests that microtubules and importin-binding both influence anillin's mobility, but importins uniquely influence anillin's turnover. Thus, the reduced mobility of the NLS mutant C-terminus of anillin could occur because it is more strongly associated with microtubules, but likely because of a reduction in affinity for active RhoA vs. a 'direct' increase in microtubule affinity (van Oostende Triplet et al., 2014). In support of this, we propose that importin-binding slows down anillin turnover between the cytosol and the equatorial cortex by facilitating its association with active RhoA or phospholipids.

Our model is that binding to active RhoA through the RBD relieves the inhibition of binding sites within the C2 domain. In support of this, removing the RBD increased anillin's affinity for importin-binding and microtubule-binding (**Figures 6, 8,** and **10**; Beaudet et al., 2017). To demonstrate that active RhoA influences the affinity of binding interactions in the C2 domain, we performed biochemical assays using recombinant anillin to pull down importin from cell lysates after manipulating the levels of active RhoA in two different ways: by loading GDP vs. GTP, or by overexpressing or depleting Ect2 (RhoA GEF). Increasing active RhoA increased

anillin's affinity for importin (**Figure 11**). This data demonstrated that RhoA-GTP relieves autoinhibition of the C2 domain to expose binding sites for importins. This prompted us to further study the interface between the RBD and C2 domains. A previous study identified mutations that weakly perturb RhoA binding and anillin's cortical recruitment (Piekny and Glotzer, 2008). In light of the structure published by Sun et al., (2015) we found that one of these mutations map to the interface and is predicted to weakly perturb interactions between the RBD and C2. Interestingly, when combining this mutant with the NLS mutant, the localization of anillin to the equatorial cortex was strongly reduced and failed to support furrowing in rescue assays, similar to mutations in the RBD predicted to directly prevent RhoA-GTP binding (**Figures 12** and **13**; Sun et al., 2015). This data shows that both the interface and importin-binding are required for anillin's cortical localization and function, and suggests that there is feedback from the C2 domain to the RBD to reinforce RhoA-binding. To test this, we made targeted mutations that would more strongly disrupt the intramolecular interface between the RBD and C2 domain. Interestingly, we saw that introducing these mutations into the C-terminus caused it to be nuclear localized in interphase cells, although the C-terminus is not (**Figure 14**). This suggests that disrupting the interface causes the C2 to be relieved from inhibition by the RBD to permit importin-binding. However, C-terminal or full-length anillin constructs containing these mutations failed to localize to the equatorial cortex, and cells failed cytokinesis in rescue assays (**Figures 13** and **14**). Therefore, this demonstrates that feedback between the C2 and RBD is also required for stable association with active RhoA for cortical recruitment. In support of this, we found that importin-β increases anillin's affinity for active RhoA *in vitro* (**Figure S7**). We conclude from this data that importin-binding enables anillin's enrichment by potentiating its interaction with RhoA at the equatorial furrow, likely by stabilizing a conformation that favours RhoA binding.

4.2 Other Modes of Anillin Regulation

Anillin likely is regulated by phosphorylation and is predicted to have many phosphorylation sites. However, few studies have determined which sites are functional, and it has been challenging to identify kinases or phosphatases that regulate the different sites. The effect of phosphorylation could vary depending on the location, and how it affects anillin's affinity for other proteins or lipids. For example, a recent study showed that phosphorylation at a site that lies just N-terminal to the RBD enhances anillin's cortical association and is required for cytokinesis (Kim et al., 2017). While recent studies of Mid1, the yeast homolog, showed that phosphorylation of Mid1 by SIN kinase drives the removal of Mid1 from the cortex as the contractile ring begins to constrict (Willet et al., 2019). This area of study is under-explored and it would be interesting to see how phosphorylation by different cell cycle kinases influences anillin's structural changes and function for cytokinesis.

4.3 Perspectives

Our studies have demonstrated that a chromatin-associated pathway regulates cortical proteins to ensure that cytokinesis is accurately coupled with chromosome segregation, and it would be interesting to see how the requirement for this pathway varies depending on cell type. The studies conducted in this thesis were primarily done using symmetrically dividing HeLa cells, a cancer-derived cell line that is typically used for studying cytokinesis in human cells due to their amenability to transfection and microscopy. However, it would be interesting to test the requirement of this pathway in epithelial cells, which have apical/basal polarity that needs to be maintained during division. A number of studies showed that extrinsic forces from neighbouring cells influence asymmetric ingression of the contractile ring from the basal to the apical side of the cortex (Guillot and Lecuit, 2013; Morais-de-Sá and Sunkel, 2013; Bourdages et al., 2014).

However, how intrinsic mechanisms couple with extrinsic mechanisms to influence ingression have not been considered. Depending on the number of neighbouring cells and how forces are distributed, they may not be sufficient to fully support asymmetric ingression. In addition, experiments in *C. elegans* embryos showed that asymmetric ingression is intrinsic vs. extrinsic (Maddox et al., 2005; Maddox et al., 2007). As epithelial cells enter mitosis, the nucleus migrates toward the apical surface (Meyer et al., 2011; Spear and Erickson, 2012), and we propose that chromatin position also may influence contractile ring assembly and ingression kinetics. Preliminary studies in our lab found that anillin is asymmetrically distributed at the basal side of the cortex of MDCK cells (Madin-Darby Canine Kidney epithelial cells), and is required for asymmetric ingression of isolated cells (Mariotti and Piekny, unpublished observations).

We also propose that the Ran pathway could have stronger roles in different cell types depending on their ploidy. In some tissues, the polyploidization of cells is essential and occurs during the differentiation programs of specific cells in skeletal muscle, heart, placenta, liver, brain and blood (Pandit et al., 2013). There are different mechanisms by which different cell types gain ploidy, including failed cytokinesis caused by regression of the cleavage furrow (Geddis and Kaushansky, 2006; Gentric and Desdouets, 2014; Fox and Duronio, 2013). Thus, it would be interesting to determine if the Ran pathway sufficiently reduces the localization of contractile proteins to cause cytokinesis failure in cells that gain ploidy.

The Ran pathway could also be hijacked to regulate the division of cancer cells with aneuploidy. Cells in highly progressive metastatic cancers often display aneuploidy due to chromosomal instability (CIN), a hallmark of cancer (Hanahan and Weinberg, 2011; Lacroix and Maddox, 2012). CIN cells typically evade or have abnormal cell cycle checkpoints, permitting them to proceed through the cell cycle, which promotes further instability. One study showed that

in cancer cells with increased aneuploidy, Ran-GTP levels were higher around chromatin, which correlated with their ability to create robust, bipolar mitotic spindles to segregate chromatin (Hasegawa et al., 2013). Cells with increased aneuploidy had more RCC1 (GEF) in comparison to diploid cells (Hasegawa et al., 2013). We hypothesize that the enhanced Ran gradient in these cells also could regulate the contractile ring to more tightly control cytokinesis in response to chromatin. Anillin expression has also been shown to be upregulated in a plethora of cancers and correlates with the metastatic potential of tumour cells (Hall et al., 2005; Olakowski et al., 2009; Piekny and Maddox, 2010; Liang et al., 2015; Wang et al., 2016; Magnusson et al., 2016; Zeng et al., 2017). However, it is not well understood what role upregulated anillin may have for cytokinesis function and how this may contribute to tumour progression. Our lab is currently determining how the requirement for anillin varies in different cancers vs. healthy tissue with altered ploidy to explore this as a potential anti-cancer therapy. To date, there have not been any promising chemotherapeutic agents that specifically target cytokinesis in cancer cells. Thus, elucidating the redundant pathways that spatially regulate cytokinesis could uncover novel molecular targets for the development of new chemotherapies.

References

Adriaans I., Basant A., Ponsioen B., Glotzer M., and Lens S.M.A. (2019). PLK1 plays dual roles in centralspindlin regulation during cytokinesis. J. Cell Biol. *218*, 1250-1264.

Akhshi T.K., Wernike D., and Piekny A. (2014). Microtubules and actin crosstalk in cell migration and division. Cytoskeleton *71*, 1-23.

Basant A., and Glotzer M. (2018). Spatiotemporal regulation of RhoA during Cytokinesis. Curr. Biol. *28*, R570-R580.

Basant A., Lekomtsev S., Tse Y.C., Zhang D., Longhini K.M., Petronczki M., and Glotzer M. (2015). Aurora B Promotes Cytokinesis by Inducing Centralspindlin Oligomers that Associate with the Plasma Membrane. Dev. Cell *33*, 204-215.

Bassi Z.I., Audusseau M., Riparbelli M.G., Callaini G., and D'Avino P.P. (2013). Citron kinase controls a molecular network required for midbody formation in cytokinesis. Proc. Natl. Acad. Sci. U.S.A. *110*, 9782-9787.

Beaudet D., Akhshi T., Phillipp J., Law C., and Piekny A. (2017). Active Ran regulates anillin function during cytokinesis. Mol. Biol. Cell *28*, 3517-3531.

Beaudet D., Pham N., Skaik N., and Piekny A. (2019). Intramolecular regulation of anillin during cytokinesis. BioRxiv doi: 10.1101/726471.

Bement W.M., Benink H.A., and von Dassow G. (2005). A microtubule-dependent zone of active RhoA during cleavage plane specification. J. Cell Biol. *170*, 91-101.

Bourdages K.G., Lacroix B., Dorn J.F., Descovich C.P., and Maddox A.S. (2014). Quantitative analysis of cytokinesis in situ during *C. elegans* postembryonic development. PLoS One *9*, e110689.

Bringmann H., Cowan C.R., Kong J., and Hyman A. (2007). Let-99, GOA-1/GPA-16, and GPR-1/2 are required for aster-positioned cytokinesis. Curr. Biol. *17*, 185-191.

Bringmann H. and Hyman A.A. (2005). A cytokinesis furrow is positioned by two consecutive signals. Nature *436,* 731-734.

Brownlee C., and Heald R. (2019). Importin α Partitioning to the Plasma Membrane Regulates Intracellular Scaling. Cell *176*, 805-815.

Budnar S., Husain K.B., Gomez G.A., Naghibosadat M., Varma A., Verma S., Hamilton N.A., Morris R.G. and Yap A.S. (2019). Anillin Promotes Cell Contractility by Cyclic Resetting of RhoA Residence Kinetics. Dev. Cell *49*, 894-906.

Burkard M.E., Maciejowski J., Rodriguez-Bravo V., Repka M., Lowery D.M., Clauser K.R., Zhang C., Shokat K.M., Carr S.A., Yaffe M.B., and Jallepalli P.V. (2009). Plk1 self-organization and priming phosphorylation of HsCYK-4 at the spindle midzone regulate the onset of division in human cells. PLoS Biol. *7*, e1000111.

Cabernard C., Prehoda K.E., and Doe C.Q. (2010). A spindle-independent cleavage furrow positioning pathway. Nature *467,* 91-94.

Canman J.C., Cameron L.A., Maddox P.S., Straight A., Tirnauer J.S., Mitchison T.J., Fang G., Kapoor T.M., and Salmon E.D. (2003). Determining the position of the cell division plane. Nature *424,* 1074-1078.

Canman J.C., Hoffman D.B., and Salmon E.D. (2000). The role of the pre- and post-anaphase microtubules in the cytokinesis phase of the cell cycle. Curr. Biol. *10,* 611-614.

Carreno S., Kouranti I., Glusman E.S., Fuller M.T., Echard A., and Payre F. (2008). Moesin and its activating kinase Slik are required for cortical stability and microtubule organization in mitotic cells. J. Cell Biol. *180,* 739-746.

Cavazza T., and Vernos I. (2015). The RanGTP Pathway: From Nucleo-Cytoplasmic Transport to Spindle Assemby and Beyond. Front Cell Dev. Biol. *3*, 82.

Chang Y.C., Nalbant P., Birkenfeld J., Chang Z.F., and Bokoch G.M. (2008). GEF-H1 couples nocodazole-induced microtubule disassembly to cell contractility via RhoA. Mol. Biol. Cell. *19*, 2147-2153.

Cheffings T.H., Burroughs N.J., and Balasubramanian M.K. (2016). Actomyosin ring formation and tension generation in eukaryotic cytokinesis. Curr. Biol. *26,* R719-R737.

Chen A., Akhshi T.K., Lavoie B.D., and Wilde A. (2015). Importin β2 mediates the spatio-temporal regulation of anillin through a noncanonical nuclear localization signal. J. Biol. Chem. *290,* 13500-13509.

Clarke P.R., and Zhang C. (2008). Spatial and temporal coordination of mitosis by Ran GTPase. Nat. Rev. Mol. Cell Biol. *9,* 464-477.

Cowan C.R., and Hyman A.A. (2007). Acto-myosin reorganization and PAR polarity in *C. elegans*. Development *134*, 1035-1043.

D'Avino P.P., Giansanti M., and Petronczki M. (2015). Cytokinesis in animal cells. Cold Spring Harb. Perspect. Biol. *7,* a015834.

Dechant R., and Glotzer M. (2003). Centrosome separation and central spindle assembly act in redundant pathways that regulate microtubule density and trigger cleavage furrow formation. Dev. Cell *4,* 333-344.

Dehapiot B., and Halet G. (2013). Ran GTPase promotes oocyte polarization by regulating ERM (Ezrin/Radixin/Moesin) inactivation. Cell Cycle *12,* 1672-1678.

Dehapiot B., Carrière V., Carroll J., and Halet G. (2013). Polarized Cdc42 activation promotes polar body protrusion and asymmetric division in mouse oocytes. Dev. Biol. *377,* 202-12.

Deng M., Suraneni P., Schultz R.M., and Li R. (2007). The Ran GTPase mediates chromatin signalling to control cortical polarity during polar body extrusion in mouse oocytes. Dev. Cell *12*, 301-308.

Douglas M.E., Davies T., Joseph N., and Mishima M. (2010). Aurora B and 14-3-3 coordinately regulate clustering of centralspindlin during cytokinesis. Curr. Biol. *20*, 927-933.

Echard A., Hickson G.R., Foley E., and O'Farrell P.H. (2004). Terminal cytokinesis events uncovered after an RNAi screen. Curr. Biol. *14*, 1685-1693.

Eggert U.S., Mitchison T.J., and Field C.M. (2006). Animal cytokinesis: from parts list to mechanisms. Annu. Rev. Biochem. *75*, 543-566.

El-Amine N., Kechad A., Jananji S., and Hickson G.R. (2013). Opposing actions of septins and Sticky on Anillin promote the transition from contractile to midbody ring. J. Cell Biol. *203*, 487-504.

El-Amine N., Carim S.C., Wernike D., and Hickson G.R.X. (2019). Rho-dependent control of the Citron kinase, Sticky, drives midbody ring maturation. Mol. Biol. Cell. mbcE19040194.

Field C.M., and Alberts B.M. (1995). Anillin, a contractile ring protein that cycles from the nucleus to the cell cortex. J. Cell Biol. *131*, 165-178.

Finger F.P., and White J.G. (2002). Fusion and fission: membrane trafficking in animal cytokinesis. Cell *108*, 727-730.

Foe V.E., and von Dassow G. (2008). Stable and dynamic microtubules coordinately shape the myosin activation zone during cytokinetic furrow formation. J. Cell Biol. *183*, 457-470.

Fox D.T., and Duronio R.J. (2013). Endoreplication and polyploidy: Insights into development and disease. Development *140*, 3-12.

Frenette P., Haines E., Loloyan M., Kinal M., Pakarian P., and Piekny A. (2012). An anillin-Ect2 complex stabilizes central spindle microtubules at the cortex during cytokinesis. PLoS One *7,* e34888.

Gai M., Camera P., Dema A., Bianchi F., Berto G., Scarpa E., Germena G., and Di Cunto F. (2011). Citron kinase controls abscission through RhoA and anillin. Mol. Biol. Cell *22*, 3768-3778.

Geddis A.E., and Kaushansky K. (2006). Endomitotic Megakaryocytes Form a Midzone in Anaphase but have a Deficiency in Cleavage Furrow Formation. Cell Cycle *5*, 538-545.

Gentric G., and Desdouets C. (2014). Polyploidization in Liver Tissue. Am. J. Pathol. *184*, 322-331.

Glotzer M. (2009). The 3Ms of central spindle assembly: microtubules, motors and MAPs. Nat. Rev. Mol. Cell Biol. *10*, 9-20.

Green R.A., Paluch E., and Oegema K. (2012). Cytokinesis in animal cells. Annu. Rev. Cell Dev. Biol. *28,* 29-58.

Guillot C., and Lecuit T. (2013). Adhesion disengagement uncouples intrinsic and extrinsic forces to drive cytokinesis in epithelial tissues. Dev. Cell *11*, 227-241.

Guse A., Mishima M., and Glotzer M. (2005). Phosphorylation of ZEN-4/MKLP1 by aurora B regulates completion of cytokinesis. Curr. Biol. *15*, 778-786.

Hall P.A., Todd C.B., Hyland P.L., McDade S.S., Grabsch H., Dattani M., Hillan K.J., and Russell S.E. (2005). The septin-binding protein anillin is overexpressed in diverse human tumors. Clin. Cancer res. *11*, 6780-6786.

Hanahan D., and Weinberg R.A. (2011). Hallmarks of cancer: the next generation. Cell *144*, 646-674.

Hasegawa K., Ryu S.J., and Kaláb P. (2013). Chromosomal gain promotes formation of a steep RanGTP gradient that drives mitosis in aneuploid cells. J. Cell Biol. *200,* 151-161.

Hickson G.R., and O'Farrell P.H. (2008). Rho-dependent control of anillin behavior during cytokinesis. J. Cell Biol. *180*, 285-294.

Hu C., Coughlin M., Field C.M., and Mitchison T.J. (2008). Cell polarization during monopolar cytokinesis. J. Cell Biol. *181,* 195–202.

Inoue Y.H., Savoian M.S., Suzuki T., Máthé E., Yamamoto M.T., and Glover D.M. (2004). Mutations in orbit/mast reveal that the central spindle is comprised of two microtubule populations, those that initiate cleavage and those that propagate furrow ingression. J. Cell Biol. *166*, 49-60.

Jananji S., Risi C., Lindamulage I.K.S., Picard L.P., Van Sciver R., Laflamme G., Albaghjati A., Hickson G.R.X., Kwok B.H., and Galkin V.E. (2017). Multimodal and Polymorphic Interactions between Anillin and Actin: Their Implications for Cytokinesis. J. Mol. Biol. *429*, 715-731.

Kaláb P., and Heald R. (2008). The RanGTP gradient- a GPS for the mitotic spindle. J. Cell Sci. *121*, 1577-1586.

Kaláb P., Pralle A., Isacoff E.Y., Heald R., and Weis K. (2006). Analysis of a RanGTP-regulated gradient in mitotic somatic cells. Nature *440,* 697-701.

Kaláb P., Weis K., and Heald R. (2002). Visualization of a Ran-GTP gradient in interphase and mitotic Xenopus egg extracts. Science *295,* 2452-2456.

Kechad A., Jananji S., Ruella Y., and Hickson G.R. (2012). Anillin acts as a bifunctional linker coordinating midbody ring biogenesis during cytokinesis. Curr. Biol. *22*, 197-203.

Kim J.E., Billadeau D.D., and Chen J. (2005). The tandem BRCT domains of Ect2 are required for both negative and positive regulation of Ect2 in cytokinesis. J. Biol. Chem. *280*, 5733-5739.

Kim H., Johnson J.M., Lera R.F., Brahma S., and Burkard M.E. (2017). Anillin phosphorylation controls timely membrane association and successful cytokinesis. PLoS Genetics *13,* e1006511.

Kimura K., Tsuji T., Takada Y., Miki T., and Narumiya S. (2000). Accumulation of GTP-bound RhoA during cytokinesis and critical role of ECT2 in this accumulation. J. Biol. Chem. *275*, 17233-17236.

Kiyomitsu T., and Cheeseman I.M. (2013). Cortical dynein and asymmetric membrane elongation coordinately position the spindle in anaphase. Cell *154,* 391-402.

Kotadia S., Montembault E., Sullivan W., and Royou A. (2012). Cell elongation is an adaptive response for clearing long chromatid arms from the cleavage plane. J. Cell Biol. *199,* 745-753.

Kotýnková K., Su K.C., West S.C., and Petronczki M. (2016). Plasma Membrane Association but Not Midzone Recruitment of RhoGEF ECT2 Is Essential for Cytokinesis. Cell Rep. *17*, 2672-2686.

Lacroix B., and Maddox A.S. (2012). Cytokinesis, ploidy and aneuploidy. J. Pathol. *226,* 338-351.

Lakomtsev S., Su K.C., Pye V.E., Blight K., Sundaramoorthy S., Takaki T., Collinson L.M., Cherepanov P., Divecha N., and Petronczki M. (2012). Centralspindlin links the mitotic spindle to the plasma membrane during cytokinesis. Nature *492*, 276-279.

Lammers M., Rose R., Scrima A., and Wittinghofer A. (2005). The regulation of mDia by autoinhibition and its release by Rho*GTP. EMBO J. *23*, 4176-4187.

Lee Y.P., Wong C.H., Chan K.S., Lai S.K., Koh C.G., and Li H.Y. (2012). In vivo FRET imaging revealed a regulatory role of RanGTP in kinetochore-microtubule attachments via Aurora B kinase. PLoS One *7*, e45836.

Lewellyn L., Dumont J., Desai A., and Oegema K. (2010). Analyzing the effects of delaying aster separation on furrow formation during cytokinesis in the *Caenorhabditis elegans* embryo. Mol. Biol. Cell *21,* 50-62.

Li F., and Higgs H.N. (2003). The mouse Formin mDia1 is a potent actin nucleation factor regulated by autoinhibition. Curr. Biol. *15*, 1335-1340.

Li H.Y., and Zheng Y. (2004). Phosphorylation of RCC1 in mitosis is essential for producing high RanGTP concentration on chromosomes and for spindle assembly in mammalian cells. Genes Dev. *18*, 512-527.

Liang P.I., Chen W.T., Li C.F., Li C.C., Li W.M., Huang C.N., Yeh H.C., Ke H.L., Wu W.J., and Chai C.Y. (2015). Subcellular localisation of anillin is associated with different survival outcomes in upper urinary tract urothelial carcinoma. J. Clin. Pathol. *68*, 1026-1032.

Liu J., Fairn G.D., Ceccarelli D.F., Sicheri F., and Wilde A. (2012). Cleavage furrow organization requires PIP(2)-mediated recruitment of anillin. Curr. Biol. *22,* 64-9.

Maddox A.S., Habermann B., Desai A., and Oegema K. (2005). Distinct roles for two *C. elegans* anillins in the gonad and early embryo. Development *132*, 2837-2848.

Maddox A.S. Lewellyn L., Desai A., and Oegema K. (2007). Anillin and the septins promote asymmetric ingression of the cytokinetic furrow. Dev. Cell *12*, 827-835.

Magnusson K., Gremel G., Rydén L., Pontén V., Uhlén M., Dimberg A., Jirström K., and Pontén F. (2016). ANLN is a prognostic biomarker independent of Ki-67 and essential for cell cycle progression in primary breast cancer. BMC Cancer *16*, 904.

Mangal S., Sacher J., Kim T., Osório D.S., Motegi F., Carvalho A.X., Oegema K., and Zanin E. (2018). TPXL-1 activates Aurora A to clear contractile ring components from the polar cortex during cytokinesis. J. Cell Biol. *217*, 837-848.

McKenzie C., Bassi Z.I., Debski J., Gottardo M., Callaini G., Dadlez M., and D'Avino P.P. (2016). Cross-regulation between Aurora B and Citron Kinase controls midbody architecture in cytokinesis. Open Biol. *6*, 160019.

Mendoza M., Norden C., Durrer K., Rauter H., Uhlmann F., and Barral Y. (2009). A mechanism for chromosome segregation sensing by the NoCut checkpoint. Nat. Cell Biol. *11,* 477-483.

Meyer E.J., Ikmi A., and Gibson M.C. (2011). Interkinetic nuclear migration is a broadly conserved feature of cell division in pseudostratified epithelia. Curr. Biol. *21*, 485-491.

Miller K.G., and Kiehart D.P. (1995). Fly division. J. Cell Biol. *131*, 1-5.

Mishima M., Pavicic V., Grüneberg U., Nigg E.A., and Glotzer M. (2004). Cell cycle regulation of central spindle assembly. Nature *430*, 908-913.

Mishima M., Kaitna S., and Glotzer M. (2002). Central spindle assembly and cytokinesis require a kinesin-like protein/RhoGAP complex with microtubule bundling activity. Dev. Cell *2*, 41-54.

Montembault E., Claverie M.C., Bouit L., Landmann C., Jenkins J., Tsankova A., Cabernard C., and Royou A. (2017). Myosin efflux promotes cell elongation to coordinate chromosome segregation with cell cleavage. Nat. Commun. *8*, 326.

Morais-de-Sá E., and Sunkel C. (2013). Adherens junctions determine the apical position of the midbody during follicular epithelial cell division. EMBO Rep. *14*, 696-703.

Murthy K., and Wadsworth P. (2008). Dual role for microtubules in regulating cortical contractility during cytokinesis. J. Cell Sci. *121*, 2350-2359.

Neef R., Klein U.R., Kopajtich R., and Barr F.A. (2006). Cooperation between mitotic kinesins control the late stages of cytokinesis. Curr. Biol. *16*, 301-307.

Niiya F., Tatsumoto T., Lee K.S., and Miki T. (2006). Phosphorylation of the cytokinesis regulator ECT2 at G2/M phase stimulates association of the mitotic kinase Plk1 and accumulation of GTP-bound RhoA. Oncogene *25*, 827-837.

Nishimoto T., Eilen E., and Basilico C. (1978). Premature of chromosome condensation in a ts chromatin-mutant of BHK cells. Cell *15*, 475-483.

Nishimura Y., and Yonemura S. (2006). Centralspindlin regulates ECT2 and RhoA accumulation at the equatorial cortex during cytokinesis. J. Cell Sci. *119*, 104-114.

Norden C., Mendoza M., Dobbelaere J., Kotwaliwale C.V., Biggins S., and Barral Y. (2006). The NoCut pathway links completion of cytokinesis to spindle midzone function to prevent chromosome breakage. Cell *125*, 85-98.

Oegema K., Savoian M.S., Mitchison T.J., and Field C.M. (2000). Functional analysis of a human homologue of the Drosophila actin binding protein anillin suggests a role in cytokinesis. J. Cell Biol. *150*, 539-552.

Olakowski M., Tyszkiewicz T., Jarzab M., Król R., Oczko-Wojciechowska M., Kowalska M., Kowal M., Gala G.M., Kajor M., Lange D., Chmielik E., Gubala E., Lampe P., and Jarzab B. (2009). NBL1 and anillin (ANLN) genes over-expression in pancreatic carcinoma. Folia Histochem. Cytobiol. *47*, 249-255.

Pandit S.K., Westendorp B., and de Bruin A. (2013). Physiological significance of polyploidization in mammalian cells. Trends Cell Biol. *23*, 556-566.

Petronczki M., Glotzer M., Kraut N., and Peters J.M. (2007). Polo-like kinase 1 triggers the initiation of cytokinesis in human cells by promoting recruitment of the RhoGEF Ect2 to the central spindle. Dev. Cell *12*, 713-725.

Piekny A.J., and Glotzer M. (2008). Anillin is a scaffold protein that links RhoA, actin, and myosin during cytokinesis. Curr. Biol. *18,* 30-36.

Piekny A.J., and Maddox A.S. (2010). The myriad roles of Anillin during cytokinesis. Sem. Cell Dev. Biol. *21,* 881-891.

Piekny A., Werner M., and Glotzer M. (2005). Cytokinesis: welcome to the Rho zone. TRENDs in Cell Biology *15*, 651-658.

Pollard T.D., and O'Shaughnessy B. (2019). Molecular Mechanism of Cytokinesis. Annu. Rev. Biochem. *88*, 661-689.

Potapova T.A., Daum J.R., Pittman B.D., Hudson J.R., Jones T.N., Satinover D.L., Stukenberg P.T., and Gorbsky G.J. (2006). The reversibility of mitotic exit in vertebrate cells. Nature *440,* 954-958.

Rankin K.E., and Wordeman L. (2010). Long astral microtubules uncouple mitotic spindles from the cytokinetic furrow. J. Cell Biol. *190*, 35-43.

Rappaport R. (1996). Cytokinesis in animal cells. Cambridge University Press, Cambridge.

Reyes C.C., Jin M., Breznau E.B., Espino R., Delgado-Gonzalo R., Goryachev A.B., and Miller A.L. (2014). Anillin Regulates Cell-Cell Junction Integrity by Organizing Junctional Accumulation of Rho-GTP and Actomyosin. Curr. Biol. *24*, 1263-70.

Rodrigues N.T., Lekomtsev S., Jananji S., Kriston-Vizi J., Hickson G.R., and Baum B. (2015). Kinetochore-localized PP1-Sds22 couples chromosome segregation to polar relaxation. Nature *524,* 489-492.

Roubinet C., Decelle B., Chicanne G., Dorn J.F., Payrastre B., Payre F., and Carreno S. (2011). Molecular networks linked by moesin drive remodeling of the cell cortex during mitosis. J. Cell Biol. *195,* 99-112.

Ruchaud S., Carmena M., and Earnshaw W.C. (2007). Chromosomal passenger: conducting cell division. Nat. Rev. Mol. Cell Biol. *8*, 798-812.

Samwer M., Dehne H.J., Spira F., Kollmar M., Gerlich D.W., Urlaub H., and Görlich D. (2013). The nuclear F-actin interactome of Xenopus oocytes reveals an actin-bundling kinesin that is essential for meiotic cytokinesis. EMBO J. *32*, 1886-1902.

Schenk C., Bringmann H., Hyman A.A., and Cowan C.R. (2010). Cortical domain correction repositions the polarity boundary to match the cytokinesis furrow in *C. elegans* embryos. Development *137*, 1743-1753.

Sedzinski J., Biro M., Oswald A., Tinevez JY., Salbreux G., and Paluch E. (2011). Polar actomyosin contractility destabilizes the position of the cytokinetic furrow. Nature *476*, 462-466.

Silverman-Gavrila R.V., Hales K.J., and Wilde A. (2008). Anillin-mediated Targeting of Peanut to Pseudocleavage Furrows Is Regulated by the GTPase Ran. Mol. Biol. Cell *19,* 3735–3744.

Soderholm J.F., Bird S.L., Kaláb P., Sampathkumar Y., Hasegawa K., Uehara-Bingen M., Weis K., and Heald R. (2011). Importazole, a small molecule inhibitor of the transport receptor importin-β. ACS Chem. Biol. *6,* 700-708.

Solski P.A., Wilder R.S., Rossman K.L., Sondek J., Cox A.D., Campbell S.L., and Der C.J. (2004). Requirement for C-terminal sequences in regulation of Ect2 guanine nucleotide exchange specificity and transformation. J. Biol. Chem. *279*, 25226-25233.

Somers W.G., and Saint R. (2003). A RhoGEF and Rho family GTPase-activating protein complex links the contractile ring to cortical microtubules at the onset of cytokinesis. Dev. Cell *4,* 29-39.

Soniat M., and Chook Y.M. (2015). Nuclear localization signals for four distinct karyopherin- β nuclear import systems. Biochem. J. *468,* 353-362.

Spear P.C., and Erickson C.A. (2012). Apical movement during interkinetic nuclear migration is a two-step process. Dev. Biol. *370*, 33-41.

Steigemann P., Wurzenberger C., Schmitz M.H., Held M., Guizetti J., Maar S., and Gerlich D.W. (2009). Aurora B-mediated abscission checkpoint protects against tetraploidization. Cell *136*, 473-484.

Straight A.F., Field C.M., and Mitchison T.J. (2005). Anillin binds nonmuscle myosin II and regulates the contractile ring. Mol. Biol. Cell *16,* 193-201.

Su K.C., Takaki T., and Petronczki M. (2011). Targeting of the RhoGEF Ect2 to the equatorial membrane controls cleavage furrow formation during cytokinesis. Dev. Cell *21*, 1104-1115.

Sun L., Guan R., Lee I.J., Liu Y., Chen M., Wang J., Wu J.Q., and Chen Z. (2015). Mechanistic insights into the anchorage of the contractile ring by anillin and Mid1. Dev. Cell *33,* 413-426.

Tatsumoto T., Xie X., Blumenthal R., Okamoto I., and Miki T. (1999). Human ECT2 is an exchange factor for Rho GTPases, phosphorylated in G2/M phases, and involved in cytokinesis. J. Cell Biol. *147*, 921-928.

Tse Y.C., Piekny A., and Glotzer M. (2011). Anillin promotes astral microtubule-directed cortical myosin polarization. Mol. Biol. Cell *22,* 3165-3175.

Vale R.D., Spudich J.A., and Griffis E.R. (2009). Dynamics of myosin, microtubules, and Kinesin-6 at the cortex during cytokinesis in Drosophila S2 cells. J. Cell Biol. *186*, 727-738.

van Oostende Triplet C., Garcia M.J., Haji Bik H., Beaudet D., and Piekny A. (2014). Anillin interacts with microtubules and is part of the astral pathway that defines cortical domains. J. Cell Sci. *127,* 3699-3710.

von Dassow G., Verbrugghe K.J.C., Miller A.L., Sider J.R., and Bement W.M. (2009). Action at a distance during cytokinesis. J. Cell Biol. *187*, 831-845.

Wagner E., and Glotzer M. (2016). Local RhoA activation induces cytokinetic furrows independent of spindle position and cell cycle stage. J. Cell Biol. *213*, 641-649.

Wang G., Shen W., Cui L., Chen W., Hu X., and Fu J. (2016). Overexpression of Anillin (ANLN) is correlated with colorectal cancer progression and poor prognosis. Cancer Biomark. *16*, 459-465.

Watanabe S., Ando Y., Yasuda S., Hosoya H., Watanabe N., Ishizaki T., and Narumiya S. (2008). mDia2 induces the actin scaffold for the contractile ring and stabilizes its position during cytokinesis in NIH 3T3 cells. Mol. Biol. Cell *19*, 2328-2338.

Watanabe S., Okawa K., Miki T., Sakamoto S., Morinaga T., Segawa K., Arakawa T., Kinoshita M., Ishizaki T., and Narumiya S. (2010). Rho and anillin-dependent control of mDia2 localization and function in cytokinesis. Mol. Biol Cell. *21*,3193-3204.

Watanabe S., De Zan T., Ishizaki T., and Narumiya S. (2013). Citron kinase mediates transition from constriction to abscission through its coiled-coil domain. J. Cell Sci. *126*, 1773-1784.

Weaver L.N., and Walczak C.E. (2015). Spatial gradients controlling spindle assembly. Biochem. Soc. Trans. *43*, 7-12.

Werner M., Munro E., and Glotzer M. (2007). Astral signals spatially bias cortical myosin recruitment to break symmetry and promote cytokinesis. Curr. Biol. *17*, 1286–1297.

Willet A.H., DeWitt A.K., Beckley J.R., Clifford D.M., and Gould K.L. (2019). NDR Kinase Sid2 Drives Anillin-like Mid1 from the Membrane to Promote Cytokinesis and Medial Division Site Placement. Curr Biol. *29*, 1055-1063.

Wolfe B.A., Takaki T., Petronczki M., and Glotzer M. (2009). Polo-like kinase 1 directs assembly of the HsCyk-4 RhoGAP/Ect2 RhoGEF complex to initiate cleavage furrow formation. PLoS Biol. *7*, e1000110.

Yüce O., Piekny A., and Glotzer M. (2005). An ECT2–centralspindlin complex regulates the localization and function of RhoA. J. Cell Biol. *170,* 571–582.

Zanin E., Desai A., Poser I., Toyoda Y., Andree C., Moebius C., Bickle M., Conradt B., Piekny A., and Oegema K. (2013). A conserved RhoGAP limits M phase contractility and coordinates with microtubule asters to confine RhoA during cytokinesis. Dev. Cell *26,* 496-510.

Zeng S., Yu X., Ma C., Song R., Zhang Z., Zi X., Chen X., Wang Y., Yu Y., Zhao J., Wei R., Sun Y., and Xu C. (2017). Transcriptome sequencing identifies ANLN as a promising prognostic biomarker in bladder urothelial carcinoma. Sci. Rep. *7*, 3151.

Zhao W.M., and Fang G. (2005). MgcRacGAP controls the assembly of the contractile ring and the initiation of cytokinesis. Proc. Natl. Acad. Sci. U.S.A. *102,* 13158–13163.

Supplemental Figures

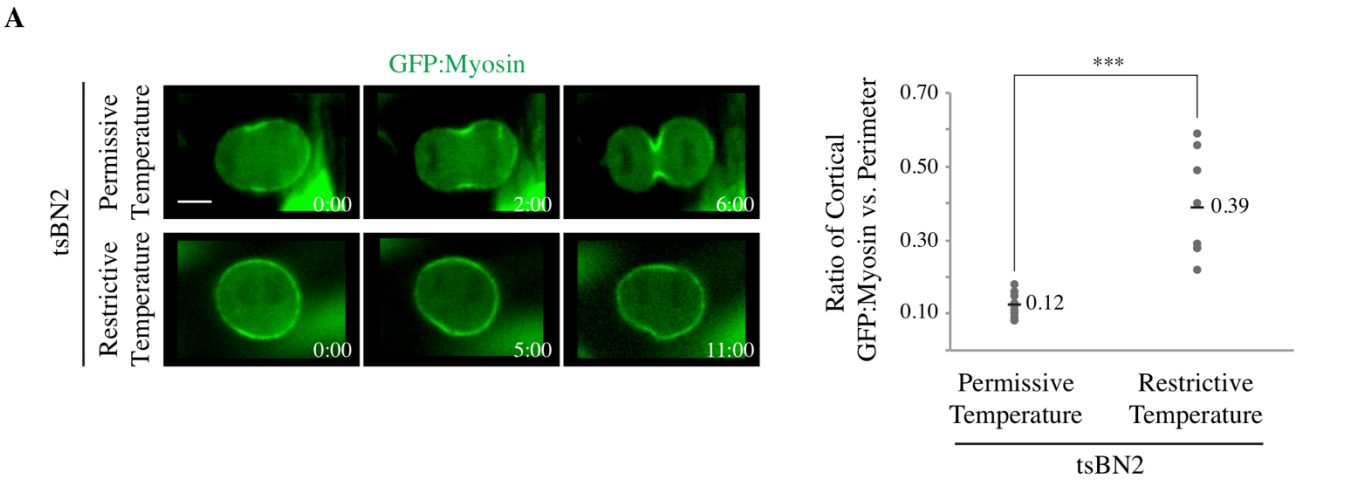

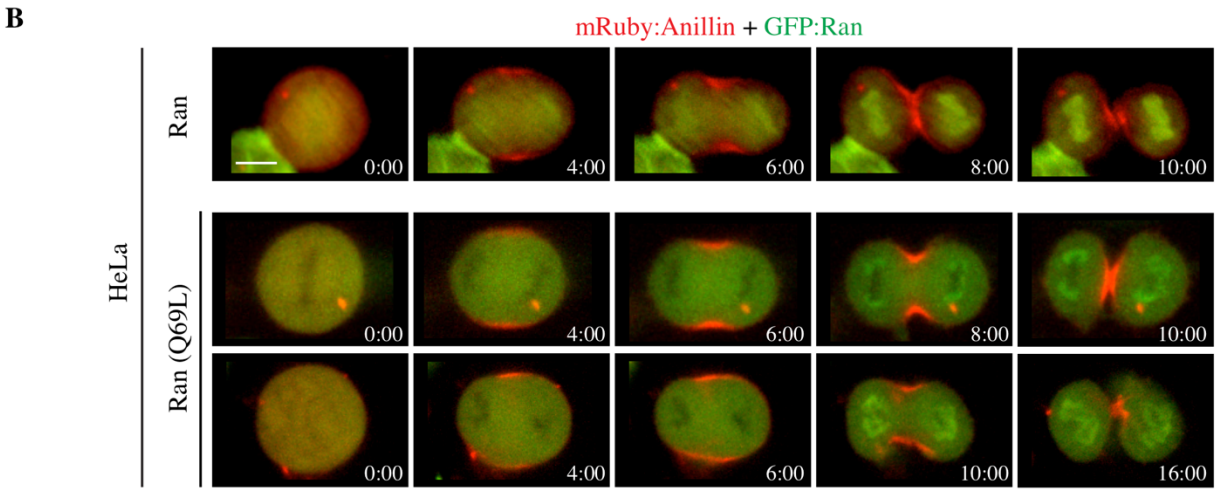

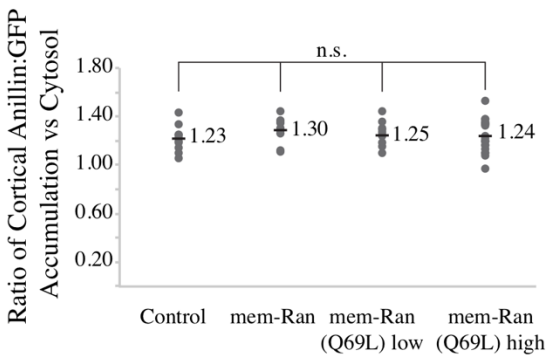

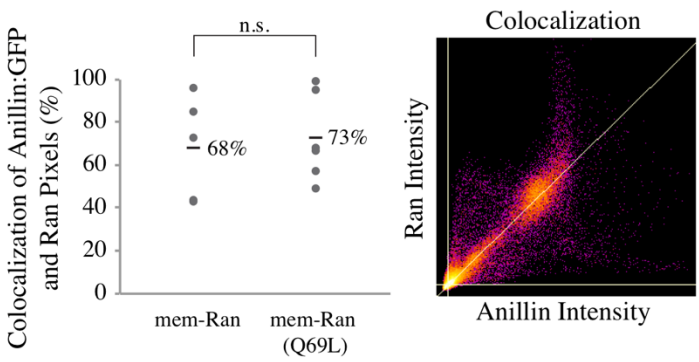

Figure S1. Related to Figures 3 and 4. Active Ran influences the localization of contractile proteins during cytokinesis

A) Timelapse images show tsBN2 cells expressing GFP:myosin (MLC; myosin light chain; active), at permissive temperature (33°C; n=29), and after upshift to restrictive temperature (39.7°C; n=23) during cytokinesis. The scale bar is 10 μm. A dot plot shows the ratio of the breadth of myosin (GFP:myosin) accumulation vs. cell perimeter in tsBN2 cells at permissive (n=9) or restrictive (n=8) temperatures. The means are indicated, and the data were analyzed using the Student's t test (*** $p < 0.001$). **B**) Timelapse images show HeLa cells co-expressing GFP:Ran (green; n=5; top panel) or GFP:Ran (Q69L; green; n=9; bottom two panels) and mRuby:anillin (red). **C**) A dot plot shows changes in the ratio of cortically accumulated anillin vs. cytosol just prior to furrow ingression in cells overexpressing membrane-targeted Ran or RanQ69L, as indicated (control, n=9, membrane-targeted Ran, n=13, low expressing membrane-targeted Ran(Q69L), n=11, and membrane-targeted Ran(Q69L), n=23). The means are shown, and the data was analyzed using the Student's t test (n.s., not significant). **D**) A dot blot shows the percentage of colocalization of anillin and Ran (n=5) or Ran (Q69L; n=6) pixels in different regions of the cortex as indicated. The means are shown and the data was analyzed using the Student's t test. The scatter plot to the right shows an example of the alignment of pixels for the cortex for one cell.

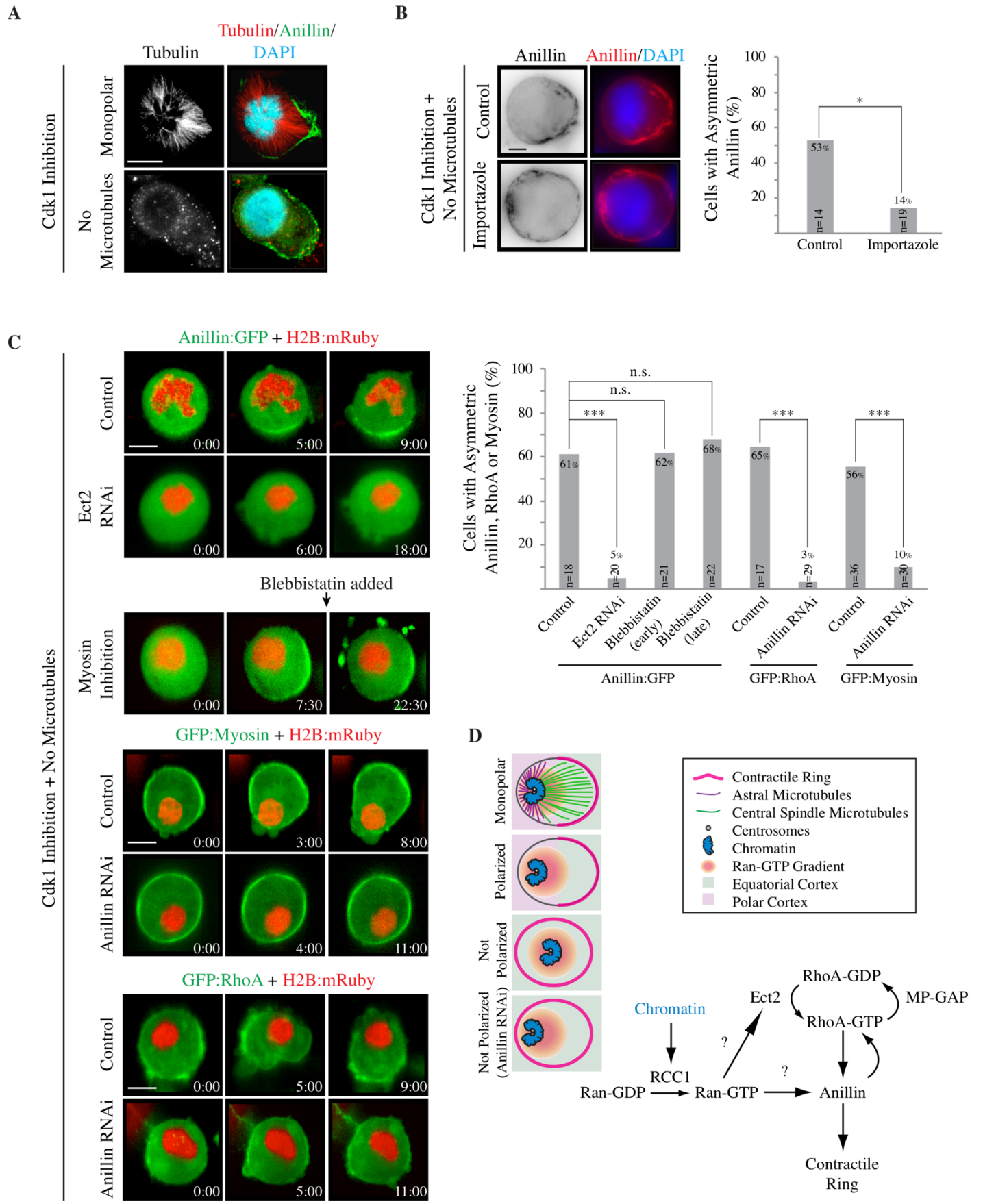
A
Tubulin
Tubulin/Anillin/
DAPI
Cdk1 Inhibition
Monopolar
No
Microtubules
B
Anillin
Anillin/DAPI
Cdk1 Inhibition +
No Microtubules
Control
Importazole
Cells with Asymmetric
Anillin (%)
100
80
60
40
20
*
53%
14%
n=14
n=19
Control
Importazole
C
Anillin:GFP + H2B:mRuby
Control
Ect2
RNAi
0:00
5:00
9:00
0:00
6:00
18:00
Blebbistatin added
Myosin
Inhibition
0:00
7:30
22:30
GFP:Myosin + H2B:mRuby
Control
Anillin RNAi
0:00
3:00
8:00
0:00
4:00
11:00
GFP:RhoA + H2B:mRuby
Control
Anillin RNAi
0:00
5:00
9:00
0:00
5:00
11:00
Cdk1 Inhibition + No Microtubules
Cells with Asymmetric
Anillin, RhoA or Myosin (%)
100
80
60
40
20
n.s.
n.s.
***
***
***
61%
5%
62%
68%
65%
3%
56%
10%
n=18
n=20
n=21
n=22
n=17
n=29
n=36
n=30
Control
Ect2 RNAi
Blebbistatin
(early)
Blebbistatin
(late)
Control
Anillin RNAi
Control
Anillin RNAi
Anillin:GFP
GFP:RhoA
GFP:Myosin
D
Monopolar
Polarized
Not
Polarized
Not Polarized
(Anillin RNAi)
Contractile Ring
Astral Microtubules
Central Spindle Microtubules
Centrosomes
Chromatin
Ran-GTP Gradient
Equatorial Cortex
Polar Cortex
Chromatin
RCC1
Ran-GDP
Ran-GTP
?
Ect2
?
RhoA-GDP
RhoA-GTP
MP-GAP
Anillin
Contractile
Ring

Figure S2. Related to Figure 5. Anillin may be a target of the Ran pathway

A) Images show fixed HeLa cells treated with 2 μM S-trityl cysteine (top cell; Hu et al., 2008) or 100 nM nocodazole to depolymerize microtubules (bottom cell) and 22.5 μM Purvalanol A to force mitotic exit, co-stained for tubulin (red), anillin (green) and DAPI (chromatin; cyan). The scale bar is 10 μm. **B**) Images show fixed HeLa cells treated with nocodazole and Purvalanol A as in (A), after treatment with DMSO (control) or 100 nM Importazole to block the Ran-GTP-importin interaction, co-stained for anillin (red) and DAPI (chromatin, blue). The scale bar is 10 μm. To the right, a bar graph shows the percentage of cells with asymmetric anillin localization for control or Importazole-treated cells. The data was analyzed using Fisher's exact test (* $p < 0.05$) and the n's are indicated on the graph. **C**) Timelapse images show HeLa cells stably expressing anillin:GFP and H2B:mRuby treated as in (A) with Ect2 RNAi or 100 μM Blebbistatin to inhibit non-muscle myosin II (late, time of addition shown by the arrow). Underneath are shown HeLa cells stably expressing GFP:myosin or GFP:RhoA and H2B:mRuby treated with Nocodazole and Purvalanol A as in (A) with anillin RNAi. The scale bar is 10 μm. To the right is a bar graph showing the percentage of cells with asymmetric anillin, RhoA or myosin. Blebbistatin (early) refers to cells where it was added at the same time as Purvalanol A, while Blebbistatin (late) refers to cells where it was added ~7 minutes after Purvalanol A. The data was analyzed using Fisher's exact test (*** $p < 0.001$) and the n's are indicated on the graph. **D**) Cartoon models show the localization of contractile proteins in polarized cells with or without microtubules, altered chromatin position and after anillin RNAi as indicated. A pathway shows some of the key regulators of cytokinesis, with the proposed placement of Ran-GTP upstream of the contractile ring, regulating anillin or an upstream component.

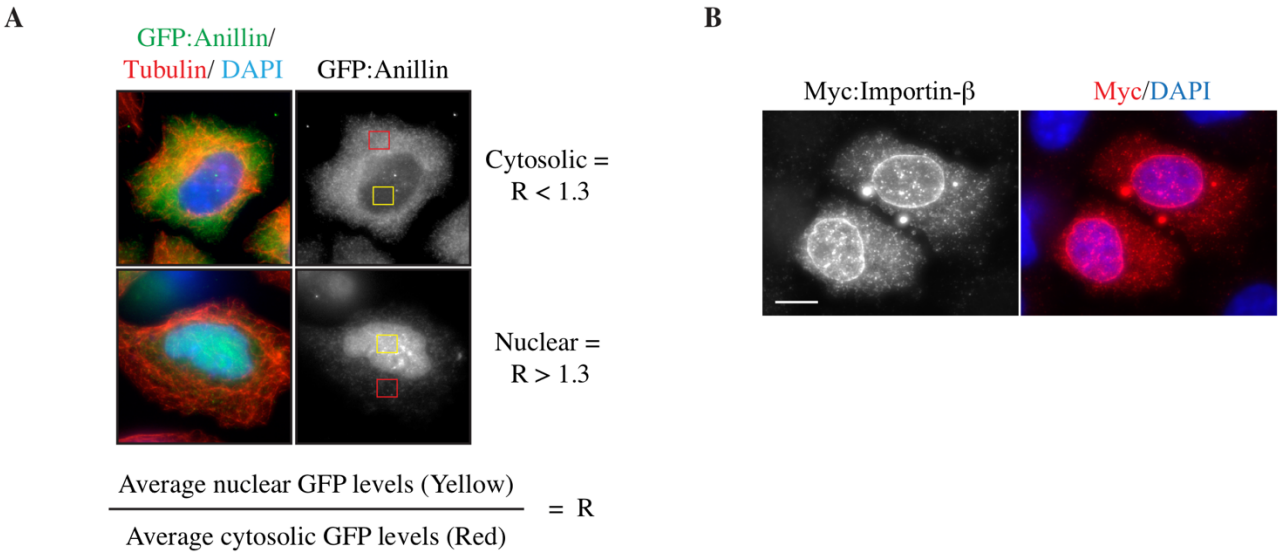
A
GFP:Anillin/
Tubulin/ DAPI
GFP:Anillin
Cytosolic =
R < 1.3
Nuclear =
R > 1.3
Average nuclear GFP levels (Yellow)
Average cytosolic GFP levels (Red)
= R
B
Myc:Importin-β
Myc/DAPI

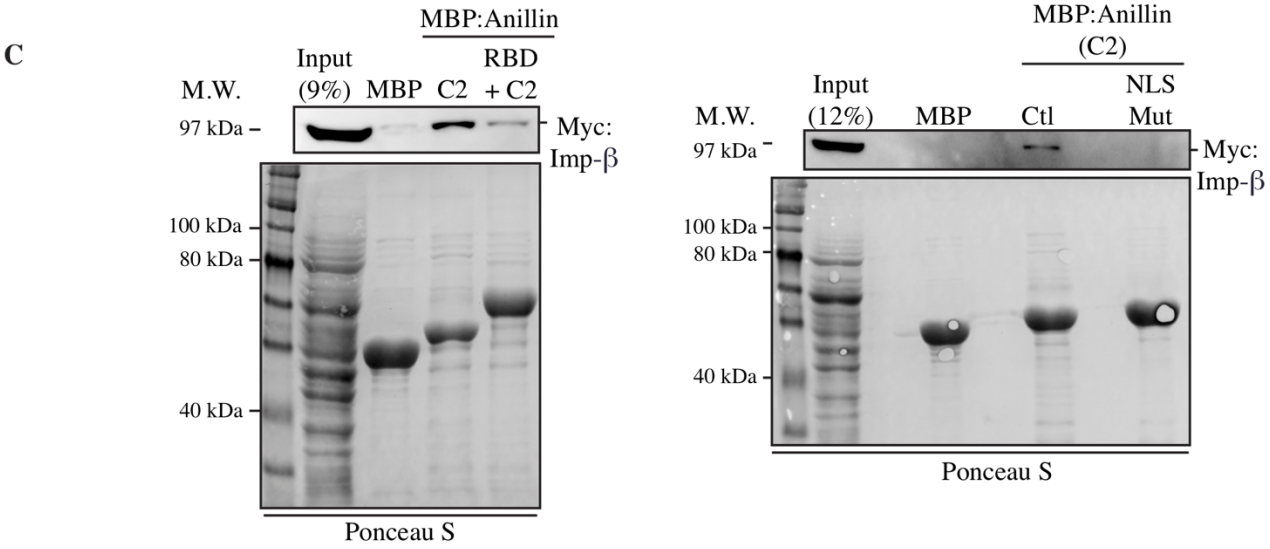
C
MBP:Anillin
Input
(9%)
MBP
C2
RBD
+ C2
M.W.
97 kDa
Myc:
Imp-β
100 kDa
80 kDa
40 kDa
Ponceau S
MBP:Anillin
(C2)
Input
(12%)
MBP
Ctl
NLS
Mut
M.W.
97 kDa
Myc:
Imp-β
100 kDa
80 kDa
40 kDa
Ponceau S

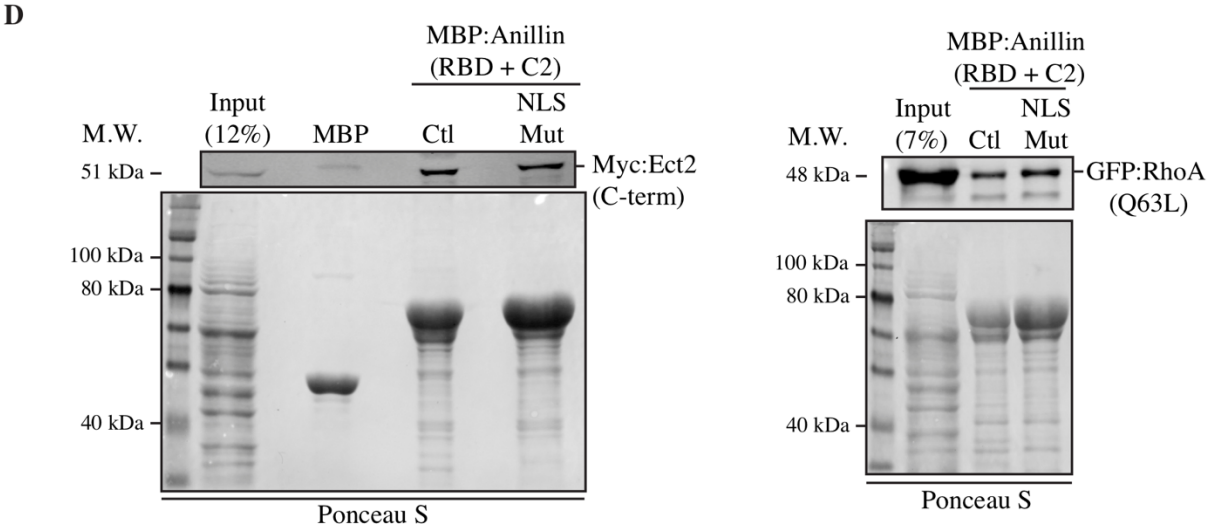
D
MBP:Anillin
(RBD + C2)
Input
(12%)
MBP
Ctl
NLS
Mut
M.W.
51 kDa
Myc:Ect2
(C-term)
100 kDa
80 kDa
40 kDa
Ponceau S
MBP:Anillin
(RBD + C2)
Input
(7%)
Ctl
NLS
Mut
M.W.
48 kDa
GFP:RhoA
(Q63L)
100 kDa
80 kDa
40 kDa
Ponceau S

Figure S3. Related to Figure 6. The C-terminal NLS of anillin binds to importin

A) Images of fixed interphase HeLa cells co-stained for GFP:anillin (green), tubulin (red) or DAPI (chromatin; blue) show how anillin was determined to be nuclear vs. cytosolic. The average levels in the yellow square (nucleus) were calculated as a ratio (*R*) vs. the average levels in the red square (cytosol). If $R > 1.3$, anillin was determined to be nuclear, while $R < 1.3$ was cytosolic. **B**) Images show fixed interphase HeLa cells expressing Myc:importin-β, co-stained for Myc (red) and DAPI (chromatin; blue). The scale bar is 10 μm. **C**) Immunoblots of the pull-down assays from **Figure 4B** showing importin-β binding to MBP-tagged anillin fragments are shown with corresponding ponceau S-stained blots for total protein levels. **D**) Immunoblots of pull-down assays show Ect2 (left) or RhoA (Q63L; right) binding to MBP-tagged nonmutant or NLS mutant anillin (RBD + C2). Underneath, the corresponding ponceau S-stained blots show total protein levels.

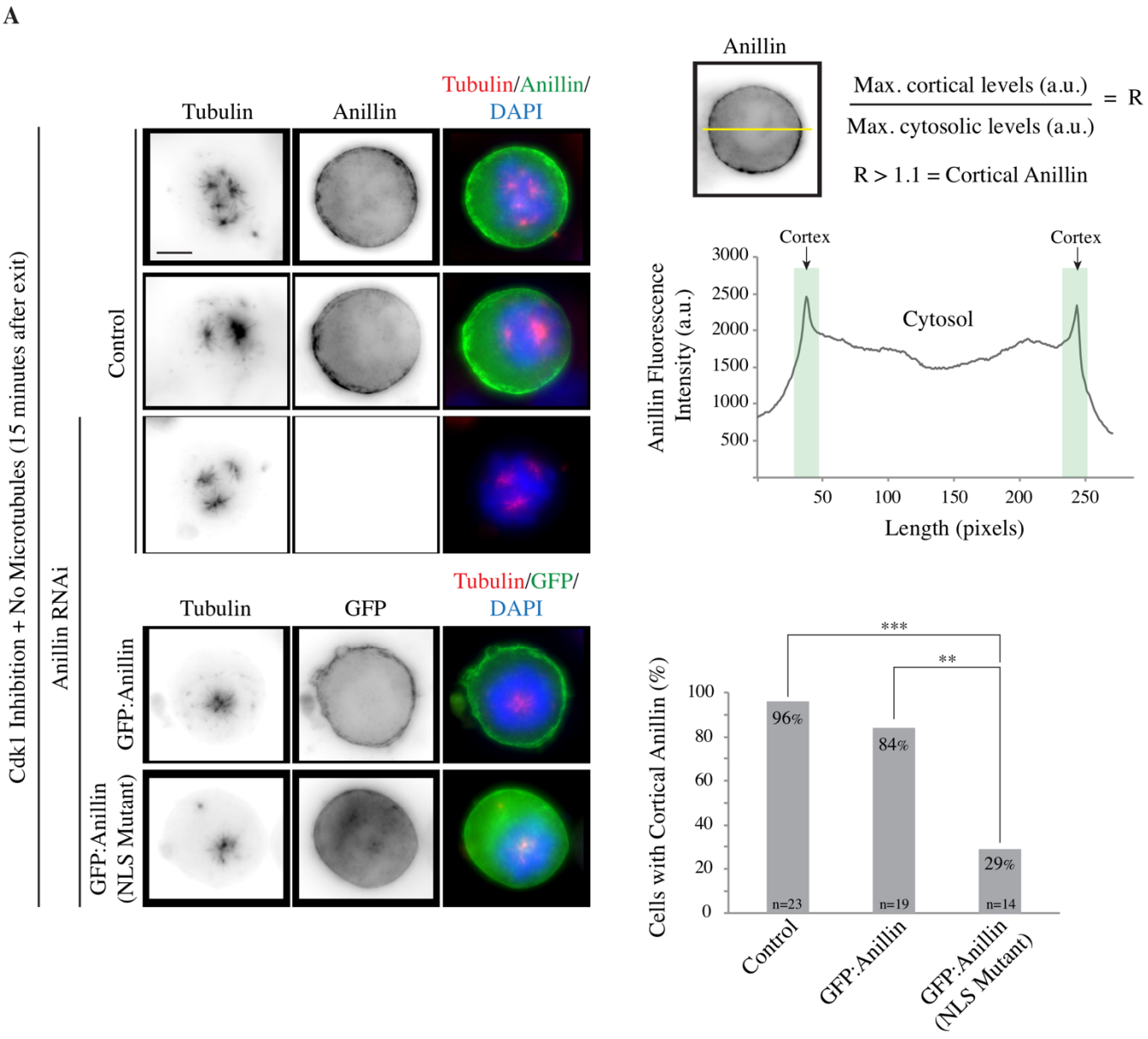
A
Anillin
Max. cortical levels (a.u.) / Max. cytosolic levels (a.u.) = R
R > 1.1 = Cortical Anillin
Tubulin/Anillin/DAPI
Tubulin
Anillin
Control
Cdk1 Inhibition + No Microtubules (15 minutes after exit)
Anillin RNAi
Tubulin/GFP/DAPI
Tubulin
GFP
GFP:Anillin
GFP:Anillin (NLS Mutant)
Cortex
Cortex
Cytosol
Anillin Fluorescence Intensity (a.u.)
3000
2500
2000
1500
1000
500
50
100
150
200
250
Length (pixels)
***
**
Cells with Cortical Anillin (%)
100
80
60
40
20
0
96%
84%
29%
n=23
n=19
n=14
Control
GFP:Anillin
GFP:Anillin (NLS Mutant)
B
+
-
+
-
+
Microtubules (MTs)
S P S P S P S P S P
MBP:Anillin (C2)
MTs
MBP:Anillin (C2)
MBP:Anillin (C2; NLS Mut)

Figure S4. Related to Figures 5 and 8. Anillin's C-terminal NLS is required for cortical recruitment

A) Images show fixed HeLa cells treated with anillin RNAi and co-expressing RNAi- resistant full-length GFP:anillin, (1-1087) with or without mutations in the C-terminal NLS (850 KK 851-DE; NLS Mutant), treated with 100 nM nocodazole and 22.5 μM Purvalanol A to depolymerize microtubules and induce mitotic exit, respectively. Cells were fixed 15 minutes after exit and co-stained for endogenous anillin or GFP (green), tubulin (red) and DAPI (chromatin; blue). The scale bar is 10 μm. To the right is a schematic to show how anillin's localization was determined to be cortical. A line scan was drawn across the cell to compare the levels of anillin fluorescence at the cortex (green rectangles) vs. cytosol, with length (pixels) on the X axis and anillin fluorescence (a.u.) on the Y axis. If maximal levels at the cortex were > 1.1-fold vs. the cytosol, anillin was determined to be cortical. Underneath, a bar graph shows the % of cells with cortical anillin for control (endogenous anillin), anillin-depleted cells rescued with RNAi- resistant GFP:anillin, and anillin-depleted cells rescued with RNAi-resistant GFP:anillin (NLS mutant). The data was analyzed by the Fisher's exact test, and the n's are shown on the graph (** $p < 0.01$, *** $p < 0.001$).
B) The image shows a Coomassie-stained gel of co-sedimentation assays (S, supernatants; P, pellets) using 1.5 μM purified microtubules (MT) incubated with 1.5 μM purified MBP-tagged anillin C2 vs. C2 NLS mutant proteins.

A

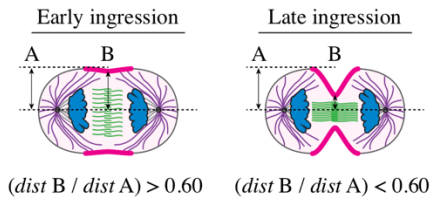

B

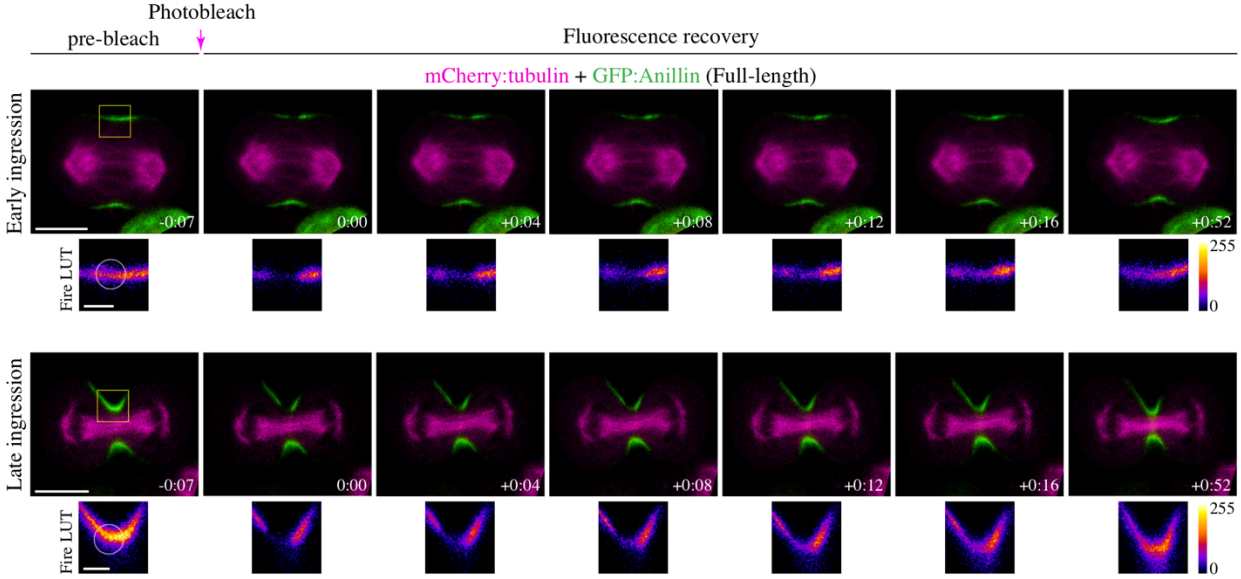

C

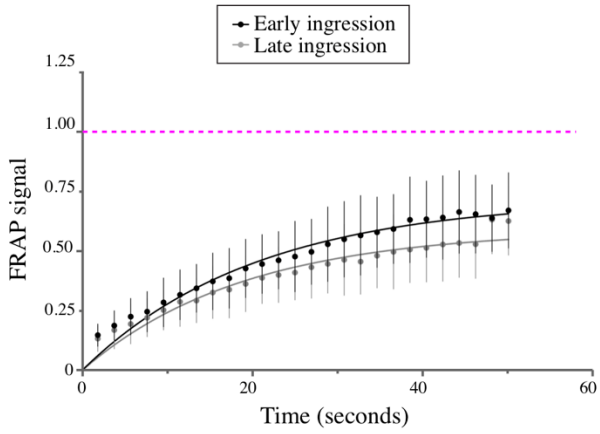

	Early ingression	Late ingression
y_{max}	0.7233 (0.02110)	0.5953 (0.02423)
k_{off} (s^{-1})	0.04717 (0.003119)	0.05094 (0.004947)
$\tau_{1/2}$ (s)	14.70	13.61

Figure S5. Related to Figure 9. Anillin has different cortical properties during early vs. late ingression

A) Cartoon cells show how the stage of ingression was determined by the ratio of the length of the ingressed cortex (B) over the width of the cell at the equator (A); where $R > 0.6$ was 'early' and $R < 0.6$ was 'late'. **B**) Timelapse images show FRAP of HeLa cells expressing mCherry:Tubulin (magenta) and GFP:Anillin (full-length; green) during early or late ingression. The boxed insets show the ROI's that were photobleached in Fire LUTs. The scale bar is 10 μm. Indicated times are before (-) or after (+) photobleaching. **C**) A graph shows the fraction of fluorescence recovery (Y-axis) over time (X-axis, seconds) for anillin during early (n=31) and late (n=15) ingression. Bars show standard deviation (SD). The table shows the maximum recovery (y_{max}), dissociation rate (k_{off}) and half-life ($\tau_{1/2}$) of anillin during early and late ingression. Standard errors are shown in parentheses (SEM).

A

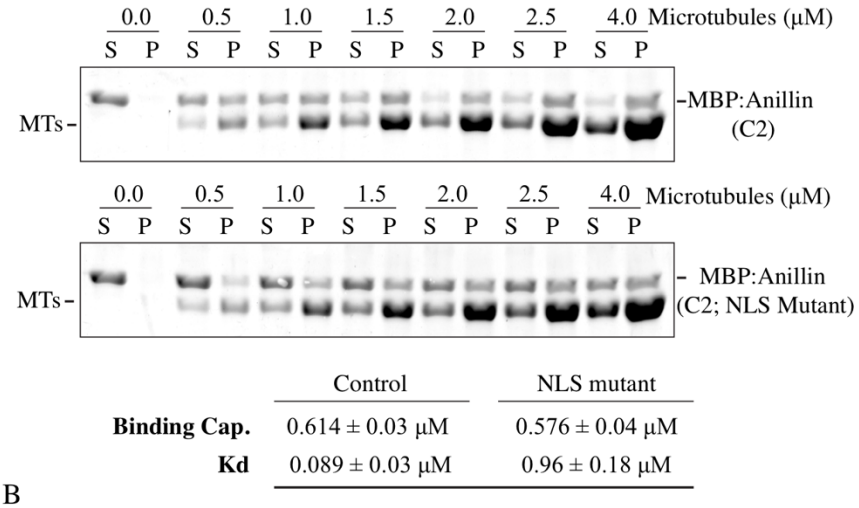

	Control	NLS mutant
Binding Cap.	0.614 ± 0.03 μM	0.576 ± 0.04 μM
Kd	0.089 ± 0.03 μM	0.96 ± 0.18 μM

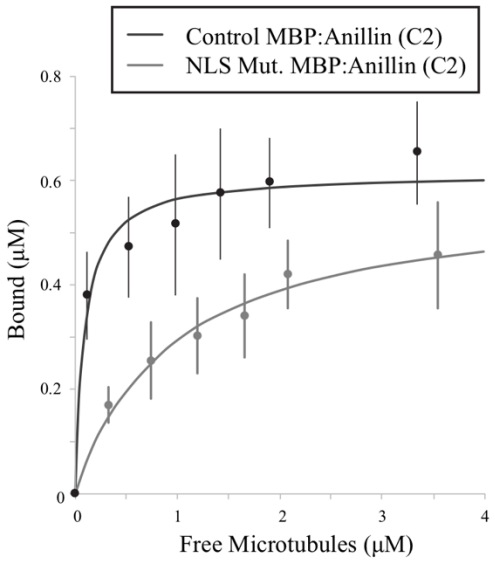

B

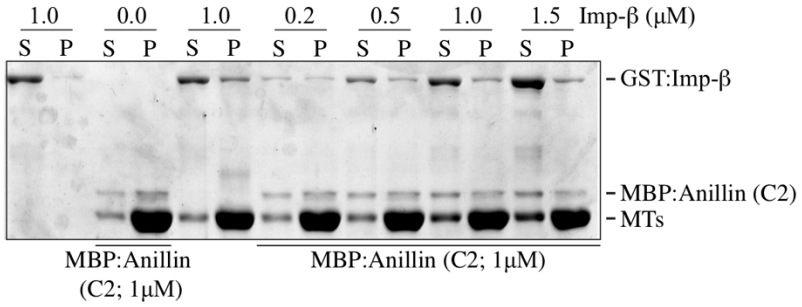

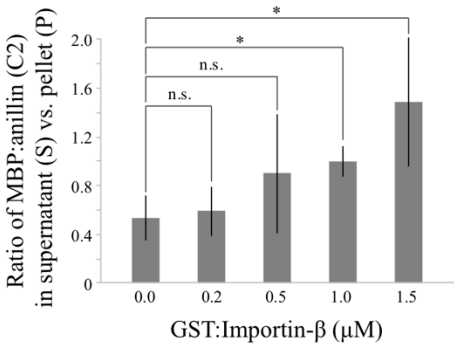

C

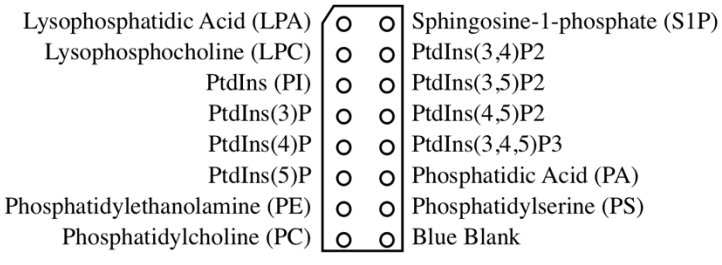

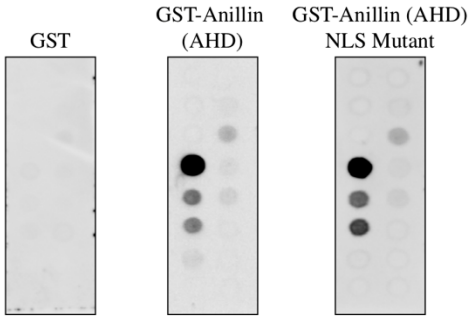

Figure S6. Related to Figure 10. The microtubule-binding region partially overlaps with the C-terminal NLS

A) Images show Coomassie-stained gels of co-sedimentation assays using 1.5 μM purified microtubules (MTs) with 1.5 μM MBP-tagged anillin C2 (top) or NLS mutant (bottom; S, supernatants; P, pellets). The table shows their mean binding capacity and dissociation coefficients, along with the SD. The graph shows bound anillin C2 (μM; Y-axis) plotted against free microtubules (μM; X-axis). Bars show SD (n=3 replicates). **B**) Images show Coomassie-stained gels of co-sedimentation assays using 1.5 μM purified MTs incubated with 1.5 μM MBP-tagged anillin C2 and 0-1.5 μM GST-tagged importin-β (S, supernatants; P, pellets). The bar graph shows the ratio of anillin (C2) in the supernatant (S) vs. bound (pellet; P) for the indicated concentrations (μM) of GST:Importin-β. Bars show SD (n=3 replicates). Data was analyzed and p values were determined by Student's t test (n.s., not significant; *$p < 0.05$). **C**) Immunoblots show PIP (phospholipids) strips incubated with purified GST, GST-tagged anillin (AHD) control or NLS mutant protein. The schematic shows the different lipids on the blots.

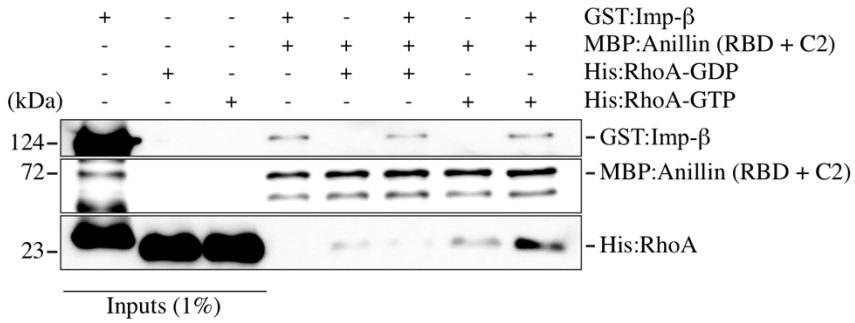

Figure S7. Related to Figure 12 and 13. Importin-binding enhances anillin's affinity for active RhoA

An immunoblot shows pull-downs of purified recombinant His-tagged RhoA pre-loaded with GDP or GTP with MBP-tagged anillin (RBD + C2) +/- purified GST-tagged importin-β as indicated. Inputs are on the left.